

PHASE-FIELD MODELING OF SOLID STATE PRECIPITATES

USING PHASE-FIELD MODELING

WITH

ADAPTIVE MESH REFINEMENT

TO STUDY

ELASTO-PLASTIC EFFECTS

IN

PHASE TRANSFORMATIONS

By

MICHAEL GREENWOOD

B.Sc Physics and Computer Science, Dalhousie University
MaSc Materials Science and Engineering, McMaster University

A Thesis

Submitted to the School of Graduate Studies
in Partial Fulfilment of the Requirements
for the Degree
Doctor of Philosophy

McMaster University

©Copyright by Michael Greenwood, November 2008

DOCTOR OF PHILOSOPHY (2008)
(Material science)

McMaster University
Hamilton, Ontario

TITLE: Using Phase-Field Modeling With Adaptive Mesh
Refinement To Study Elasto-Plastic Effects In
Phase Transformations

AUTHOR: Michael Greenwood,
B.Sc.(Dalhousie University),
MaSc (McMaster University)

SUPERVISOR: Dr. Nikolas Provatas

NUMBER OF PAGES: 122

ABSTRACT

This thesis details work done in the development of the phase field model which allows simulation of elasticity with diffuse interfaces and the extension of a thin interface analysis developed by previous authors to study *non-dilute ideal* alloys. These models are coupled with a new finite difference adaptive mesh algorithm to efficiently simulate a variety of physical systems. The finite difference adaptive mesh algorithm is shown to be at worst 4-5 times faster than an equivalent finite element method on a per node basis. In addition to this increase in speed for explicit solvers in the code, an iterative solver used to compute elastic fields is found to converge in $O(N)$ time for a dynamically growing precipitate, where N is the number of nodes on the adaptive mesh. A previous phase field formulation is extended such as to make possible the study of non-ideal binary alloys with complex phase diagrams. A phase field model is also derived for a free energy that incorporates an elastic free energy and is used to investigate the competitive development of solid state structures in which the kinetic transfer rate of atoms from the parent phase to the precipitate phase is large. This results in the growth of solid state dendrites. The morphological effects of competing surface anisotropy and anisotropy in the elastic modulus tensor is analyzed. It is shown that the transition from surface-energy driven dendrites to elastically driven dendrites depends on the magnitudes of the surface energy anisotropy coefficient (ϵ_4) and the anisotropy of the elastic tensor (β) as well as on the super saturation of the particle and therefore to a specific Mullins-Sekerka onset radius. The transition point of this competitive process is predicted from these three controlling parameters.

ACKNOWLEDGEMENTS

I would like to acknowledge my supervisor Dr. Nikolas Provatas for all the aid he has given me during the course of my PhD work and for his support over the last four years. I would like to acknowledge the help from my PhD committee as well. I would also like to thank the members of our group, the other students in our department and particularly the secretarial staff in the Materials Department at McMaster.

This thesis would never have been completed without the financial support of NSERC Canada and I would like to acknowledge the computing resources of Shar-cNet.

It has been a long journey and 25.25 years of long schooling and has finally come to yet another ending. My scattered family has been there the whole time, thanks to all of you as well. My sanity was mostly kept in tact by having an outlet for something other than thesis, and this has to go to the McMaster Fencing team. Being able to suit up, grab a weapon and stab someone really vents the frustrations.

Finally I would like to thank the Second Cup and My Dog Joe coffee shops for providing me with desk space.

Contents

Nomenclature	xi
1 Introduction	1
1.1 Solidification and Solid-State Phase Transformations	1
1.1.1 Sharp Interface Kinetics of Second Phase Formation	1
1.1.2 Experimental Studies of Widmanstätten Plates and Needles	3
1.1.3 Observations and Conditions for Solid State Dendrites	5
1.2 Basic Theory of Elasticity	7
1.3 Formation of Instabilities on Precipitate Interfaces - Linear Stability Analysis	10
1.3.1 Mullins-Sekerka Instability Theory for an Isothermal Precipitate	10
1.3.2 Linear Stability of Planar Fronts in a Temperature Gradient	12
1.4 Phenomenology of Phase Field Modeling	12
1.4.1 General Phase Field Concepts - Solidification of a Pure Material	13
1.4.2 Dilute Ideal Binary alloys: Innovations for Working with Diffuse Interfaces	17
1.5 Phase Field Modeling with Elasticity	20
2 Multi-Scale Modeling and The Adaptive Meshing Technique	25
2.1 Multi-Scale Modeling	25
2.2 Finite Difference Adaptive Grid Structure	26
2.2.1 Element Structure	28
2.2.2 Node Structure	30
2.2.3 Quad Tree Structure	31
2.3 Adaptive Mesh Refinement Algorithm	32
2.3.1 Mesh Quad Tree Adapter Algorithms	32
2.3.2 Simple Adaptive Mesh Modeling Solver Routine	34
2.4 Finite Difference Adaption Efficiency	35
2.4.1 The Reduction of the Total Node Count	36

2.4.2	The Efficiency of Finite Differencing Techniques over the Finite Element Method	38
2.4.3	Application of the Finite Difference Adaptive Mesh to Phase-field Simulations of Velocity Selection in Rapidly Solidified Binary Alloys [36]	39
2.4.4	Application of the Finite Difference Adaptive Mesh to Polycrystalline Pattern Formation Using a Coarse-grained Approximation of the Phase-Field Crystal Model[7]	40
2.4.5	Application of the Finite Difference Adaptive Mesh to the Solution of Static Elasticity by Gauss-Seidel Iteration	44
3	Thin Interface Asymptotics for Quantitative Modeling of Phase Field Models for Alloys with Non-Linear Phase Boundaries.	47
3.1	Sharp-Interface Kinetics of Binary Alloy Solidification	48
3.2	Approximating the Gibb's Free Energy Functional	49
3.3	A Phase Field Model for Solidification of Binary Alloys	51
3.4	Isothermal and Non-Isothermal Solidification of an Isomorphous Alloy	54
3.5	Diffusion limited growth in Beta-Brass	58
4	Incorporating Elasticity in the Phase Field Model	64
4.1	Sharp Interface Kinetics of Phase Transformations with Elasticity	64
4.2	Phase Field Elastic Free Energy Functional	65
4.3	A Phase Field Model For Elastically Influenced Phase Transformations	66
4.4	Growth of an Isotropic Second Phase Precipitate with Coherent Interfaces in an Isotropic Parent Phase	69
4.5	Approximation of the Strain Field Around a Precipitate with Cubic Elastic Coefficients	70
5	Morphological Transitions Due to Elastic and Surface Energy Competitions	73
5.1	Conditions Influencing the Structure of Precipitates	74
5.1.1	Elastic Anisotropy (β)	74
5.1.2	Surface Energy Anisotropy (ϵ_4)	74
5.1.3	Supersaturation(Ω)	75
5.2	Characterization of the Morphological Transition	75
5.2.1	Defining the Transition Point Between Dominant Growth Directions	76
5.2.2	Measurement of the Critical Surface Anisotropy (ϵ_4^C)	77
5.2.3	Critical Tip Radii at the Transition Point	78
5.2.4	Linear Stability Calculation of the Transition Tip Radius (R_C)	80
5.2.5	Calculation of the Critical Transition Point	82

6	Summary	85
A	Appendix - Numerical Techniques	86
A.1	Finite Differencing	86
A.1.1	Finite Difference Templates of Gradient Operators	87
A.2	Cubic Elastic Free Energy Coefficients	88
A.3	Static Elastic Solution for the Displacement Fields by Gauss-Seidel Iteration	90
A.3.1	Elastic Coefficient Pre-factors to the Discretized Displacement Templates	90
A.3.2	Discretized Terms of U_i and ϕ_i	91
A.3.3	Threshold in the Convergence of the Displacement Field	91
A.3.4	Displacement Field Dependency on the Interface Width W_o	92
B	Appendix - Phase Field Model Derivation with Elasticity	93
B.1	Phase Field Equation	95
B.2	Chemical Diffusion	96
	Terminology	98

List of Figures

1.1	CuNi Binary Phase Diagram	2
1.2	Polished meteoric iron, the Widmanstätten structure	3
1.3	Experimental solid state structures of CuZn and Ni base superalloy	6
1.4	Illustration of the Displacement field in linear elasticity theory.	8
1.5	Linear stability criteria for isothermal precipitates.	11
1.6	Amplification rate of instability modes in directional solidification	12
1.7	Schematic diagram of the phase field in 1D	14
1.8	Illustration of the temperature dependence in the free energy density in the phase field model	15
1.9	Schematic diagram of an advancing interface in the phase field model	16
1.10	Planar instability caused by applied elastic stress.	20
2.1	Adaptive mesh of a pure material dendrite and the temperature field	27
2.2	Schematic diagram of the finite difference adaptive grid data structure	28
2.3	Schematic diagram of the element data structure	29
2.4	Schematic diagram of the quad-tree data structure	31
2.5	Illustration of a node's local mini-mesh	35
2.6	Total node count on the adaptive mesh at the interface of a precipitate	36
2.7	Total node count in the bulk of both the precipitate and parent phases	37
2.8	Computational time of the finite difference adaptive mesh and a finite element adaptive mesh	38
2.9	Illustration of the phase field crystal model simulating mean positions of individual atoms	41
2.10	Phase field crystal model simulated on the adaptive mesh with the complex amplitude equations	43
2.11	Number of convergence iterations in the Gauss-Seidel formulation of the static elasticity equations on an adaptive mesh	45
3.1	Phase diagram for the NiCu binary alloy and the simulated phase diagram for an arbitrary A-B alloy	55
3.2	Predicted dimensionless steady-state tip velocities for varied values of λ for a <i>non-linear</i> phase diagram	56

3.3	Comparison of the temporal evolution of the dimensionless tip velocity for non-isothermal solidification with quenches to 1450K and then to 1400K	57
3.4	The solute concentration along the centerline of a dendrite for non-isothermal solidification	58
3.5	Temporal evolution of the dimensionless tip velocity for non-isothermal solidification with a slow cooling from 1450K to 1400K	59
3.6	Dendrite centerline solute concentration for the slow quench from 1450K to 1400K	60
3.7	CuZn Phase Diagram	61
3.8	Morphological comparison of needle growth in β brass and a phase field dendrite	62
3.9	Simulated and experimental growth rates scaled to their peak velocities.	63
3.10	Plotted scaled values of the supersaturation and the diffusion coefficients in β brass as functions of the temperature	63
4.1	A cross section of the composition field through a circular isotropic coherent precipitate and the parent phase.	70
4.2	Strain fields about circular anisotropic coherent precipitates with varied particle radius and elastic anisotropy	71
4.3	The measured values of the anisotropic strain amplitude and the fitted prediction vs β	72
5.1	Morphologies of growth precipitates in the presence of elastic and surface anisotropy	76
5.4	Illustration of the "envelope" field about 4 different precipitates in $R - \theta$ space	77
5.5	Interpolation of ϵ_4^C by examination of the envelope amplitude.	78
5.6	Fitted relationship between ϵ_4^C and β for 4 supersaturations	79
5.7	Linear relationship between the fitted critical tip radius and the Mullins-Sekerka wavelength instability	81
5.8	Critical transition lines for four different supersaturations	83
5.9	The critical transition line for an alloy composition of $C_o = 0.4$ with a morphological overlay of the precipitate structure.	84
A.1	Finite difference global and local coordinate schemes	86
A.2	Radial displacement field about an isotropic coherent precipitate for varied interface widths in the phase field model	92

List of Tables

3.1	Equilibrium parameters extracted from phase diagram tables.	59
3.2	Effective diffusion coefficients calculated from equation 3.25	60

List of Algorithms

- 1 Basic Flow of Control for the Adaptive Algorithm 32
- 2 Mesh Quad Tree Adapter Algorithm 33
- 3 Algorithm for splitting Elements 33
- 4 Algorithm for unsplitting Elements 34
- 5 Basic Algorithm for the Linear Array Finite Difference Solver . . . 35

Nomenclature

A	Number of nodes on the surface area(3-D) or arc length(2-D) of the precipitates	44
$A(\vec{n})$	Function for surface energy anisotropy	14
A_a	A constant representing the number of nodes across the normal of the interface	36
A_b	A constant related to the geometry of the precipitate (ie. circle or needle)	36
A_j	Complex amplitude of the dimensionless density field	41
B	Elastic modification to the phase field equation	67
$B(\vec{n})$	Function for kinetic anisotropy	16
C	Local concentration	2
CX_{ijkl}	Elastic Modulus Tensor for phase X	22
C^{eq}	Local equilibrium concentration	3
C_L	Equilibrium concentration on the liquid side interface.	1
C_S	Equilibrium concentration on the solid side interface.	1
C_b	Elastically modified equilibrium composition in the parent phase	66
C_b^{eq}	The equilibrium composition in the parent phase in the absence of elasticity	66
C_b^{int}	Local equilibrium concentration on the parent side of the interface	22
C_{11}	Notation for elastic modulus with cubic symmetry: Values are presented in dimensionless form (αC_{11})	9
C_{12}	Notation for elastic modulus with cubic symmetry: Values are presented in dimensionless form (αC_{12})	9

C_{44}	Notation for elastic modulus with cubic symmetry: Values are presented in dimensionless form (αC_{44})	9
C_{ijkl}	Elastic modulus tensor	9
C_{int}	Local interfacial concentration	3
D	Thermal diffusion coefficient	16
D_L	Diffusion coefficient in the liquid phase	2
D_S	Diffusion coefficient in the solid phase	2
D_r	Ratio of diffusion between the parent and precipitate phase.	11
D_{eff}	Effective diffusion coefficient	60
G	Gibbs free energy	13
G_{ele}	Corrective term for the strain to the interfacial equilibrium composition	64
H	Nucleation barrier height	52
J	Solute flux	52
L	Latent heat of fusion	14
L_{arc}	The total arc length of a precipitate	36
L_{system}	Total system size along one dimension	36
M_1	A parameter related to the interface kinetic coefficient	39
M_2	A parameter related to the solute diffusivity	39
N	Total nodes in a domain	44
N_{arc}	Number of nodes along a precipitate interface	36
N_{bulk}	Number of nodes in the bulk of the parent and precipitate phases off of the interface	36
N_{total}	Total number of nodes in the domain	37
N_{uni}	Number of nodes on a uniform mesh	43
R	Natural gas constant	49
R^*	Nucleation radius	11
R_p^*	Critical radius of instability for a perturbation mode p	10
R_C	Critical tip radius of the morphological transition criterium	82
R_{trans}^C	Measured radius for the morphological transition	79
S	Speed up factor for the adaptive mesh algorithm	43
S_i	The entropy of phase i	50
T	Local temperature	3
T_M	Melting temperature	13
U	Dimensionless undercooling	13
U_i	Displacement vector in cartesian coordinate i	8

U_r	Radial displacement in spherical coordinates	10
U_{amp}	Amplitude of the anisotropic strain trace	72
V	Velocity normal to the interface	2
V_R^*	Scaled Velocity to a reference velocity	61
V_R	Velocity in units of m/s	61
W_ϕ	Interface width	13
W_o	Isotropic interface width	14
X	A placement for a field value, such as the composition or the phase.	31
Z_i	Prefactors to $g(\phi)^i$ terms in the elastic free energy	66
Δt	Discrete time step	44
Ω	Supersaturation	4
Ω_{el}	Supersaturation modified for elasticity	81
Ψ	Diffusion modulation factor	67
α	Modulation factor to dimensionalize the elastic coefficients into units of the model	67
\bar{V}	Velocity in units of W/τ	61
$\bar{\psi}$	Mean density in the phase field crystal formulation	42
β	Deviation from anisotropy in the cubic elastic coefficients: Values presented are dimensionless as $\alpha\beta$	71
β_k	Interface kinetic coefficient	3
ϵ^*	Hydrostatic eigenstrain	9
ϵ_{ij}^*	Eigenstrain tensor	8
ϵ_{ij}^{el}	Elastic strain	9
ϵ_4	Strength of surface energy anisotropy	14
ϵ_4^C	Critical value for the surface energy anisotropy	75
ϵ_e	Strength of strain anisotropy	22
ϵ_{ele}	Magnitude of the elastic energy anisotropy to the equilibrium composition	79
ϵ_{ij}	Total strain	8
ϵ_{surf}	Magnitude of surface energy anisotropy to the equilibrium composition	79
γ	Surface energy	49
κ	Local interface curvature	3
λ	Phase field constant proportional to the inverse of the nucleation energy	14
μ_i	Chemical potential of phase i	50
ν	Molar volume	49
ω_p	Amplification rate of instability mode p	12

ϕ	Order parameter	13
ρ	Mass density	41
σ_{ij}	Stress tensor	9
τ	Function related to the interface kinetics attachment time	52
τ_o	Interface kinetics attachment time scale	16
θ	Angle	72
$\tilde{q}(\phi)$	Elastically modified two sided diffusion modulating function	68
\vec{n}	Local normal vector of the interface	14
ξ	Overhead for the adaptive mesh	44
a	Precipitate radius	10
a_1	Constant from thin interface asymptotics = 0.8839	17
a_2	Constant from thin interface asymptotics = 0.6267	17
a_i	Lattice spacing of the phase i	9
a_t	Anti-trapping prefactor	52
c_p	Specific heat at constant pressure	14
d_o	Capillary length	3
dt	Discrete increment of time	44
e	Calculated Displacement difference for the Threshold of convergence	91
e'	Threshold convergence criteria	91
e_i	Element Neighbours i	29
f_{el}	Elastic free energy	9
$g(\phi)$	Algebraic function to interpolate through a diffuse interface	14
$h(\phi)$	Function describing the double well potential	14
l_D	Diffusion length	12
l_T	Thermal length	12
m	Liquidus slope	53
n_i	Grid node i	30
p	Mode of instability	11
$q(\phi)$	Function to modulate diffusion coefficients between phases	52
t	Time	2
x	Position	2

DON'T PANIC

I study snowflakes, growing inside of other snowflakes....
except they're made of metal....
and simulated on a computer.

OVERVIEW

The main theme of this thesis is a study of the effects of elasticity on the phase transformation process. I will focus mainly on solid state transformations, but will also touch on some issues regarding solidification, mostly by way of demonstrating new advances that I have made to the phase field methodology that are generic to phase field modeling. My objective is to study and elucidate the mechanisms of growth of solid state dendritic structures and the structures that have come to be known as Widmanstätten precipitates (plates, needles, etc..), to do so by advancing the phase field model developed by Alain Karma [8] to include elasticity (as well as the ability to model non-ideal alloys quantitatively), to implement this model on an efficient adaptive meshing algorithm based on finite differences rather than the slower finite element methods and to investigate the anisotropic nature of elasticity in solids. This thesis is broken down into several chapters. The first chapter in this thesis overviews some of the history of solid state transformations and solidification, elastic effects in phase transformations and phase field models incorporating elasticity. It also details much of the terminology and theoretical background used to develop the models and analyze their results. Chapter 2 describes the adaptive mesh structure, its algorithms and the overall efficiency of the code. The portability of the code is demonstrated by the implementation of the data structure and algorithms to several different projects. Chapter 3 extends an existing phase field model for ideal dilute binary alloys to a model for *non-linear* phase coexistence lines. Another extension to this phase field model which incorporates elastic fields is introduced in Chapter 4 and in Chapter 5 this model is used to look at the competitive effects of elastic anisotropy and surface anisotropy.

Chapter 1

Introduction

This chapter will overview some of the past work done in both experiments on and modeling of phase transformations. First the classical theories of phase transformations and experimental work in Widmanstätten structures and solid state dendrites are outlined. The theory of elasticity is overviewed as it pertains to this thesis and two cases of morphological linear stability theory are discussed, a spherical precipitate in an isothermal melt and a planar front driven in a temperature gradient. The phenomenology of phase field models is then reviewed, in the context of solidification of pure materials and alloys with a discussion of the history and physical connections of the model. Finally, the inclusion of elastic free energies into the phase-field model is shown.

1.1 Solidification and Solid-State Phase Transformations

1.1.1 Sharp Interface Kinetics of Second Phase Formation

The growth of a second phase in a host phase of an alloy, as happens, for example, during the solidification of binary alloys is largely controlled by mass transport, particularly in isothermal conditions. Diffusion of impurities is in turn coupled to the underlying energies of the two phases through their local equilibrium state at the interface¹. This influence is characterized by a phase-diagram of the particular alloy. The simplest binary-alloy phase diagram is shown in figure 1.1.

This diagram is obtained by a Gibb's construction using the free energy of a Cu-Ni mixture at different temperatures. For a given undercooling (quench) into the co-existence region (point B), solidification proceeds while maintaining concentrations corresponding to the liquidus (C_L) and solidus (C_S) for that temperature on either side of the solid/liquid interface, provided that the interface can be maintained at

¹at least for low to intermediate cooling rates

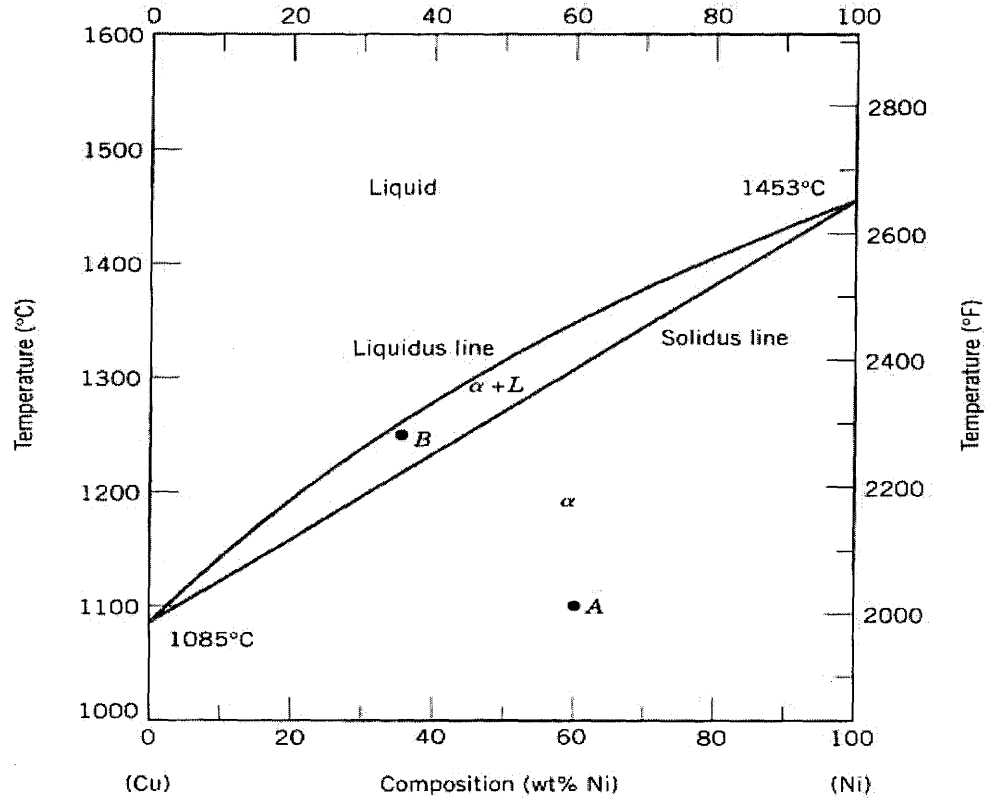


Figure 1.1: Binary phase diagram for CuNi.[95]

equilibrium. The flux of solute across the interface is related to the local normal velocity at the interface, and to C_S and C_L by mass conservation expressed as:

$$D_S \frac{\partial C}{\partial x} \Big|_{x_{int}^-} - D_L \frac{\partial C}{\partial x} \Big|_{x_{int}^+} = (C_L - C_S)V \quad (1.1)$$

where D_S is the rate of diffusion in the solid, D_L is the rate of diffusion in the liquid and V is the local normal velocity of the interface². Diffusion of impurities in bulk phases is governed by Fick's law,

$$\frac{\partial C}{\partial t} = \nabla(D(C)\nabla C(\vec{x})) \quad (1.2)$$

where $D(C)$ is the diffusion function and $C(\vec{x})$ is the local impurity concentration.

The thermodynamic correction due to curvature of the interface is controlled by the effects of surface tension. The equilibrium correction to the interface composition (on either side of the interface) from this effect is described by the Gibbs-

²These also can have curvature corrections to Equation 1.1, although these are typically small.

Thomson condition,

$$\frac{C_{int}(T) - C_j^{eq}(T)}{\Delta C} = -d_o\kappa - \beta_k V \quad (1.3)$$

where j is either the solid (S) or the liquid (L) phases, T is the temperature, d_o is the chemical capillary length, κ is the curvature of the interface and β_k is the interface kinetic coefficient. The capillary length is strictly different on different sides of the interface. This effect will be omitted in this work.

While the kinetics above were introduced in the context of isothermal solidification, their form remains essentially unchanged for solid state precipitate growth. However, other solid state considerations must be included, such as elastic effects, depending on the nature of the solid-solid interfaces. These will be described below, following a review of some relevant solid state precipitation phenomena.

1.1.2 Experimental Studies of Widmanstätten Plates and Needles

The Widmanstätten structure was first observed around 1808 by Alois de Widmanstätten. His name has been used to describe this structure that has been observed to occur in many different alloys. The Widmanstätten structure is formed by the precipitation of a new phase in a solid solution. These precipitates form a network of regular patterns related to the crystallographic nature of both the precipitate phase and the original parent phase, as seen in figure 1.2.

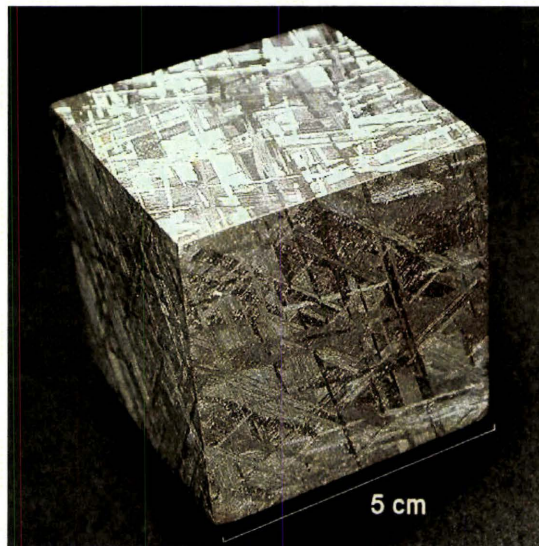


Figure 1.2: Cubic polish of a meteoric iron illustrating the Widmanstätten structure.[1]

The problem of Widmanstätten precipitates is broken down into two areas:

1. The crystallographic mechanism in the precipitation leading to the nucleation of the Widmanstätten precipitates.
2. The factors influencing the growth of the precipitate once nucleation has occurred.

These patterns and their formation was the focus of intense experimental study in the early 1900s. The one commonality found to be shared between all alloys studied, and that which defines the Widmanstätten structure, is that all were found to exhibit similar relationships between the nucleating phase relative to the orientation of the parent phase. These orientational relations can create low energy boundaries. In iron-carbon alloys it is found that the $\{110\}$ plane in the FCC precipitate phases grows parallel to the $\{111\}$ plane in the BCC parent phase. Similarly, orientational relationships are found in both Cu-Zn brass and Al-Cu alloys [76, 75, 58].

The growth rate of the Widmanstätten transformation implies that a slow transfer process is controlling the rate at which the precipitates can grow. The diffusion of a solute species is largely thought to be responsible for the transformation rate. Composition not only controls the transformation rate but also the morphologies of the precipitates nucleated. This can result in either primary plates growing from grain boundaries directly or secondary plates which develop from grain boundary allotriomorphs.

Kirkaldy and Townsend [73] presented experimental evidence detailing the importance of crystallographic orientations between experimental morphologies by showing that certain grain orientation mismatches inhibited the growth of Widmanstätten structures, consistent with the predictions of earlier theories of Mehl et al [76, 75, 58]. More importantly they provided a model for a diffusional shape instability of the secondary plates from the grain boundary allotriomorphs. This model used shape instability theory to calculate the morphological spacings, which were found to be in relatively good agreement with experiments. This theory however excluded the effects of strain energy, grain boundary diffusion and anisotropy in the surface energy. [96, 59]

Investigations into the growth rates have been used to understand the kinetics involved in the formation of the Widmanstätten precipitates. Growth rate prediction models have been developed with varying degrees of success and disagreement regarding the comprehension of the controlling aspects of the precipitate growth.

In 1946 Zener [104] and then in 1957 Hillert [31] produced models for growth rates on diffusion controlled transformations by considering the flux balance at the interface. Both predicted a growth rate proportional to the supersaturation (Ω) assuming that the supersaturation is small ($\Omega \ll 1$).

In 1961 Ivantsov [35] developed a more rigorous model to predict growth rates and this derivation produced rates proportional to the square of the supersaturation

(Ω^2). This derivation assumed an isoconcentrate boundary and neglected curvature on the equilibrium concentrations as well as diffusion. Horvay and Cahn [25] developed a similarly rigorous extension to the Ivantsov model which also predicted growth rates proportional to Ω^2 . But this model also assumed an isoconcentrate boundary and still lacked elastic effects.

In 1969 Trivedi proposed a variant of the Ivantsov model [77, 11] in which the variation of concentration along the interface due to capillarity was small and therefore the interface shape could be approximated by a parabola yet still include a variable concentration along the interface. This model, however, also neglected elastic strain energy and anisotropic surface energy effects. It assumed a dilute alloy capillarity effect and the diffusion coefficient of the solute was independent of the concentration.

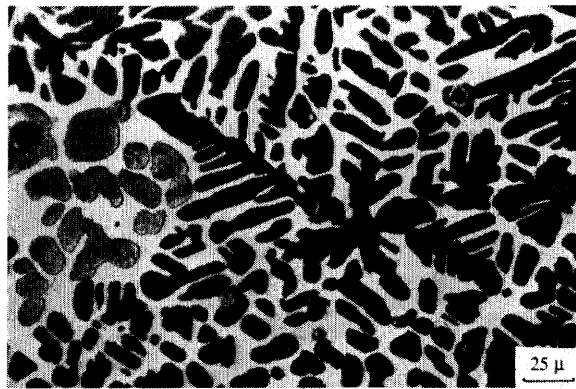
Semi-empirical models have generally given good understanding of some of the basic physics in solidification and solid state transformations. They are however, limited –as any modeling formalism– in several key ways. They generally rely on qualitative geometric constructions. They also usually contain several parameters that need to be fit in order to predict experimental data. They cannot predict growth behavior over the entire range of supersaturations or cooling rates. Moreover, and most importantly, such modeling formalisms cannot be used to self-consistently examine the complex dynamics and pattern formation inherent in microstructure growth. These are all areas where phase field models can help complement previous semi-empirical approaches.

In the 1990s Bhadeshia et al [80] claimed that the transformation process of Widmanstätten plates was a paraequilibrium process in which the plates lengthen at a rate controlled by diffusion but was nevertheless a displacive transformation. Bhadeshia claimed that the transformation was stress controlled due to misfit strains from elastic mismatches between parent and precipitate phases. This growth process would be much like the transformation of martensite, but at rates controlled by the diffusion of the solute. This theory failed in the growth of single plates. Bhadeshia showed that the energy required for the transformation of a single plate was much too high due to strain energy at the plate tip. He therefore concluded that plates must grow in pairs to mutually accommodate this strain energy.

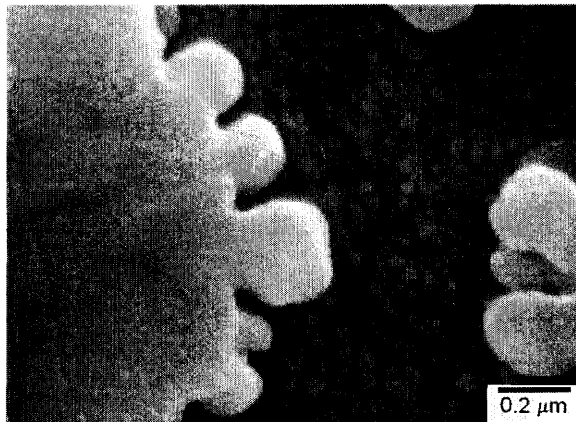
1.1.3 Observations and Conditions for Solid State Dendrites

The appearance of precipitate dendritic structures in the parent phase can be found in solid-state transformations, given that the relationship between the parent and precipitate meet certain properties. A high rate of atomic transfer from the parent phase to precipitate phase, relative to the diffusion of solute ahead of the growth is required. The appearance of dendrites in the solid state can be found if the precipitating phase and the parent phase have similar lattice structures and the transformation is driven by a diffusional process in the presence of an anisotropy.

As with the Widmanstätten structures, there is present a crystallographic mechanism in the precipitation process that leads to the nucleation of a precipitate. This effect and various other factors will also influence the growth process of the precipitate once nucleation has occurred. While there is some investigation into the effects of this crystallographic anisotropy in the process of nucleation [52], the focus of much of this thesis will revolve around the competitive growth process of these precipitates after they have already nucleated. This thesis investigates the mechanism by which coherency and surface energy anisotropy effects can influence the growth process of a precipitate in the solid state.



(a) Solid state dendritic precipitates in Cu-52.7 wt pct Zn [92]



(b) Seaweed-like γ' precipitate in Ni base superalloy[103]

Figure 1.3: Solid State structures for Brass(a) and a Ni base Superalloy(b)

In 1967 Malcolm et al [41] produced experimental solid state dendrites in β brass. The dendrites had semi-coherent interfaces and low energy boundaries. Laraia and Voorhees [38, 93] showed how a coherent precipitate can shift the interfacial composition towards the far field alloy composition, thus reducing the driving force for the transformation. They examined the equilibrium shapes of elastically

coherent particles in an anisotropic matrix. It was found that the particles formed complex geometric shapes determined by the nature of the anisotropy present in the material. Husain et al [92] reviewed a series of experimental materials papers and postulated the following conditions for solid state dendrites to occur(see figure 1.3 (a)):

1. *A solid solution gets supersaturated on cooling and forms precipitates of another solid solution.[92]*
2. *The two phases must have similar crystallographic structures.[92]*
3. *The lattice parameter of the precipitate phase is a simple multiple of the parent phase.[92]*

The three dimensional effects of elastic stress on Ni-Al $\gamma - \gamma'$ precipitates were studied by Lund and Voorhees [12]. Overlapping elastic fields caused by high densities of precipitates was found to be the controlling aspect of the growth process. The morphological instability of precipitates in a nickel base superalloy was investigated by Yoo [103], illustrated in Figure 1.3 (b). It was found that at certain undercooling solid-state precipitates driven by diffusion limited growth would undergo Mullins-Sekerka instability and then evolve into an almost isotropic growth pattern.

Much like solidification, under the proper conditions, nucleated precipitates in the solid state will undergo growth and instability. The morphological development of the particle should be controlled not only by the diffusion in both parent and precipitate phases and anisotropy in the surface energy but also in elastic contributions to the energy, as well as any anisotropic effects due to the elasticity.

Anisotropic driving forces cause precipitates to grow in preferential directions. When two differing anisotropic driving forces coincide, their mutual competition can cause destructive and constructive interference and therefore morphological changes to the resulting dendritic structures during solidification and in the solid state occurs. This effect was illustrated by Provatas et al [63] in solidification by the introduction of a temperature gradient at an angle to the growth direction preferred by surface energy anisotropy. It was found that by changing either the rate of solidification or the angle of the temperature gradient, a transition from dendritic to seaweed structures was forced. Haxhimali et al [85] showed that the introduction of competing surface anisotropies could also destructively interfere producing seaweed like structures in 3 dimensions.

1.2 Basic Theory of Elasticity

A solid state transformation process will inherently involve some sort of elastic strain. This strain will usually involve a lattice mismatch at the interface or a volu-

metric change of the precipitate size. Presented here is the basic elastic theory that is used in the analyses later in this thesis.

The first element of elasticity theory [23] is the definition of the displacement field U_i , where i is a cartesian coordinate(x,y,z). U_i is a vector that defines the displacement of atoms or the displacement of any point P in a strained body from its original position to the position P' in the strained state, illustrated in figure 1.4.

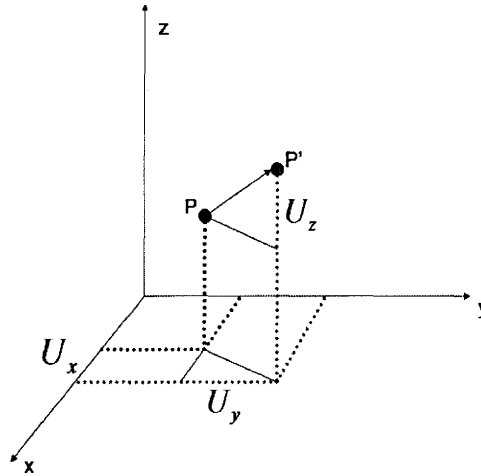


Figure 1.4: The displacement of position P to position P' broken down into orthogonal components U_x, U_y and U_z .

When a deformation occurs the distances between two local points change. The relative change between two points undergoing displacement is defined by the strain ϵ_{ij} .³ For small changes in relative displacement, linear elasticity can be assumed and the strain is given as [23],

$$\epsilon_{ij} = \frac{1}{2} \left(\frac{\partial U_i}{\partial x_j} + \frac{\partial U_j}{\partial x_i} \right) \quad (1.4)$$

Lattice mismatches at interfaces, composition and temperature variation, and volumetric changes can be characterized by eigenstrains (ϵ_{ij}^*), a state in the material that has a different relaxed strain state than that of the reference material. For a hydrostatic eigenstrain (ie no shear component) the eigenstrain tensor can be characterized by placing 0 values at all points in the eigenstrain tensor except on the diagonal. This can be defined as [19, 45]

$$\epsilon_{ij}^* = \epsilon^* \delta_{ij} \quad (1.5)$$

³Einstein notation is used in this thesis. Summation conventions apply to repeated suffixes.

where $\epsilon^* = \frac{a_\alpha - a_\beta}{a_\alpha}$ for a lattice mismatch and a_i is the lattice parameter for the α and β phases.

As a driving force in phase transformations, elastic strain is the strain relative to the relaxed state of the current phase. This defines the elastic strain as [23]

$$\epsilon_{ij}^{el} = \epsilon_{ij} - \epsilon_{ij}^* \quad (1.6)$$

and the stress is therefore computed as [23]

$$\sigma_{ij} = C_{ijkl}\epsilon_{kl}^{el} = C_{ijkl}(\epsilon_{kl} - \epsilon_{kl}^*) \quad (1.7)$$

where C_{ijkl} is the elastic modulus tensor and is related to the lame constants λ and μ for an isotropic linear elastic solid as [72] $C_{ijkl} = \lambda\delta_{ij}\delta_{kl} + \mu(\delta_{ik}\delta_{jl} + \delta_{il}\delta_{jk})$.⁴ For square symmetry in 2 dimensions, $C_{11} = C_{xxxx} = C_{yyyy}$, $C_{12} = C_{xxyy} = C_{yyxx}$ and $C_{44} = C_{xyxy} = C_{yxxy} = C_{yxyx} = C_{xyyx}$.

The elastic free energy is calculated from the elastic strains and stress in the system through Hooke's law and is defined to be [23]

$$f_{el} = \frac{1}{2}\sigma_{ij}\epsilon_{ij}^{el} = \frac{1}{2}C_{ijkl}(\epsilon_{kl} - \epsilon_{kl}^*)(\epsilon_{ij} - \epsilon_{ij}^*) \quad (1.8)$$

The equilibrium stress state of the material can be calculated by assuming that a control volume is in static equilibrium along each set of orthogonal stresses, in general this is described by the tensor equation

$$\nabla_i\sigma_{ij} = 0 \quad (1.9)$$

and in two dimensions this results in the following simultaneous equations (by using repeated summation),

$$\begin{aligned} \frac{\partial\sigma_{xx}}{\partial x} + \frac{\partial\sigma_{xy}}{\partial y} &= 0 \\ \frac{\partial\sigma_{yy}}{\partial y} + \frac{\partial\sigma_{yx}}{\partial x} &= 0 \end{aligned} \quad (1.10)$$

Eshelby produced an analytical solution to these equations in three dimensions for isotropic elliptical particles with a hydrostatic eigenstrain (ϵ^*) [17, 72]. For a spherical inclusion the displacement for a point outside the inclusion was found to be,

$$U_r(r) = \frac{\epsilon^*a^3}{3r^2} \frac{3\lambda + 2\mu}{\lambda + 2\mu} \quad (1.11)$$

⁴ $\delta_{ij} = 1$ if $i = j$ and 0 otherwise.

and for a point inside the inclusion,

$$U_r(r) = \frac{\epsilon^* r}{3} \frac{3\lambda + 2\mu}{\lambda + 2\mu} \quad (1.12)$$

where λ and μ are the lame coefficients and a is the particle radius. Similarly for a 2-D circular inclusion it is expected that these solutions would be proportional to $U_r(r) \propto \frac{a^2}{r}$ outside the precipitate and $U_r(r) \propto r$ inside the precipitate. The total elastic energy of the inclusion was solved and found to be $\propto \epsilon^{*2} a^3$ in 3-D and is expected to be $\propto \epsilon^{*2} a^2$ in 2-D.

1.3 Formation of Instabilities on Precipitate Interfaces - Linear Stability Analysis

As interfaces move during phase transformations instabilities can form from minor fluctuations in the continuum fields. These fluctuations are usually due to small amounts of thermal "noise" arising at the atomic level. In the linear stability analysis by Mullins and Sekerka, it is the diffusion away from an interface that drives instability, balanced against the stabilizing force of surface tension. Instabilities can also be amplified by strain fields where the reduction of strain energy becomes the driving force for the instability, a situation known as the ATG (Asaro-Tiller-Grinfeld) instability [5, 55, 40].

The transition from planar to unstable fronts is well documented and is important in nearly all microstructure phenomena.

1.3.1 Mullins-Sekerka Instability Theory for an Isothermal Precipitate

In 1963 Mullins and Sekerka [60] analyzed the moving interface of a growing sphere to characterize the instability modes as the sphere grew in an undercooled melt. Applying a spherical harmonic perturbation to the interface and applying the boundary conditions (Equations 1.1 and 1.3) to the perturbations, they calculated the fastest growing mode of instability and also the critical radius at which a growing sphere will become unstable to linear order in the perturbation [60, 53]. This radius, R_p^* is given as,

$$R_p^* = R^* \left(1 + \frac{1}{2} \left(1 + \frac{1}{p} + D_r \right) p(p+2) \right) \quad (1.13)$$

where D_r is the ratio of the diffusion in the parent phase and the precipitate phase, p is the mode of the instability⁵ and R^* is the nucleation radius approximated by

$$R^* = \frac{2d_o}{\Omega} \quad (1.14)$$

where d_o is the capillary length and Ω is the supersaturation or undercooling. Figure 1.5 shows a plot of the instability criterion in Equation 1.14. A cooling path can be followed to either cause (Path 1 in Figure 1.5) or hinder (Path 2 in Figure 1.5) the instability of the interfacial region.

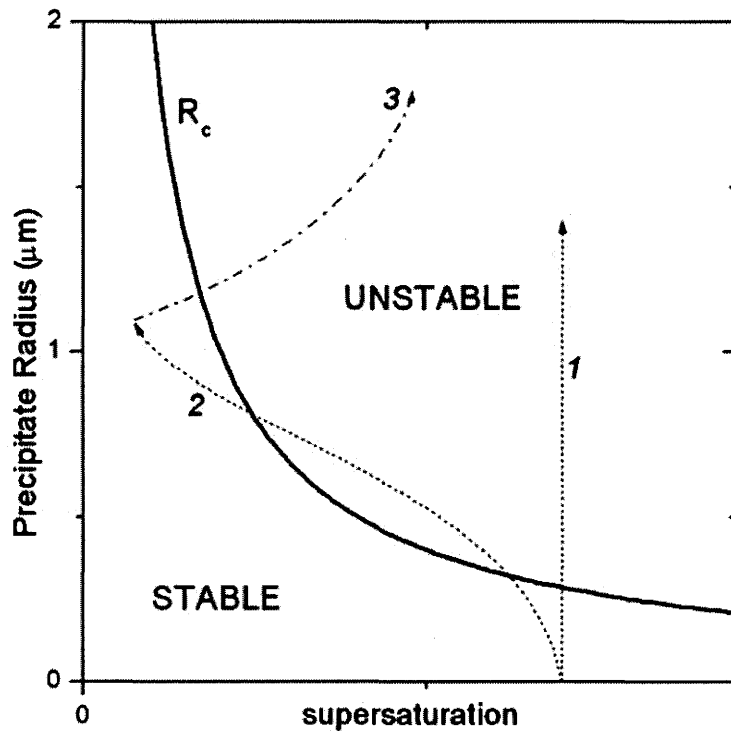


Figure 1.5: *Stability plot [60] illustrating regions of precipitate stability and instability. Precipitates can follow growth paths that maintain stability by decreasing the supersaturation during precipitate growth. Contrarily the precipitate can be plunged into a region of instability via quickly increasing the supersaturation achieved by changing the temperature .*

⁵ $p = 2$ is the minimum mode to become unstable, $p = 1$ represents a simple translation of the precipitate.

1.3.2 Linear Stability of Planar Fronts in a Temperature Gradient

A planar front advancing into a temperature gradient can also undergo a transition from planar to non-planar growth. Mullins and Sekerka [60] and later Langer [53] solved the steady state diffusion equation and applied the boundary conditions 1.1 and 1.3. By doing so Langer was able to calculate the amplification rate ω_p for different perturbation modes p of an interface, where the wavelength $\lambda = \frac{2\pi}{p}$. An example of this is illustrated for directional solidification where the solid diffusion rate was zero. In this case the amplification rate is

$$\omega_p = \frac{2D}{l_D^2} \left((ql_D - 2 + 2k) \left(1 - \frac{1}{v'} - \frac{1}{2}d_o p^2 l_D - \frac{2k}{ql_D - 2 + 2k} \right) \right) \quad (1.15)$$

where d_o is the capillary length, p is the perturbation mode of the instability, D is the diffusion coefficient, k is the partition coefficient, $v' = 2l_T/l_D$, $ql_D = 1 + \sqrt{1 + (kl_D)^2}$, $l_D = \frac{2D}{V}$ and $l_T = \frac{m_l C_o^l (1-k)}{G}$ are the diffusion and thermal lengths respectively, m_l is the liquidus slope, G is the thermal gradient and V is the rate at which the gradient is pulled into the melt.

A plot of the amplification rate ω_p vs the perturbation frequency p , as shown in figure 1.6, can be used to determine not only the selected wavelength ($\frac{2\pi}{p}$) but also the condition for interfacial stability. The interface is stable when all possible modes result in negative growth amplification, shown by the $v' = 0.7$ plot in Figure 1.6. The interface becomes unstable for conditions that cause any modes to have positive amplification rates. This stability criteria was determined to be point at which the peak of the amplification curve touches the the axis. This is illustrated by the $v' = 1.05$ curve in Figure 1.6.

1.4 Phenomenology of Phase Field Modeling

In recent years, the phase field method has emerged as a standard and powerful tool to tackle free-boundary problems. This method has the advantage that it avoids explicit front tracking by making phase boundaries spatially diffuse through the use of order parameters that vary continuously across interfaces. However, the multi-scale nature of solidification and other phase transformations makes it difficult to use phase-field models *quantitatively* due to the computational complexity associated with making the solid-liquid interface thin enough to mimic the desired sharp-interface limit. The phase field methodology and new advances that have helped to overcome some of the traditional problems of phase field models will be discussed next (as well as later in the Thesis).

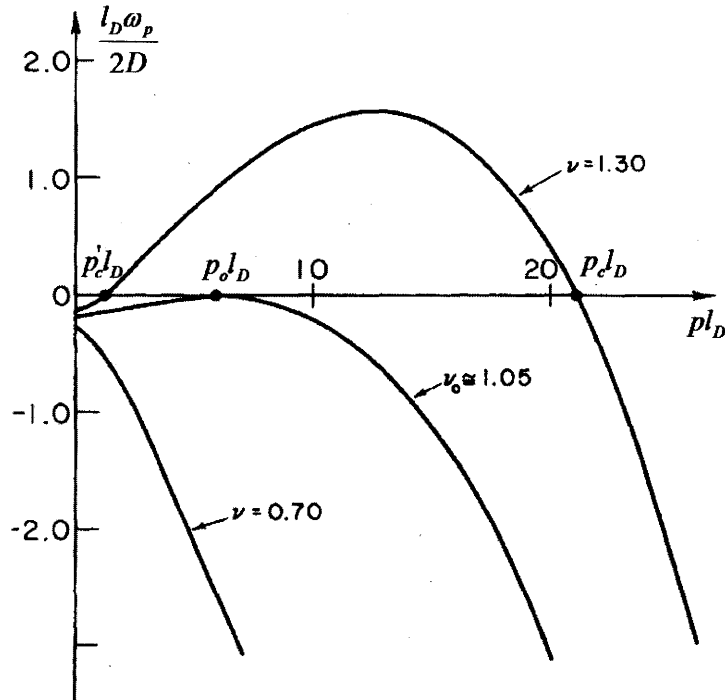


Figure 1.6: Amplification rate(ω_p) plotted vs wave number p for 3 different velocities. An unstable interface, the stability criteria and a stable interface are all shown[53].

1.4.1 General Phase Field Concepts - Solidification of a Pure Material

A brief review of the phase-field method will be used to introduce the concepts pertaining to a phase field by examining the well-documented case of the solidification of a pure material.[16, 67, 61, 63, 86, 22, 49, 102, 15, 32] The phase field method begins with a phenomenological free energy (G) of the solid-liquid system expressed in terms of the temperature and the order parameter field $\phi(x)$, which takes fixed values in either phase (e.g. $\phi = -1$ in the liquid and $\phi = 1$ in the solid) and continuously interpolates between these values across a thin interface whose width scales with the length W_ϕ . The interface is defined as the level set of points satisfying $\phi(\vec{x}, t) = C_i$, where $-1 < C_i < 1$ [22]. A form of G for a pure material is given by

$$G[\phi, U] = \int (|W_\phi(\vec{n})\nabla\phi|^2 + h(\phi) - \lambda U g(\phi))dV \quad (1.16)$$

where $U = (T - T_M)/(L/c_p)$ is the dimensionless temperature field, T_M is the

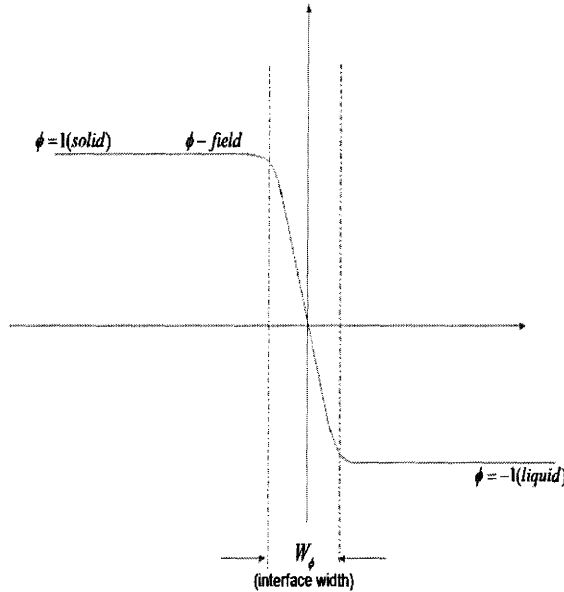


Figure 1.7: Schematic of an interface of the phase field in 1D. The solid phase has a value of $\phi = 1$, followed by a smooth transition through the interface and a value of $\phi = -1$ in the liquid.

melting temperature, L is the latent heat of fusion and c_p is the specific heat at constant pressure. The constant λ is proportional to the inverse of the nucleation energy. In cases where we are not concerned with modeling nucleation kinetics but, rather, the kinetics of dendritic growth, λ can be treated as a free parameter, which is used to "tune" the parameters of the phase field model to emulate an appropriate sharp interface model. The gradient energy term $|W_\phi(\vec{n})\nabla\phi|^2$ controls the surface tension energy, made anisotropic through the function $W_\phi(\vec{n}) = W_o A(\vec{n})$, [49, 102] where \vec{n} is the local normal to the interface and W_o denotes the isotropic liquid-solid interface width. A typical form often used for $A(\vec{n})$ is given by

$$A(\vec{n}) = (1 - 3\epsilon_4) \left(1 + \frac{4\epsilon_4}{1 - 3\epsilon_4} (n_x^4 + n_y^4 + n_z^4) \right) \quad (1.17)$$

where ϵ_4 controls the 4-fold anisotropic strength [22, 102, 15, 94, 43, 10, 8, 14]. Equation 1.17 was originally introduced phenomenologically. More recently, this form and corrections to it have been obtained from first principles calculations using density functional theory [78]. The function $h(\phi) = -\frac{\phi^2}{2} + \frac{\phi^4}{4}$ is the "double-well" potential that separates the energy between the solid and liquid phases. The function $g(\phi)$ is an algebraic function that assumes the limits $g(\pm 1) = \pm 1$ and $g'(\pm 1) = 0$. In the sharp interface limit of phase-field models, the specific form of $g(\phi)$ in the

interface is not important, as all that enters the analysis are its limits at $\phi = \pm 1$ [22, 49, 8, 14, 6]. A convenient choice for the interpolation function $g(\phi)$, which maintains the bulk phases at $\phi = \pm 1$, is given as

$$g(\phi) = \frac{15}{8} \left(\phi - \frac{2\phi^3}{3} + \frac{\phi^5}{5} \right) \quad (1.18)$$

The form of the bulk free energy density $g(\phi) - \lambda U(T)g(\phi)$ is shown in figure 1.8, which illustrates the relative changes in the free energy between the bulk solid($\phi = 1$) and liquid($\phi = -1$) as the temperature changes.

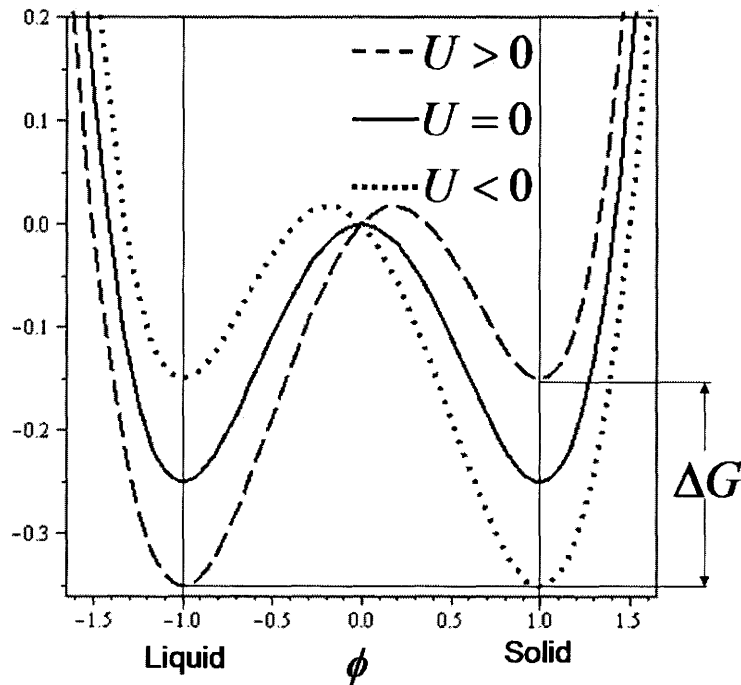


Figure 1.8: Free energy density for a pure material. Solid Line: Energetically both solid and liquid phases are favoured. Dotted Line: The case for $T < T_M$ resulting in the well shifting toward the solid. Dashed Line: The case for $T > T_M$ resulting in the well shifting to the liquid.

The evolution equation for ϕ is described by dissipative minimization of the free

energy, expressed as

$$\begin{aligned} \tau(\vec{n}) \frac{\partial \phi}{\partial t} &= -\frac{\delta G}{\delta \phi} \\ &= W_{\phi}^2(\vec{n}) \nabla^2 \phi + \phi - \phi^3 - \lambda U (1 - \phi^2)^2 \\ &\quad + W_o \frac{1}{2} \nabla \cdot \left(|\nabla \phi|^2 \frac{\partial A^2(\vec{n})}{\partial (\nabla \phi)} \right) \end{aligned} \quad (1.19)$$

where $\tau(\vec{n}) = \tau_o B(\vec{n})$ represents the anisotropic interface kinetics attachment time scale, with τ_o a constant. It's value scales with the atomic mobility [64]. When the function $B(\vec{n}) = A(\vec{n})$, it is possible to simulate the limit of $\beta = 0$ of the sharp interface model, even for large ratios of the interface width to the capillary length $\left(\frac{W_o}{d_o}\right)$ [49].

The evolution of ϕ is coupled to the dynamics of the temperature field via a modified form of the heat diffusion equation

$$\frac{\partial U}{\partial t} = \nabla \cdot (D \nabla U) + \frac{1}{2} \frac{\partial \phi}{\partial t} \quad (1.20)$$

where D here is the thermal diffusion coefficient. The second term on the right hand side of Equation 1.20 represents the latent heat released during solidification, as illustrated in Figure 1.9. This form "smears" the latent heat across the diffuse region of the interface, and reduces to a delta function source in the sharp-interface limit $W_o \rightarrow 0$. Equation 1.20 was originally derived from a condition of entropy growth during a phase transformations [74, 81]. Equations 1.19 and 1.20 can be

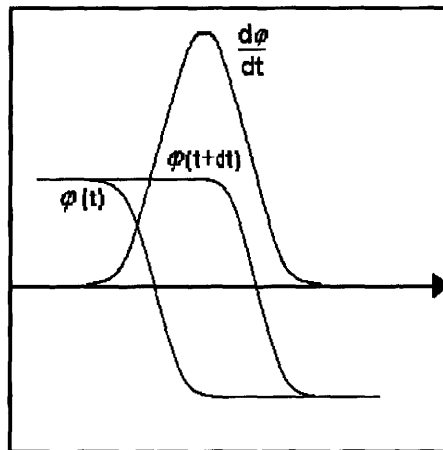


Figure 1.9: Schematic of an advancing interface. The interface advances essentially as a propagating front. The quantity $\partial \phi / \partial t$ represents a normalized quantity of heat released at the interface.

conveniently studied in dimensionless form by rescaling space as $x \rightarrow x/W_o$ and time as $t \rightarrow t/\tau_o$. In that case we can treat $\tau_o = W_o = 1$ in equation 1.19 while $D \rightarrow D\tau_o/W_o^2$ in equation 1.20.

The parameters of the phase-field model can be selected to recover the dynamics of the sharp interface limit. This can formally be achieved by letting $W_o \rightarrow 0$ and $\lambda \rightarrow 0$, such that $\frac{W_o}{\lambda} \propto d_o$ and $\frac{\tau_o}{\lambda W_o} \propto \beta_k$ [14, 15]. In simulating the important case of $\beta_k = 0$, use of these relationships would require that the simulation time scale τ_o become prohibitively small. This asymptotic limit is of little practical value when there is a significant disparity between the capillary length d_o and the diffusion length $\frac{D}{V}$. Since the interface width is of order $10^{-9}m$, this precludes simulation of large-scale dendritic structures over a significant amount of time.

An improvement was developed for the mapping of the phase-field model to the sharp interface model for equal thermal conductivities in both the solid and liquid phases. [49]. That work showed that the sharp-interface limit can be faithfully reproduced if the interface width (W_o), the kinetics time(τ_o), and the coupling parameter(λ) are inter-related according to

$$d_o = a_1 \frac{W_o}{\lambda} \quad (1.21)$$

and

$$\beta = \frac{a_1 \tau_o}{W_o \lambda} \left(1 - a_2 \lambda \frac{W_o^2}{D_L \tau_o} \right) \quad (1.22)$$

where a_1 and a_2 are constants that depend on integrals of the steady-state phase-field function ϕ_o . For the choice of the phase-field free energy described above, $a_1 = 0.8839$ and $a_2 = 0.6267$. The remarkable feature of equation 1.22 is that it allows for the simulation of $\beta_k = 0$ for large values of the ratio $\frac{W_o}{d_o}$ merely by choosing an appropriate interface kinetics time scale τ_o .

1.4.2 Dilute Ideal Binary alloys: Innovations for Working with Diffuse Interfaces

For the case of binary alloy solidification in metals, in which the solute diffusion coefficients of different phases can vary by several orders of magnitude, the situation is far more complex than in pure materials. A second order matched asymptotic analysis (ie. a boundary layer analysis) of various two-sided alloy phase field models [6, 48, 8, 62] reveals that their thin interface limit gives rise to three "correction" terms to the standard sharp-interface models of solidification (described by the same kinetics reviewed in Section 1.1.1). Two of these "correction" terms emerge precisely due to the two-sidedness of diffusion. In the limit of rapid solidification, where the diffusion length of impurities becomes comparable to the

interface width, these corrections define physically relevant corrections to the usual sharp interface models of solidification [65, 36]. At low solidification rates, however, these corrections are not relevant, and their influence –inherent in all phase field models– must be eliminated, particularly if diffuse interfaces are to be used for efficient computations.

For the specific case of a dilute, ideal, two-sided binary alloy, a method for eliminating the thin interface corrections introduced by the diffuseness of the phase field was recently calculated by Karma and co-workers [48, 8]. The phase field free energy for a dilute ideal binary alloy used by Karma and co-workers is

$$G(\phi, c, T) = \int_{dV} \left[\frac{\gamma}{2} |\vec{\nabla}\phi|^2 + f(\phi, T_m) + f_i(\phi, C, T) \right] \quad (1.23)$$

where as with the pure model, ϕ and T are the phase field and temperatures and C is introduced to the phase field model as the composition. The function $f(\phi, T_m)$ is defined to be

$$f(\phi, T_m) = H \left(-\frac{\phi^2}{2} + \frac{\phi^4}{4} \right) \quad (1.24)$$

and is the double well potential where H is the strength of the nucleation barrier. For a dilute ideal alloy the bulk energy ($f_i(\phi, C, T)$) is

$$f_i(\phi, C, T) = f^A(T_m) - S_i(T - T_m) + \frac{RT}{\nu} (C \ln(C) - C) + \epsilon_i C \quad (1.25)$$

where i represents either the solid state or liquid state, R is the gas constant and ν is the molar volume. The phase dependent entropy is $S(\phi) = \frac{1}{2}(S_a + S_b - \frac{L}{T_m} g_2(\phi))$ and the phase dependent enthalpy of mixing is $\epsilon(\phi) = \frac{1}{2}(\epsilon_a + \epsilon_b + (\epsilon_a - \epsilon_b)g_1(\phi))$. g_1 and g_2 are interpolation functions through the diffuse interface with the limits of $g_i(\phi = \pm 1) = \pm 1$ and the derivative limit of $g_i(\phi = \pm 1) = 0$.

The evolution equation for ϕ is described by dissipative minimization of the free energy, expressed as

$$\tau \frac{\partial \phi}{\partial t} = -\frac{\delta F}{\delta \phi} \quad (1.26)$$

and the dynamics of the composition field via a Fickian diffusion equation as,

$$\frac{\partial C}{\partial t} = D_L \nabla \cdot (q(\phi) C \nabla \mu) \quad (1.27)$$

where D_L is the liquid diffusion coefficient and $q(\phi)$ interpolates the liquid diffusion coefficient into the solid phase through the interface.

Having redefined the variables to

$$u = \ln \frac{2C}{C_l^o(1+k - (1-k)h(\phi))} \quad (1.28)$$

where C_l^o is the equilibrium composition on the liquid side of the interface, $h(\phi)$ is an interpolation function which is set to $h(\phi) = \phi$ and k is the partition coefficient $k = \frac{C_s^o}{C_l^o}$, Karma et al [48] wrote the phase field equations in a compact form as,

$$\begin{aligned} \tau \partial_t \phi &= W^2 \nabla^2 \phi - f'(\phi) - \frac{\lambda}{1-k} g'(\phi) (e^u - 1) \\ \partial_t C + \vec{\nabla} \cdot \vec{j} &= 0 \end{aligned} \quad (1.29)$$

where λ has the same relationship to the capillarity (d_o) and kinetic time (τ) as defined in section 1.4.1 and the flux (j) is written as,

$$\vec{j} = -DCq(\phi)\vec{\nabla}u - a_t WC_l^o(1-k)e^u \partial_t \phi \frac{\vec{\nabla}\phi}{|\vec{\nabla}\phi|} \quad (1.30)$$

where the first term is the standard Fick's law for diffusion and the second is an anti-trapping current that corrects for diffusion through an overly diffuse interface. This term is controlled by the anti-trapping coefficient (a_t) and is related to the difference in diffusion in the bulk phases by,

$$a_t = \frac{(h(\phi) - 1)(1 - q(\phi))}{\sqrt{2}(\phi^2 - 1)} \quad (1.31)$$

where $q(\phi)$ interpolates the diffusion coefficients through the two phases. i.e. for $h(\phi) = \phi$ and one sided diffusion $q(\phi) = \frac{1-\phi}{2}$ the coefficient becomes $a_t = \frac{1}{2\sqrt{2}}$ and for equal diffusion ($q(\phi) = 1$) $a_t = 0$.

The anti-trapping technique has also been extended to the study of non-isothermal solidification of dilute ideal binary alloys by Ramirez and co-workers [42]. This situation exploits the fact that thermal diffusion relaxes on time scales several orders of magnitude faster than solute diffusion. This allows the temperature at the interface to be treated as quasi-statically "frozen" in time relative to the dynamics of solute segregation, thus allowing the dynamics of the solute diffusion to be evolved/corrected using the anti-trapping flux technique developed in Refs. [48, 8]. Similar approaches can also be utilized to couple phase field models of alloy solidification to other fast fields, such as electrostatic, and elastic fields.

More recently still, the anti-trapping technique was also extended to the study of quantitative modeling of pattern formation in eutectic (i.e. two-phase) solidification by Folch and Plapp Ref. [71]. At the core of their approach is an idealized triple-well potential that approximates the free energy of each of three phases with an

identical quadratic well. Following analogous approach to Ref. [8], the free energy parameters are chosen such as to decouple the steady state phase and concentration fields between any two coexisting phases. This gives rise to a phenomenological form of the equilibrium chemical potential to any experimental value through the equilibrium of the two solidus and liquidus coexistence lines of any particular eutectic phase diagram. These features, along with the use of an anti-trapping current acting at the two solid-liquid interfaces allows eutectic growth to be simulated efficiently and true to the sharp interface kinetics, even with rather diffuse phase field interfaces.

Chapter 3 will return to the specific binary alloy model of Karma and co-workers, showing several new features that we have made to the model, which make it possible to study alloys with non-linear co-existence curves, i.e. non-ideal binary alloys. Chapter 4 will then extend this model further to handle elastic effects.

1.5 Phase Field Modeling with Elasticity

Borrowing from ideas developed originally for solidification, the phase field methodology has also rapidly developed in the area of solid state transformations. This work is broken down into several categories; the study of elastically driven instabilities, primarily A-T-G instabilities [5, 55], the study of cracking behaviour, the effect of dislocations on interface migration and diffusion in the solid state, and the morphological patterning of precipitates in the presence of elastic fields.

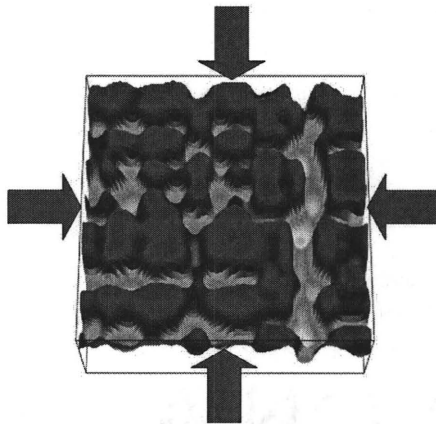


Figure 1.10: *Island morphology of a stressed solid in contact with its melt. The equivalent unstressed solid results in a purely stable planar front.[46]*

Phase field models to study thin film instability from lattice induced strain and strained solids in the presence of their melt have been developed [46, 47, 99, 100, 39] to study the instability relationship to the applied and internal strain fields.

Kassner [46, 47] developed a phase field model that, in the sharp-interface limit, recovered the equations describing the A-T-G instability. This instability is illustrated in Figure 1.10 where a stable planar front becomes unstable with an applied stress. In the course of their study of the instability, they examined the additional effect of body forces, such as gravity, and found a system of period doubling in the patterning process.

Kessler and Levine [20] introduced the development of the phase-field model to the study of crack development and in particular used this model to provide insight into how a crack velocity is actually determined based on short scale dissipation. Karma, Kessler and Levine[2] further developed the phenomenological continuum model for a mode III fracture and reported two-dimensional simulations that yielded a function for the steady state crack velocity. Wang [87] used their phase field model to study the effect of multiple voids and cracks in both single crystals and polycrystals. Dislocations and precipitates were trivially included into their model. In 2004 Henry and Levine [27] studied the properties of fracture using biaxial strain with a phase field model.

Dislocations can have profound effects on phase transformations in the solid state and influences the effect of solute segregation. In 2001 and 2002 Hu and Chen [82, 83] examined the effect of solute segregation and the nucleation of coherent precipitates in the presence of dislocations. In 2002 Koslowski et al [57] studied dislocation dynamics, investigating effects such as hardening. Rodney [18] investigated the motion of dislocations due to elasticity in a microstructure of late stage $\gamma - \gamma'$ and Haataja and Leonard [56] and Hu and Chen[84] investigated the effects of dislocations on phase separation.

In 1995 Morin [9] proposed a phase field model for the simulation of the transformation of amorphous solids undergoing order-disorder transformations. Jou [37] incorporated elastic energies into phase field models for the solid state. They qualitatively illustrated how the application of anisotropic external source strains affected the precipitate and parent phases with isotropic elastic coefficients. After applying these anisotropic stresses, initially isotropic precipitates instead grew in strictly anisotropic morphologies.

Bouar [97] looked at the origin of chessboard structures in coherent decomposition of alloys using a phase field model with elasticity and Aguenou [45] proposed a model with elasticity to explain the quasi-dendritic growth of cobalt on a platinum surface. The elastic anisotropy of the lattice strain was found to have a profound impact on the morphology of the domain growth. Wang [88, 89] proposed a phase field model for three dimensional solid state precipitates with arbitrary elastic inhomogeneities, the model was later extended to investigate the effect of free surfaces on martensitic transformations [90].

Solid state plate growth was studied by Vaithyanathan [91]. They presented a phase field model to study the coarsening of θ' precipitates in $Al - Cu$ alloys incorporating elastic fields to elucidate the effects of the various energetic contributions

on the equilibrium shapes of the particles. Their particular form for the surface energy resulted in lens shaped precipitates, while the addition of anisotropic elasticity caused their precipitates to maintain a more rectangular shape. Zhu [44] similarly studied the coarsening kinetics of solid state precipitates by studying γ' precipitates in $Ni - Al$ alloys. Mecozzi [24] used a phase-field model to simulate the $\gamma \rightarrow \alpha$ transformation in $C - Mn$ steel and Lu [98] detailed the effects of elasticity on the morphology of γ' precipitates in $Ni - Al$ alloys. Yeon [101] presented a model for the study of morphological evolution of second phase particles that were coherently precipitated in the parent phase. They also included the sharp interface asymptotics of the elasticity showing that in the thin interface limit, the elasticity is decoupled from the effect of the capillarity and interface kinetics at least to first order. Their simulations showed that relatively isolated precipitates grew as solid state dendrites, whereas a material of densely packed precipitates would fail to become unstable and quickly grew to an equilibrium square shape morphology.

Elasticity in most of these models has been incorporated into phase field models by the addition of phase dependent elastic free energies such as the form in Equation 1.8. [46, 37, 45, 88, 91, 101, 34] By the introduction of strain sources, such as the eigenstrain ϵ_{ij} , and making the elastic modulus tensor C_{ijkl} depend upon the order parameter ϕ , the dynamical evolution of strain field, order parameter (i.e. phase field) and concentration field are simply given by simultaneously solving Equations, 1.9, 1.19 and 1.20.

This addition to the free energy adds an additional corrective term to the Gibbs-Thomson condition (Equation 1.3) [69]. Including the effects of anisotropy the Gibbs-Thomson relationship can be written as,

$$C_b^{int} = C_b^{eq} - \Delta C_{capillarity}(1 + 15\epsilon_4 f(\theta)) - \Delta C_{elastic}(1 - \epsilon_e h(\theta)) \quad (1.32)$$

where $f(\theta)$ and $h(\theta)$ are trigonometric functions of the interface normal direction. ϵ_4 and ϵ_e are the corresponding strengths of these anisotropies, while $\Delta C_{capillarity}$ and $\Delta C_{elastic}$ are the isotropic corrections to the interfacial composition of the capillarity and elastic strain respectively. The values of $\Delta C_{capillarity}$ and $\Delta C_{elastic}$ are presented in chapter 5 for a cubic elastic modulus tensor.

For a two phase system the elastic modulus tensor is interpolated from phase to phase by a function (as in section 1.2.1) which has the limits such that $g(\phi = \pm 1) = \pm 1$ (where it is recalled that $\phi = \pm 1$ denotes the order parameter in the two bulk phases). The elastic tensor, thus defined for two phases, becomes,

$$C_{ijkl} = \frac{1 + g(\phi)}{2} C1_{ijkl} + \frac{1 - g(\phi)}{2} C2_{ijkl} \quad (1.33)$$

where $C1_{ijkl}$ are the elastic tensors in each respective phase. Correspondingly the

eigenstrain sources can be made phase dependent as,

$$\epsilon_{ij}^* = \frac{1 + g(\phi)}{2} \epsilon_{ij}^{*1L} + \frac{1 - g(\phi)}{2} \epsilon_{ij}^{*2L} \quad (1.34)$$

for two phases, where ϵ_{ij}^{*L} is the lattice eigenstrain.

As mentioned earlier, Chapter 4 will make use of this phenomenology in an alloy phase field model, which will then be used to report new results on solid state morphological transitions.

This chapter introduced thermodynamic aspects of the phase field phenomenology and discussed its connections to solid state transformations and solidification. The following chapters report on new contributions made in this thesis. These include new phase field formulations for solidification and/or elasticity, novel methods of solving phase field models computationally and applications of the phase field method to solid state transformations and solidification.

The next chapter begins by delving into the subtle and all too often unappreciated details of numerical solution methods and their efficiency for phase field models in all areas of materials science. This is a necessary first step without which quantitative modeling with this approach is impossible.

Chapter 2

Multi-Scale Modeling and The Adaptive Meshing Technique

A finite difference adaptive mesh technique is used to approximate the partial differential equations solved in the models that will be presented in chapters 3 and 4. This chapter will describe the data structure for a new dynamic adaptive mesh refinement (AMR) algorithm to solve coupled transient (diffusion-type phase-field) and time-independent (elastic equilibrium) equations. It will go beyond the AMR technique introduced by Provatas et. al.[68] by using the finite difference (FD) method rather than the finite element method (FEM) as the primary solution method. This will be shown to increase the portability of the technique allowing many new models using higher order derivatives to be simulated with minimal interaction with the code structure. This new multi-scale technique is demonstrated on two very different solidification microstructure phenomena.

2.1 Multi-Scale Modeling

The simplest method of computing time dependent solutions of phase-field equations is to solve the partial differential equations using an explicit finite difference method and to update each nodal point in a uniform mesh by explicit time stepping. However, the typical interface width of a material undergoing a phase transformation is of the order of 10^{-9} to 10^{-8} m while the final microstructure size can be on the order of 10^{-4} m or larger. This length scale disparity can result in as much as 5 – 6 orders of magnitude difference during the phase transformation process. Limiting the simulation to a two dimensional problem can generate a static uniform mesh with as many as 10^{12} nodal points. This results in unrealistically long computation times and memory management becomes almost impossible. Two methods each independently can decrease this nodal count by several orders of magnitude. First is the technique by which to widen the interface while maintaining realistic interface kinetics such as was discussed in section 1.4.1 and secondly a numerical

method which dynamically increases the nodal count efficiency by taking advantage of the physical aspects of multiscale phase transformation problems. Such a numerical method is discussed and further developed in this chapter.

The nodal count efficiency can be increased by decreasing the number of nodes in regions where a high density of nodes is not required to gain the numerical accuracy required for the simulation. In phase transformations, this typically occurs in regions away from the interface. By allowing a mesh to dynamically change its resolution from a higher resolution to a lower resolution in regions where such grid resolution is not required can save both computation time and computer memory. This method of numerical efficiency applies to any problem where

$$\frac{Interface\ Length(or\ Area)}{Domain\ Area(or\ Volume)} \ll 1 \quad (2.1)$$

such as in solidification and solid state transformations.

A dynamic adaptive mesh routine for use with finite differencing numerical techniques is developed to increase this nodal efficiency over traditional uniform meshes. The adaptive algorithm (Section 2.3) creates a non-uniform mesh that places a higher density of grid points in regions determined by problem specific refinement conditions. The use of dynamic tree data structures (Section 2.2) contains information about the nodes, their inter-connectivity and the computed field values of the model at those nodes. For example, for the pure alloy phase-field model discussed in section 1.4.1 a simple refinement condition can be set using a linear combination in the gradients in both the phase and the dimensionless temperature as in equation 2.2,

$$|\nabla\phi| + \gamma|\nabla U| > Threshold \quad (2.2)$$

that will result in high densities of nodes at the interface and in regions where the dimensionless temperature is steep, as shown in figure 2.1.

2.2 Finite Difference Adaptive Grid Structure

The finite difference adaptive grid data structure handles two distinct processes, the mesh quad tree adapter and the linear array finite differencing solver, the details of which are graphically represented in Figure 2.2. The linear array finite differencing solver is the user side interface on which the model is implemented. It contains three arrays of node points (grid points), field value nodes, ghost nodes and boundary nodes. These are all described below in section 2.2.2. The mesh quad tree adapter includes the additional data structures of the element, described in section 2.2.1, and the quad-tree in section 2.2.3. Both the adapter and the solver each access the node structure via pointers in either the elements or the solver arrays. The grid structure also contains all global information about the domain area, such as initial

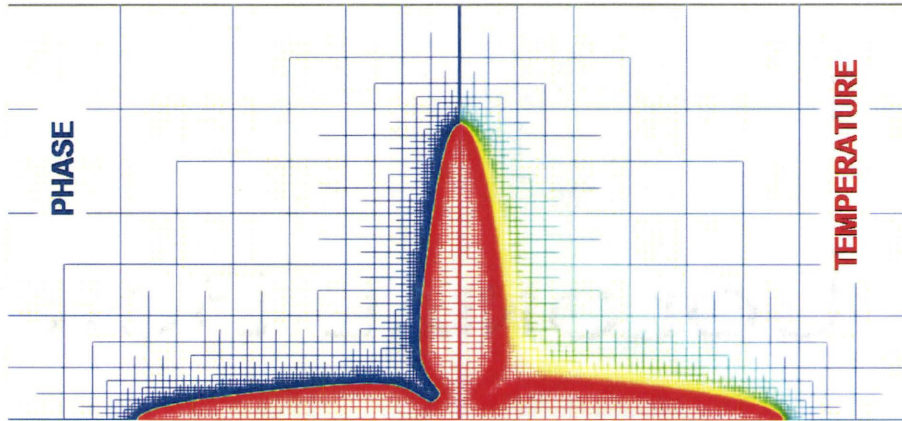


Figure 2.1: *Adaptively grown dendrite of a pure metal illustrating the phase and thermal fields. High resolution is adapted at the interface where needed and unresolved in other regions.*

undercooling U for the pure alloy, supersaturation for an alloy, material parameters, etc. Each tree structure describes a square domain area and the tree pointer array allows many trees to be interconnected to simulate non-square domain areas. In addition to this functionality a later implementation will allow individual or clumps of trees to be spread over multiple processors for parallel computation. This feature and a 3D version of the code will not be discussed further in this thesis.

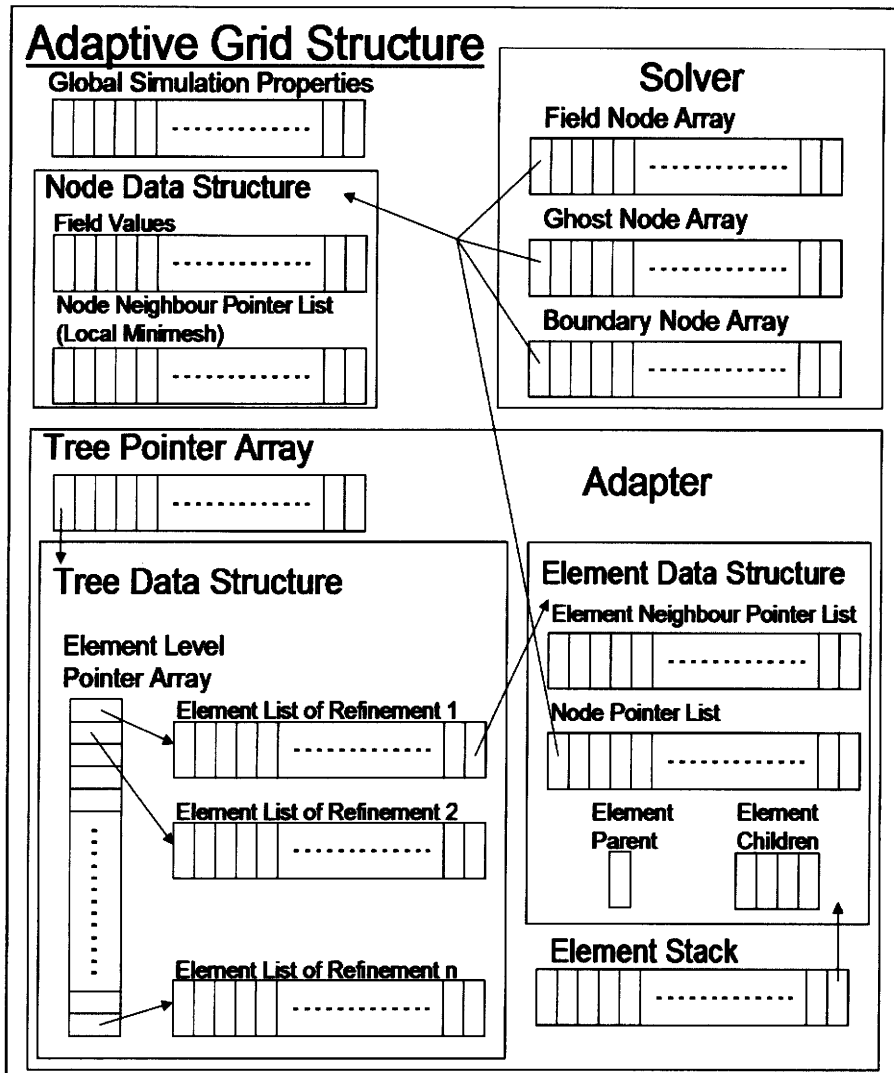


Figure 2.2: A schematic diagram of the adaptive grid data structure. The arrows represent connectivity pointers.

2.2.1 Element Structure

The element structure can be visualized as a branching point in the mesh. The structure of the element contains pointers to its 4 children, its parent element, to 9 nodes and to its 8 immediate element neighbours, see Figure 2.3. If the element has no children then this element is termed a leaf and its ghost nodes can potentially be active. With reference to Figure 2.3, ghost nodes can only exist at the white nodes and the black nodes are strictly field nodes. Field nodes become termed

boundary nodes when they are against a domain boundary. These are discussed further below. The relationship between the nodes and the element neighbours is schematically shown in figure 2.3. During the course of the adaption process each element follows three rules:

ELEMENT RULE 1: All adjacent elements can vary by only one level in refinement

ELEMENT RULE 2: All elements contain 9 nodes, field, boundary or ghost

ELEMENT RULE 3: Element neighbour pointers only point to elements of the same level

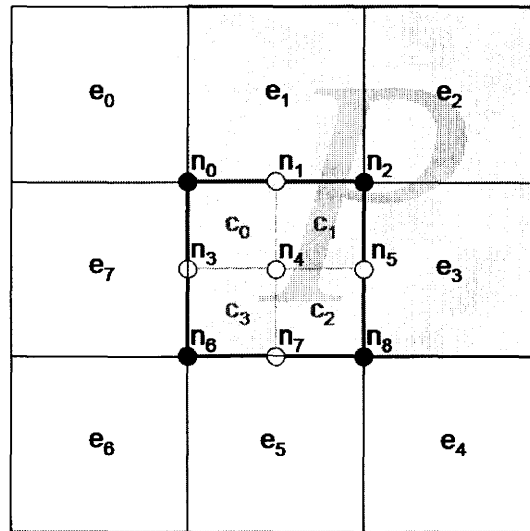


Figure 2.3: Schematic of the element data structure for the element outlined in bold. The element has 8 immediate neighbours of the same level, $e_0 - e_7$, 9 nodes $n_0 - n_8$, 4 children element pointers $c_0 - c_3$ and a link to its parent element P denoted by the grey region. Black nodes are field nodes and white nodes may be either ghost or field nodes.

Element Rule 1 is the core to the adaptive process providing both stability to the solutions of partial differential equations on the non-uniform mesh and allowing for a systematic method of providing uniform mini-meshes at each field node. Rule 3 states that all of these pointers must point to neighbours on the same level (even if they don't exist). This is schematically shown in the Figure 2.3 where each element neighbour ($e_0 - e_7$) is identical in size as the current element. In the course of adaption there may however be no element neighbour of the current element in a particular direction (white elements in Figure 2.3). In that case the pointer points to nothing at all. Rule 1 however requires that the element's parent must have an existing neighbour in that location.

2.2.2 Node Structure

The node structure is the lowest level of the finite difference adaptive process. This structure contains the field values, such as ϕ and U from the model in section 1.4.1, which is used by the solver to update the solutions and through which the adaptive algorithm determines whether further refinement is required. The node structure maintains a local mini-mesh around each node by containing pointers to its local neighbour nodes. This is done by following these three rules during the course of adaption:

NODE RULE 1: Node neighbours are all the same level of refinement

NODE RULE 2: Nodes are at the center of a uniform mini-mesh

NODE RULE 3: A node takes the resolution (dx) of the most resolved element attached to it

There are three types of nodes, a field node, a ghost node and a boundary node. All nodes have no knowledge of whether they are a ghost, a field or a boundary node. It is the adaptive grid that determines this by storing them in the appropriate solver array after the adaption process.

A boundary node is a node which lies on a user defined boundary at which special functions are applied to simulate the appropriate physical boundary conditions. For example, such conditions could be zero flux boundaries or a boundary in which heat and/or additional material is added. The adaptive process also has the provision for not including boundary nodes, in this case the adaptive grid is structured with periodic boundary conditions on a toroid.

A field node is a node that exist at the corner of square elements, which form the bulk of the simulation domain. In figure 2.3 n_0, n_2, n_6, n_8 are always field nodes (except for the case of user defined boundary nodes). The nodes in the center of an edge, n_1, n_3, n_5, n_7 may be field nodes if they are corner nodes to any of the four elements to which they can be attached. The field values at these nodes are determined by the partial differential equations of the model.

A ghost node is a node that is required to exist to provide a uniform mini-mesh for a field node. Edge nodes n_1, n_3, n_5, n_7 are ghost nodes if they are not also corners of other elements (i.e. field nodes). Center nodes n_4 are always ghost nodes. The field values at these nodes are not determined by the model but are instead determined by a user input function which interpolates their value from neighbouring field nodes. For the purposes of the research presented in this thesis, all interpolations are done linearly. For example for the edge node n_1 ,

$$X_{n_1} = \frac{1}{2}(X_{n_0} + X_{n_2}) \quad (2.3)$$

and the ghost at the center of the element is interpolated by

$$X_{n_4} = \frac{1}{4}(X_{n_0} + X_{n_2} + X_{n_6} + X_{n_8}) \quad (2.4)$$

where X is the field value to be interpolated.

2.2.3 Quad Tree Structure

The quad-tree data structure presented here is similar to the tree structure developed by Provatas et al [68]. The difference between their data structure and the one presented here lies on the focus placed on the node data structure for finite differencing as opposed to the element centered focus used with finite element solvers in their 1999 paper. A single quad-tree data structure is defined on a square domain of the study area. Several trees can be strung together to form rectangular study domains or spread over several computer processors for memory and speed increases.

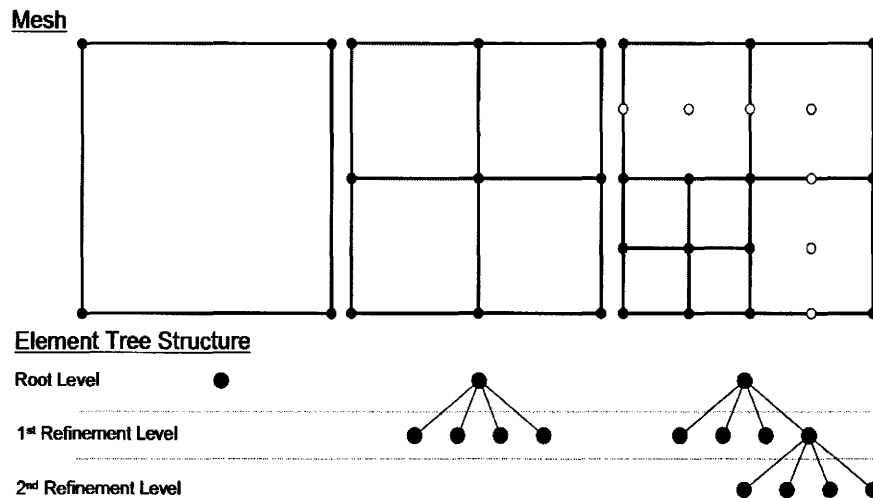


Figure 2.4: Schematic diagram of a quad-tree data structure used in adaptive meshing. An element splits and creates 'children' beneath it in the tree structure. Active 'Field' nodes are represented by black nodes and active 'Ghost' nodes are represented by white nodes.

The adaptive tree (or quad-tree) can be pictured as the hanging branch of a tree, with a root element at the top, as illustrated in Figure 2.4. Every time an element splits it spawns four new children to the resolution level beneath it, much as the branch would split to smaller and smaller branches. Any element that has no children is considered to be a leaf. These leaves represent the regions that have resolved to the needed resolution and therefore the nodes connected with these elements will be passed to the solver algorithm for the model update. The element leaves are stored in the element pointer arrays by level of resolution. These arrays are used to determine the element refinement and unrefinement process, discussed below in section 2.3.

2.3 Adaptive Mesh Refinement Algorithm

The adaptive mesh refinement technique is broken down into two distinct objects.

1. The mesh quad tree adapter algorithms (Section 2.3.1).
2. The linear array finite differencing solver algorithm (Section 2.3.2).

These two independent object structures pass the node structures back and forth between them. The layout of the basic relationship between these two algorithms

Algorithm 1 Basics of Control

```
Initialize program variables and parameters
Resolve mesh according to initial parameters
Apply initial field values
for time=1 to End Of Simulation do
  if Readapt Criteria met then
    Mesh Quad Tree Adapter
  end if
  Linear Array Finite Difference Solver
end for
```

is given in Algorithm 1. The initial simulation parameters are set and the mesh is initially resolved to the initial geometry of the study domain, ie. a small circular particle in a melt or a seed particle in a matrix. Once the mesh has been resolved to this domain, the initial field parameters are applied to the mesh and the simulation begins. A regridting criterion is defined, typically re-gridding every M time steps as the simulation progresses. At every time step the solver is called to update the field values on the nodes. When the readapt criteria is met, the node structures are passed to the Mesh Quad Tree Adapter to reconstruct the mesh.

2.3.1 Mesh Quad Tree Adapter Algorithms

The Mesh Quad Tree Adapter Algorithm takes as input all of the nodes from the Linear Array Finite Differencing Solver and empties the ghost node array. The algorithm (the flow of which is shown in Algorithm 2) first inspects every element for the criteria of unsplitting and then checks every element for the criteria of splitting. It continues this process until no elements have been split or unsplit. To help maintain the rules in sections 2.2.1 and 2.2.2 every leaf element is checked only once for splitting and unsplitting by cycling through the element level pointer array. Once each element in these lists have been checked once the lists may be cycled through again to check for further refinement.

The splitting algorithm is the dominant routine in the adaption process, ie. splitting takes priority over unsplitting. Each element is examined sequentially, starting

Algorithm 2 Mesh Quad Tree Adapter Algorithm

```
Delete the Ghost Pointer List
while Some elements have split or unsplit do
    Check All elements for unsplitting criteria
    Check All elements for splitting criteria
end while
Update Node Neighbours Lists
Build Ghost Node List
Set Ghost Averaging Information
```

at the 2nd highest of resolved elements in the element level pointer array, the highest resolution already having been split as far as allowed. Each element is checked for the defined splitting criteria. If the element must be split, it is pushed onto a stack data structure and each of its neighbours are then checked against ELEMENT RULE 1. If splitting will violate this rule, neighbours are pushed onto the stack for splitting and their neighbours are checked against element rule 1. This process occurs recursively down the levels of refinement until no adjacent elements violate element rule 1. Once the order of splitting is determined by the stack, the element

Algorithm 3 Splitting Algorithm

```
for ElementLevelArray=maxLevel-1 to 0 do
    while Level is not empty do
        if Element Splitting criteria is met then
            Push Element onto stack
            while Stack is not empty do
                if Top of Stack's neighbours need splitting then
                    Push Needed Neighbours onto stack
                else
                    Pop the Element from the Stack
                    Create 4 new children elements
                    Push children onto ElementLevelArray +1
                    Add New Nodes to the Node List
                    Remove former Ghosts from Ghost List
                end if
            end while
        end if
    end while
end for
```

on the top of the stack is popped and the element is split. New elements are created as the element's children, pointers to the element's neighbours are updated, new nodes are generated, ghost nodes are converted to field nodes and the node

neighbours are updated. The process of splitting is illustrated in algorithm 3

Unsplitting is a procedure for determining whether an element will have its four children elements removed, making the procedure to determine whether an element is unsplit much simpler. ELEMENT RULE 1 must still be maintained. The unsplitting algorithm begins at the bottom of the element level pointer array (i.e. at the lowest level of refinement) and the elements are sequentially checked to see if its parent element requires splitting. If the parent element does not require splitting then the parent is unsplit IF the neighbours allow it (ELEMENT RULE 1). There is no recursive unsplitting of elements. The elements neighbours and node neighbours are updated. The flow of the unsplitting algorithm is shown in algorithm 4.

Algorithm 4 UnSplitting Algorithm

```
for ElementLevelArray=maxLevel-1 to 0 do
  while Level is not empty do
    if Element Splitting criteria is NOT met then
      if Element's Parent's Splitting criteria is NOT met then
        if Parent's Children Have NO Children then
          if Parent's Neighbour's are Same level or One level Lower then
            ADD Parent to ElementLevel+1
            REMOVE Parent's Children from ElementLevel
            REMOVE Unneeded nodes from node list
            REMOVE Ghosts from Ghost list
            Center Node Becomes a Ghost
            Edge Nodes Become Ghosts depending on neighbour levels
            DELETE Children
          end if
        end if
      end if
    end if
  end while
end for
```

Once there are no elements that require splitting or unsplitting the field, boundary and ghost node lists are all updated and passed back to the solver. This and the method of solution of the phase field equations on the node structure is discussed next.

2.3.2 Simple Adaptive Mesh Modeling Solver Routine

Typically, any algorithm you can apply to a uniform mesh can also be applied in the solver algorithm. The solver algorithm can be very simple, with the addition of one

additional step over a uniform meshing algorithm. In the adaptive solver routine, the ghost nodes must be interpolated before the field node values are used. The simplest form for the solver algorithm is outlined in algorithm 5.

Algorithm 5 Linear Array Finite Difference Solver Algorithm

Update Boundary Conditions
 Update Ghost Nodes
 Update Field Nodes

The ghost nodes are updated by the interpolations described in equations 2.3 and 2.4. Each field node is located at the center of its own local mini-mesh as illustrated in Figure 2.5. The field nodes are calculated by standard finite difference templates (these templates are described in Appendix A.1) on the mini-mesh without the knowledge of whether the field values of its neighbours are from ghost nodes or other field nodes.

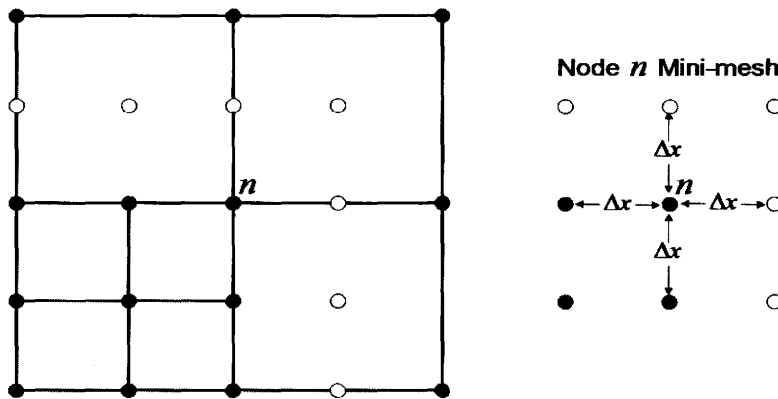


Figure 2.5: *Global (left) and Local (right) meshes around the node n. The node n sees only a local uniform minimesh.*

2.4 Finite Difference Adaption Efficiency

The adaptive mesh approach provides the advantage of dramatically reducing both the computer memory requirements and reducing the overall time for a given simulation to be completed, allowing for larger domain and precipitate sizes. This is accomplished by reducing the total number of grid points that must be stored in memory and therefore the total number of grid points that must be evaluated at each time step. Traditionally adaptive meshes have been employed using the finite element method. In this thesis, the node structure is specifically designed (e.g.

ghost nodes in Figures 2.4 and 2.5) for the use of finite differencing to approximate derivatives.

The remainder of this chapter proceeds as follows. The total node count produced by an adaptive mesh is characterized below, followed by a section over-viewing the efficiency of finite difference techniques over finite elements. Three examples are then used to illustrate the portability and advantage of the finite difference adaptive mesh in the application of a myriad of problems in microstructure formation.

2.4.1 The Reduction of the Total Node Count

The nodal count efficiency is considered for a circular precipitate of the pure material model briefly introduced in section 1.4.1. The node count at the refinement level

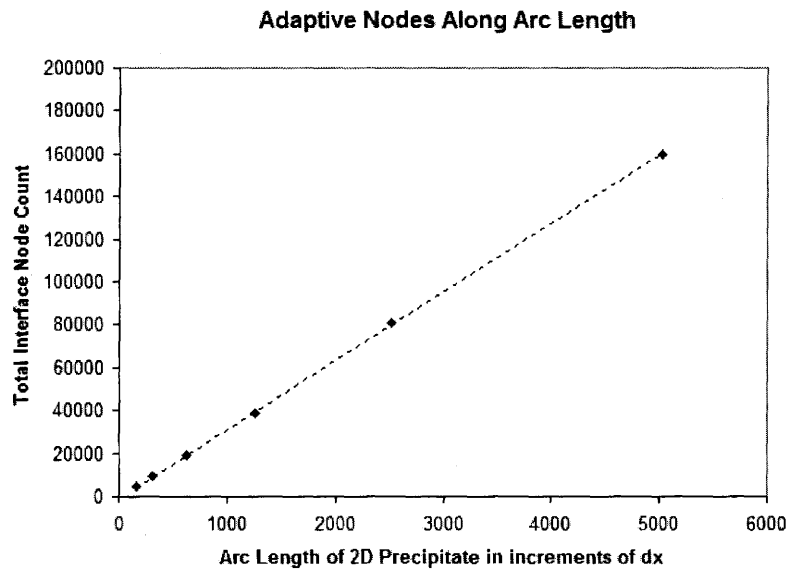


Figure 2.6: Total Node Count of nodes at the interface grid refinement level as a function of the total arc length of the precipitate. The relationship is linear with the total arc length.

along the arc-length of the precipitate interface is plotted in Figure 2.6 showing a linear relationship to the total arc-length of the precipitate, ie $N_{arc} = A_a \cdot L_{arc}$, where L_{arc} is the total arc length of the precipitate and A_a is a constant representing the adapted thickness of the interface. The remainder of the total node count in the bulk of the domain, Figure 2.7, shows a logarithmic relationship as $N_{bulk} = A_b \log_2(L_{system})$ where L_{system} is the total system size along one edge and A_b is a constant related to the geometry of the elements. Only when the precipitate

radius is of the same order of magnitude as the total system size, ie $\frac{L}{2R} \approx 1$ does the logarithmic behaviour break down resulting in a decrease of the total bulk nodes.

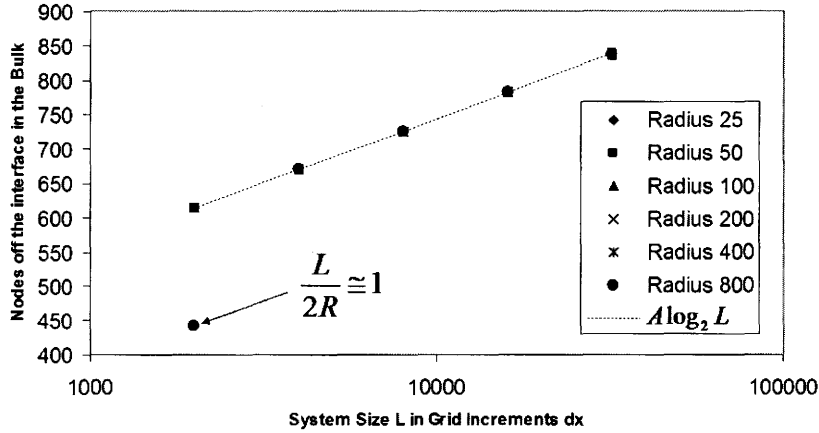


Figure 2.7: Total Node Count in the bulk of the domain for a series of circular precipitates in increasing domain sizes. The total count strictly follows a logarithmic behaviour except when the precipitate size approaches that of the domain size.

The total node count is constructed by the addition of these two contributions:

$$\begin{aligned}
 N_{total} &= N_{arc} + N_{bulk} \\
 &= A_a \cdot L_{arc} + A_b \log_2(L_{system}) \\
 &= O(L_{arc}) + O(\log(L_{system}))
 \end{aligned} \tag{2.5}$$

To characterize the total node count the magnitudes of each of $O(L_{arc})$ and $O(\log(L_{system}))$ must each be considered. As illustrated in Figures 2.6 and 2.7 the total count of the bulk nodes is much less than the interface nodes for the chosen particle and domain sizes. The condition of Node count dominance is such that $N_{arc} = N_{bulk}$. If a precipitate is grown to a size of $100nm$ with a grid spacing of $0.5nm$, for the above condition to occur the total domain size (ie. L_{system}) must be of the same order of magnitude as the size of the universe. Therefore it can be assumed that the total node count is,

$$N_{total} = O(L_{arc}) \tag{2.6}$$

2.4.2 The Efficiency of Finite Differencing Techniques over the Finite Element Method

The finite element technique has many advantages, such as complicated element structure and domain boundary shapes, however it also has some computational disadvantages. When considering simple domain geometries, such as rectangular or periodic domain boundaries, there are two primary reasons for using finite differencing in adaptive mesh refinement over a finite element formalism:

Node Calculation Rate vs Simulation Time

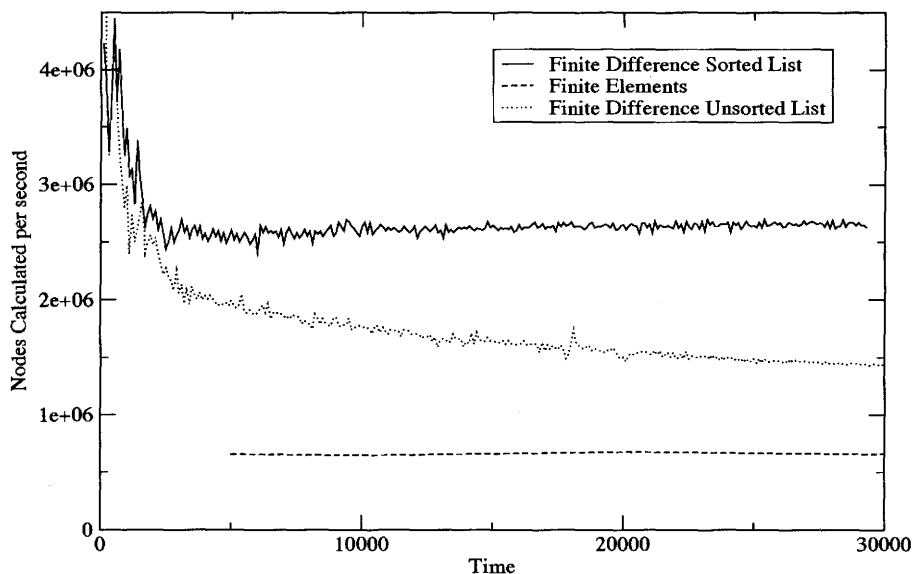


Figure 2.8: Time comparison of the finite difference method and the finite element method. The finite difference method is found to be at least five times faster than the finite element method on a per node basis. This plot also shows the computational importance of maintaining an ordered list in computer memory.

1. It provides a significant increase in computational efficiency over finite element codes. This can be seen in figure 2.8 where an ordered array of adaptive finite differencing nodes (Figure 2.8 - Finite Difference Sorted List) has an increase in computational speed of approximately 5 times over an adaptive finite element method (FEM). Depending on the problem solved and the finite element method used, this can be increased to 30 times or more due to either matrix inversion in the finite element process or local matrix calculations performed in each element, which carry a high overhead per node.
2. The finite difference method is much simpler to code numerically and therefore a more robust and portable meshing algorithm and data structure can be

”served up” for others to use in implementing their own model(s). The finite difference method also allows the approximation of higher order derivatives without a significant loss in speed, while finite element codes must use higher order elements resulting in significant increases of matrix manipulations and solution time.

2.4.3 Application of the Finite Difference Adaptive Mesh to Phase-field Simulations of Velocity Selection in Rapidly Solidified Binary Alloys [36]

This section summarizes the results of a recent paper in which simulations of an alloy phase field model solved with the adaptive mesh technique described above were performed to examine dendrite tip velocity and solute partitioning during rapid solidification of an isothermally cooled alloy. To run simulations with available memory and in realistic times the adaptive meshing was very important [36].

The phase field model used to simulate isothermal solidification of a 2-D binary alloy is given by

$$\begin{aligned} \frac{1}{M_1} \frac{\partial \phi}{\partial t} = & \vec{\nabla} \cdot (W^2(\theta) \vec{\nabla} \phi) - \frac{\partial}{\partial x} \left(W(\theta) \frac{dW(\theta)}{d\theta} \frac{\partial \phi}{\partial y} \right) \\ & + \frac{\partial}{\partial y} \left(W(\theta) \frac{dW(\theta)}{d\theta} \frac{\partial \phi}{\partial x} \right) - \frac{\partial f(\phi, C, T)}{\partial \phi} \end{aligned} \quad (2.7)$$

$$\frac{\partial C}{\partial t} = \vec{\nabla} \cdot \left(M_2 C(1 - C) \vec{\nabla} \left(\frac{\partial f(\phi, C, T)}{\partial C} \right) \right) \quad (2.8)$$

The field $C(x, t)$ is the dimensionless (molar fraction) alloy concentration field, while T denotes the constant temperature and ϕ is the usual phase field or order parameter. The parameter M_1 is related to the interface kinetic coefficient while M_2 is related to the solute diffusivity D . The function $f(\phi, C, T)$ is the bulk free energy of the a binary alloy. The first three gradient terms on the right hand side of Equation 2.7 arise due to the fact that the surface energy is assumed to be anisotropic, as discussed in the introduction in section 1.4.1. The model essentially represents a coupling of the dissipative equation for the evolution of the order parameter with Fick’s law of diffusion. The details of this model can be found in the reference [64, 36].

The model is used to study time-dependent simulations of two-dimensional isothermal Ni-Cu dendrites simulated on the above mentioned adaptive mesh refinement technique. The use of the adaptive mesh allowed for the simulation of system sizes that would have required $256 \cdot 10^6$ nodes at all times (approximately 5-10 GBytes of computer memory), whereas at early times the AMR algorithm

contains only a few thousand nodes (≈ 1 MByte of computer memory with the adaptive mesh memory overhead). At late times the efficiency of the algorithm is found to scale with the available microstructure interface, not the system area (2-D) or volume (3-D).

The dendrite tip velocity selection is examined and found to exhibit a transition between two markedly different regimes as the undercooling is increased. At low undercooling, the dendrite tip growth rate is consistent with the kinetics of the classical Stefan problem, where the interface is assumed to be in local equilibrium. At high undercooling, the growth velocity selected approaches a linear dependence on the melt undercooling, consistent with the continuous growth kinetics of Aziz et al. and with the one-dimensional steady-state phase-field asymptotic analysis of Ahmad et al. [64]. Moreover, it was found that the solute partitioning coefficient at the solid-liquid interface approaches unity as the velocity increases such the diffusion length of impurities approaches the scale of the solid-liquid interface width. The simulations are also consistent with other previously observed behaviors of dendritic growth as the undercooling is increased. This includes the transition of dendritic morphology to absolute stability and non-equilibrium solute partitioning. The results of this study show that phase-field models of solidification, which inherently contain a nonzero interface width, can be used to study the dynamics of complex solidification phenomena involving both equilibrium and non-equilibrium interface growth kinetics.

2.4.4 Application of the Finite Difference Adaptive Mesh to Polycrystalline Pattern Formation Using a Coarse-grained Approximation of the Phase-Field Crystal Model[7]

The second application of the new adaptive mesh refinement algorithm is to a new class of phase field models known as "phase field crystal" models [51, 50, 66]. These models can be represented by one or more amplitude equations, the solution(s) of which can be combined to model phase transformations that incorporate atomic-scale elastic and plastic effects. These types of equations are not the topic of this thesis. They represent the future of phase field modeling, particularly for problems at the nano-micron scale which involve atomic scale elasto-plasticity. These types of equations are, however, a type of phase field model that poses a problem to traditional FEM approaches because they contain higher order derivatives (up to order 12), which leads to large overhead per node using FEM. A finite difference adaptive meshing algorithm allows the calculation of higher order derivatives with little extra work. The new AMR code developed in this work has been implemented to increase the overall efficiency of these models. The phase field crystal model and the amplitude equations are overviewed here briefly. Further details can be found in reference [7].

The phase field crystal (PFC) methodology constructs the equilibrium free en-

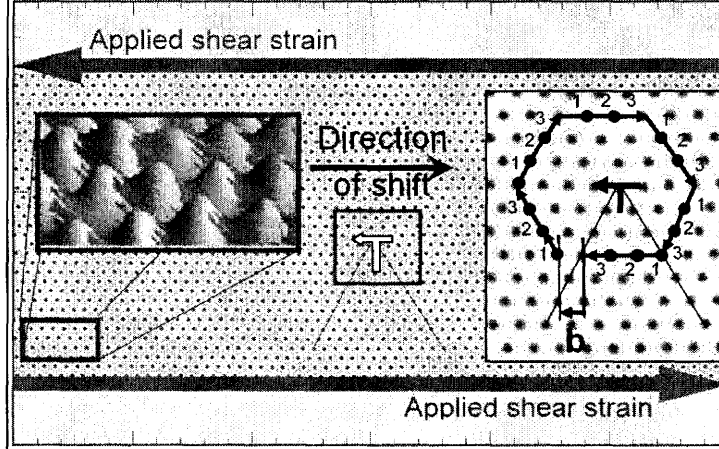


Figure 2.9: PFC simulation of an applied shear stress, illustrating the mean positions of atoms in a pure material and a dislocation.[66]

ergy such as to produce periodic atomic density states, rather than ones uniform in space. The conserved dynamics of the PFC model then naturally reproduce many of the nonequilibrium dynamics arising in real polycrystalline materials, thus the model will naturally include such properties as the elastic energy and surface energy anisotropic properties of the material. The peaks in the periodic density states actually represent the mean position of the atoms over billions of atomic vibration. This is shown in Figure 2.9, where Stefanovic [66] studied the effects of applied shear stress on the dislocation motion through a material.

In the PFC model of a pure material, the evolution of the density ρ is given by

$$\frac{\partial \rho}{\partial t} = \Gamma \nabla^2 \left(\frac{\delta G}{\delta \rho} \right) \quad (2.9)$$

where G is the free energy functional, which can be written as $G = \int d\vec{r} [f(\rho, \nabla^2 \rho, \dots)]$, f is the local free energy density and Γ is a constant. The density ρ can be rewritten in a dimensionless form $\Psi \propto \rho$, determined by the form of the energy f and the material properties such as the Young's modulus and the lattice spacing [51, 50]. This dimensionless spatial density can be approximated in terms of complex amplitudes A_j as

$$\Psi \approx \sum_{j=1}^3 A_j e^{ik_j \cdot x} + \sum_{j=1}^3 A_j^* e^{-ik_j \cdot x} + \bar{\Psi} \quad (2.10)$$

where $\bar{\Psi}$ is the mean density. While the field Ψ varies on atomic dimensions, the amplitudes A_j vary over longer length scales and are thus amenable to adaptive

mesh refinement¹. The idea behind this work was that the original phase field crystal equation (Equation 2.9) is formulated in terms of equations for the A_j , which are then solved for adaptively. The complete solution is then reconstructed by substituting the A_j back into Equation 2.10.

The complex amplitude equations for the A_j are given as

$$\frac{\partial A_j}{\partial t} = \tilde{\mathcal{L}}_j A_j - 3A_j |A_j|^2 - 6A_j \sum_{k:k \neq j} |A_k|^2 - 6\bar{\psi} \prod_{k:k \neq j} A_k^* \quad (2.11)$$

where $j, k \in [1, 3]$ and

$$\tilde{\mathcal{L}}_j = [1 - \nabla^2 - 2i\mathbf{k}_j \cdot \nabla] \left[-r - 3\bar{\psi}^2 - \{\nabla^2 + 2i\mathbf{k}_j \cdot \nabla\}^2 \right] \quad (2.12)$$

The superscript “*” denotes the complex conjugation, r (≤ 0) and $\bar{\psi}$ (≥ 0) are model parameters that control the bifurcation from a uniform liquid phase to a crystalline phase with hexagonal symmetry. Thus r is proportional to the temperature quench from a critical temperature T_c , whereas $\bar{\psi}$ can be viewed as a mean density.

Away from a topological defect, grain boundary or vacancy, the complex amplitude equations for A_j can be further reduced to a set of real phases (Ψ_j) and amplitudes (Φ_j). These vary over long lengths scales compared to the atomic scale, and can be solved adaptively. The equations for these variables are give by,

$$\begin{aligned} \frac{\partial \Psi_j}{\partial t} = & (r + 3\bar{\psi}^2) [-\Psi_j + \mathcal{C}^{\Re}(\Psi_j, \Phi_j)] \\ & - 3\Psi_j \left(\Psi_j^2 + 2 \sum_{k \neq j} \Psi_k^2 \right) - 6 \frac{\bar{\psi}}{\Psi_j} \left(\prod_k \Psi_k \right) \cos \left(\sum_k \Phi_k \right) \end{aligned} \quad (2.13)$$

$$\frac{\partial \Phi_j}{\partial t} = \frac{(r + 3\bar{\psi}^2) \mathcal{C}^{\Im}(\Psi_j, \Phi_j)}{\Psi_j} + 6 \frac{\bar{\psi}}{\Psi_j^2} \left(\prod_k \Psi_k \right) \sin \left(\sum_k \Phi_k \right), \quad (2.14)$$

where the operators \mathcal{C}^{\Re} and \mathcal{C}^{\Im} contain only first and second order derivatives in Ψ_j and Φ_j .

The phase and amplitude formalism of Equations 2.13 and 2.14 has neglected higher order derivatives of Ψ_j and Φ_j , limiting these equations to only second order derivatives. However these equations are only solved in the crystal interior, away from the interface. The complex amplitude formalism (Equation 2.11), which is valid near topological defects, requires 6th order derivatives and is implemented with ease on a finite difference adaptive mesh. Figure 2.10 shows the average of the three complex amplitudes A_j of Equation 2.11 (re-constructed from Ψ_j and Φ_j) for the case of polycrystalline solidification.

¹strictly speaking it is these amplitudes that are the authentic “phase fields”

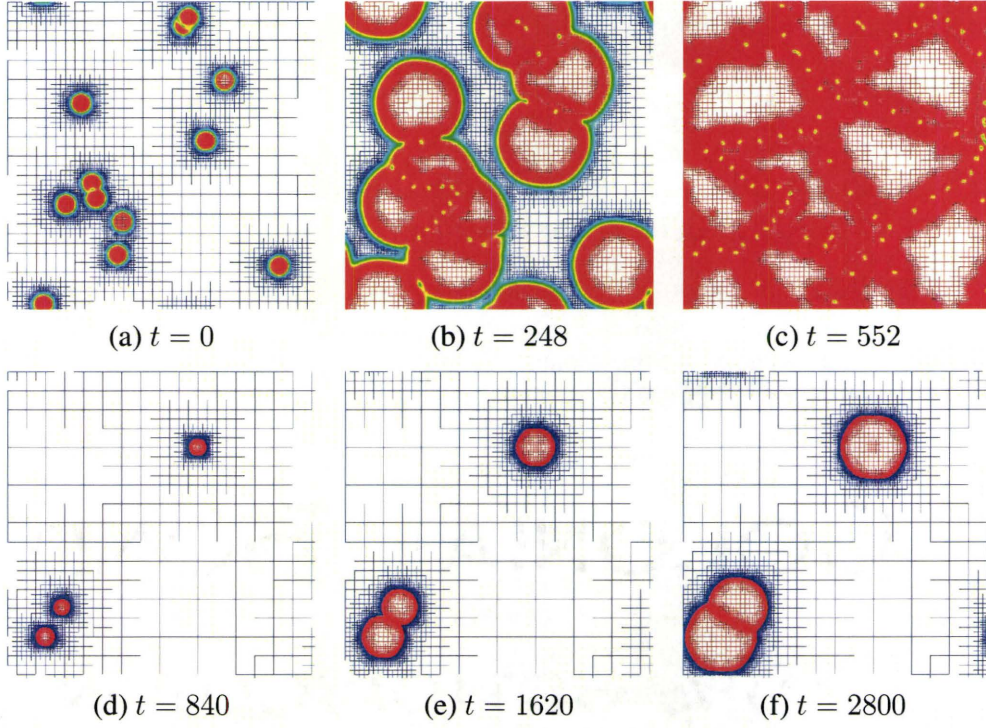


Figure 2.10: The top (a,b,c) is a region densely populated by precipitates. The system size is 256π , or roughly 45 nm . The bottom (d,e,f) is a region sparsely populated with precipitates, the region size being 4096π or about $0.722 \mu\text{m}$. [7] The highly dense regions of red are grain boundaries of different precipitates, i.e. variations in the amplitudes A_j . The yellow dots seen in the grain boundaries are dislocations that occur in the boundary.

In figure 2.10 a,b and c, the simulation speed up factor was of the order of $S = 10$ since the grains are very densely packed and the volume to surface ratio is small. Whereas the much larger simulation sizes, where grains can grow to the order of μm (figure 2.10 d,e and f) results in simulation speedups of $S = 1000$ or more.

It can be shown [7] that the new adaptive mesh approach leads to an acceleration by three orders of magnitude in model calculations of polycrystalline grain growth in two dimensions, where the speed up factor was defined as,

$$S = \frac{N_{uni}}{N_{Tot}} \frac{\Delta t_{uni}}{\Delta t_{hyb}} \frac{1}{6} \xi \quad (2.15)$$

where N_{uni} is the number of grid points required to solve the PFC equation on a uniform mesh, and N_{Tot} is the number of grid points required to solve the hybrid

implementation of the modified PFC model, Δt are the respective time steps of the implementations and ξ is the overhead of the AMR algorithm, which is found to be about $\xi \approx 0.97$.

2.4.5 Application of the Finite Difference Adaptive Mesh to the Solution of Static Elasticity by Gauss-Seidel Iteration

The final application of the adaptive mesh refinement technique is the efficient solution of the phase field model coupled to elasticity, which will be the main focus of Chapters 4 and 5. As this model will be presented in detail later, only the results of the efficiency of the new adaptive mesh algorithm on this model will be presented in this section.

The displacement fields that satisfy equation 1.9 and that are coupled to the phase field model in chapters 4 and 5 are solved by Gauss-Seidel iteration. In brief this method incrementally improves the static strain fields by using an approximate solution at iteration j to give an improved solution estimate at step $j + 1$. When solutions stop changing, the method is said to be converged to the correct solution. The templates for updating these equations on a numerical mesh are presented in appendix A.3. Typically the solution time for a Gauss-Seidel iterative technique is of the order of $O(N^2)$, where N is the total number of grid points in the system [28]. On a uniform mesh this is simply an unmanageable way to solve strain fields (or any static fields) for every time step of the dynamic phase field equations. However, presented below are two new techniques developed in this thesis, which together are used to increase the computational efficiency with which the strain field can be calculated, with no changes required to the Gauss-Seidel algorithm. Through this method a numerical solution to equation 1.9 is achieved in a time of the order $O(A)$, where A is the number of grid points on the surface area (3-D simulation) or arc length (2-D simulation) of a precipitate. These techniques are as follows:

First, the Gauss-Seidel algorithm works most efficiently by using an accurate approximation to the solution field. At time t during the phase transformation process the displacement fields are approximated from the solution of the displacement field at time $t - dt$. The phase and composition fields each only vary by a small amount in each time step. If the solution at time $t - dt$ is converged, then using this as a guess for the displacement fields at time t results in a solution that is already very close to convergence. Therefore, only the initial time step (ie. around the initial seed) will require a convergence time of $O(N^2)$.

Secondly, the solution to equation 1.9 on the finite difference adaptive mesh is improved by the decrease in the total number of grid points and the far field propagation of the iterative correction to the displacement field is quickly solved by a coarse mesh. Section 2.4.1 shows that the total number grid points is linear with the total surface area (3-D simulation) or arc length (2-D simulation) of the precipitates. This alone changes the solution time for a uniform mesh from $O(L^4)$,

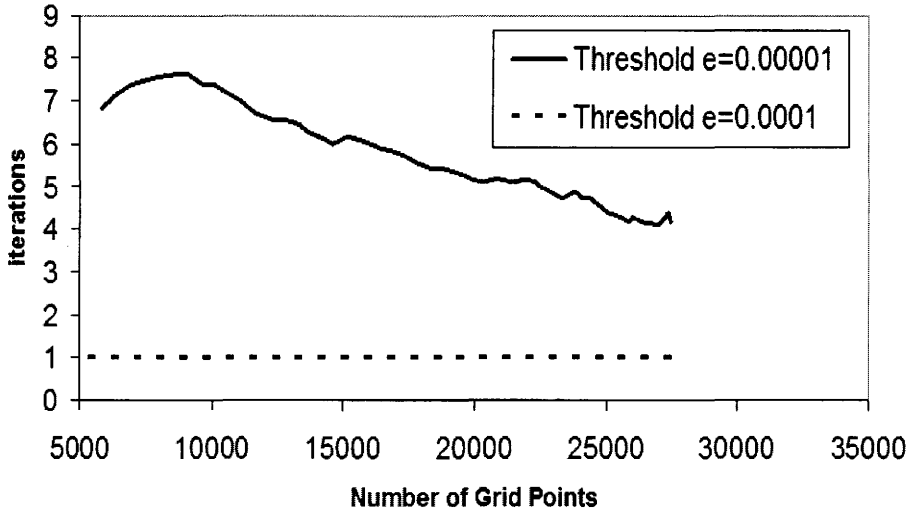


Figure 2.11: *Precipitates are grown in a parent phase and the displacement fields are converged to a threshold error of $e = 0.00001$ and $e = 0.0001$. Plotted is the number of convergence iterations required to attain the selected error vs the particle size represented by the total number of grid points. The total number of required iterations is found to approach a constant at every time step.*

where L is the number of grid points along the edge of the domain, to at worst $O(A^2)$. For a dendrite the size of the domain this results in a solution time of $O(L^2)$, a marked improvement over the uniform solution.

It is found that a combination of these two methods results in a convergence time of $O(A)$. This is illustrated by Figure 2.11 in conjunction with the total node count in Equation 2.6. Figure 2.11 shows that for two convergence criterion ($e = 0.0001$ and $e = 0.00001$ where ϵ is an error measure as described in Appendix A.3) the number of iterations required to converge the solution approaches a steady state constant as the total particle size increases (ie. the number of grid points increases). The number of convergence iterations required is therefore dependent only on the convergence criterion e , ie.

$$t_{steps} = F(e) \quad (2.16)$$

where t_{steps} is the number of convergence iterations and $F(e)$ is a function dependent only on the convergence criterion e and is independent of the number of grid points N . In combination with Equation 2.6 the total convergence time is thus found to be

$$t_{convergence} = N_{total} \cdot t_{steps} = O(A) \quad (2.17)$$

A dendrite grown to the domain boundary on an adaptive mesh has $O(L)$ grid

points by Equation 2.6. This technique shows that the convergence time of this dendrite will be $O(L)$, a marked improvement over a similar solution time of $O(L^4)$ for the same dendrite grown on a uniform mesh with no initial guess for the solution. Other techniques for rapid solutions to the displacement fields could also have been implemented. Two standard techniques are the Multi-grid technique and the fourier techniques developed by Khachatryan. Both of these techniques are typically applied to uniform meshes and would require a solution $O(L^2 \log(L))$. If these techniques are applied on an adaptive mesh the solution times would at best result in $O(L)$ time. Therefore the Gauss-Seidel methodology on an adaptive mesh is superior in its simplicity of application.

Chapter 3

Thin Interface Asymptotics for Quantitative Modeling of Phase Field Models for Alloys with Non-Linear Phase Boundaries.

This chapter develops mathematical modifications to a recently formulated phase field of an ideal, dilute binary model [8]. This contribution incorporates a new formalism for phase transformations that allows one to exploit a thin interface asymptotic analysis developed by previous authors [8, 49] to the study of *non-linear* phase diagrams [13].

A significant advantage afforded to the approach introduced by previous workers [8, 49] is the ability to choose the interpolation functions (such as Equation 1.18) for the entropy and internal energy in the free energy functional such that the steady state phase field and concentration equations decouple for all values of the interface width (W). This allows the surface energy in the phase field model to be set independently of concentration, a feature critical when making the phase field interface diffuse for computational convenience. Otherwise, a concentration-dependence to the surface energy would exist, detracting from the efficiency with which equivalent sharp-interface parameters can be calculated and subsequent computations carried out. An additional advantage of the approach of Karma and co-workers is the inclusion of an anti-trapping flux, a mathematical construct that enables the model to cancel the effects of spurious kinetics and solute trapping that arise when the model is run at an accelerated rate for numerical convenience. The construction of this anti-trapping flux in order to operate the model with diffuse interfaces was coined the "thin-interface" analysis. There are alternative phase field formulations that also decouple the phase and concentration equations [26, 33, 79]. However, a thin-interface asymptotic analysis for simulating these models in their corresponding sharp-interface limit is presently lacking. This implies that while these other for-

mulations can unambiguously set the surface energy into their model, they are not generally free of spurious interface kinetics and non-equilibrium solute trapping.

To date most quantitative phase field studies of single-phase solidification have been formulated strictly for dilute ideal alloys, characterized by *linear* coexistence curves. A notable exception is the two-phase solidification model of Ref. [71], which can be collapsed to a single-phase solidification model that can describe solidification in alloys with non-linear coexistence curves. A limitation of this model, however, is that it approximates the second derivative of the free energy of each phase to be equal. Because of this, the thin-interface limit of this model does not correctly capture any curvature corrections arising from the *unequal* second derivatives of the Gibb's free energy at equilibrium. Moreover, their work modeled solid-liquid coexistence at all temperatures by linear liquidus and solidus lines.

This Thesis developed an extension to the approach of Karma and co-workers which allows non-ideal alloy phase field models to be simulated in the limit of a diffuse interface (called a thin-interface limit). Section 3.1 first considers the sharp interface kinetic equations for non-linear phase equilibrium lines in the binary alloy phase diagram. In section 3.2 an approximation of the Gibbs Free Energy Functional is made by Taylor expansion about reference compositions. This Taylor expansion is fit to the general free energy of a binary alloy with *non-linear* coexistence curves is proposed in section 3.3. Section 3.4 shows results with an application to a non-ideal binary alloy undergoing both isothermal and non-isothermal solidification. Finally, the technique is applied to the practical problem of diffusion limited growth rates of α needles in β brass in section 3.5.

3.1 Sharp-Interface Kinetics of Binary Alloy Solidification

After generalizing the Gibbs-Thomson condition in the introduction of this thesis, equation 1.3, this boundary condition can be expressed as

$$c_{L,s} = c_{L,s}^{\text{eq}} - c_{L,s}^{\text{eq}}(1 - k(T)) \left[\frac{2\gamma T/L}{|m_{L,s}(T)|(1 - k(T))c_L^{\text{eq}}} \right] \kappa \quad (3.1)$$

where

$$|m_{L,s}(T)| = \frac{RT^2(1 - k(T))[\hat{G}''(c_{L,s}^{\text{eq}})c_{L,s}^{\text{eq}}]}{\nu L} \quad (3.2)$$

and where we have defined

$$k(T) = \frac{c_s^{\text{eq}}(T)}{c_L^{\text{eq}}(T)} \quad (3.3)$$

as the temperature dependent partition coefficient between solid and liquid phases, which is uniquely defined by the phase diagram of a particular alloy. Meanwhile,

$\hat{G}''(c_{L,s}^{\text{eq}})$ is the second derivative of the dimensionless molar Gibb's free energy evaluated at the equilibrium concentrations $c_{L,s}^{\text{eq}}$ (made dimensionless by redefining $\hat{G} \equiv G/RT$). L is the latent heat of fusion, $c_{L,s}(\vec{x}, t)$ is the concentration field, ν is the molar volume of the phases, T is the temperature, R is the natural gas constant, γ is the surface energy of the solid/liquid interface and κ is the local interface curvature.

Equation 3.1 shows that for two co-existing phases the relative change in concentration is in general different on each side of the interface. The work here is limited to the class of alloys that satisfies $G''(c_s^{\text{eq}})c_s^{\text{eq}} \approx G''(c_L^{\text{eq}})c_L^{\text{eq}}$, which implies that $m_L = m_s \equiv m(T)$, the slope of the liquidus curve at temperature T . This can be seen by following standard procedures [29] to derive the liquidus slope of a binary alloy, which is given by

$$\frac{dT}{dc_L^{\text{eq}}} = \frac{RT^2(1 - K(T)k(T))[\hat{G}''(c_L^{\text{eq}})c_L^{\text{eq}}]}{\nu L} \quad (3.4)$$

where $K(T)$ (*not* the partition coefficient) is defined by

$$K(T) = \frac{G''(c_s^{\text{eq}})c_s^{\text{eq}}}{G''(c_L^{\text{eq}})c_L^{\text{eq}}} \quad (3.5)$$

When $K \approx 1$, $dT/dc_L^{\text{eq}} \equiv m(T)$. The consequence is that the solutal capillary length (large square bracket in equation 3.1) is the same on both sides of the interface. This working approximation becomes exact in dilute ideal solutions, but can also be assumed reasonable for a wider class of alloys at low enough concentrations.

3.2 Approximating the Gibb's Free Energy Functional

The Gibb's free energy function for a binary alloy will be constructed with the phase labeled by the index i . This will be used to motivate the choice of the phenomenological free energy used in our phase field model in the next section. Rather than attempting to fit or approximate the Gibb's free energy of the phase over its entire concentration domain, the function is, instead, expanded to second order in a series around $c = c_i^{\text{eq}}$, which we will require to be accurate only in the neighborhood around the equilibrium concentration. This approach is reasonable since at low undercooling, kinetics and curvature effects typically only cause the concentrations at the interface to deviate by a small amount from their equilibrium values.

Proceeding in this manner, the expansion for the Gibb's free energy of phase i is written as

$$G_i = g_i(T) + a_i(T)(c - c_i^{\text{eq}}) + b_i(T)(c - c_i^{\text{eq}})^2 \dots \quad (3.6)$$

where

$$g_i(T) = f(T) - S_i(T)(T - T_m(T)) + \frac{RT}{\nu} (\ln c_i^{\text{eq}}(T) + \epsilon'_i(T) - 1) c_i^{\text{eq}}(T) \quad (3.7)$$

$$a_i(T) = \frac{RT}{\nu} (\ln c_i^{\text{eq}}(T) + \epsilon'_i(T)) \quad (3.8)$$

$$b_i(T) = \frac{RT}{2\nu c_i^{\text{eq}}(T)} \quad (3.9)$$

The coefficient S_i is the entropy of the phase, while $\epsilon'_i \equiv \epsilon_i \nu / RT$ where ϵ_i is a free parameter of the phase, which has units of energy density. The functions $f(T)$ and $T_m(T)$ are for, the moment, arbitrary functions of temperature that are to be determined.

The free parameters of G_i will next be constructed so that the free energy self-consistently reproduces some relevant thermodynamic properties of a general binary alloy phase. Beginning with the chemical interpotential defined by $\mu_i(T) = dG_i/dc|_{c_i^{\text{eq}}}$ and equating $\mu_s = \mu_L$ gives

$$k(T) \equiv \frac{c_s^{\text{eq}}}{c_L^{\text{eq}}} = \exp\left(-\frac{(\epsilon_s - \epsilon_L)\nu}{RT}\right) \quad (3.10)$$

which fixes the internal energy difference $\epsilon_s - \epsilon_L$ in terms of the partition coefficient at temperature T . Alternatively ϵ_i can be fixed in terms of the chemical potential and the equilibrium concentration of phase i , both obtainable from thermodynamic databases.

The function $f(T)$ is determined by evaluating $G_i(c)$ at c_i^{eq} , giving

$$f(T) = S_i(T - T_m) + G_i(c_i^{\text{eq}}) - \frac{RT}{\nu} (\ln c_i^{\text{eq}} + \epsilon'_i - 1) c_i^{\text{eq}} \quad (3.11)$$

Requiring that $f(T)$ be independent of phase ($i = s, L$) imposes the constraint

$$(T - T_m)(S_s - S_L) = \frac{RT}{\nu} (1 - k(T)) c_L^{\text{eq}}, \quad (3.12)$$

which allows the reference parameter $T_m(T)$ in equation 3.7 to be self-consistently determined. Specifically, $(S_s - S_L) = -L/T$, where L is the latent heat of fusion. (L is assumed to be independent of temperature, although making it depend on temperature would not change any of the arguments presented here). Equation 3.12 is therefore re-cast as an explicit condition on the parameter $T_m(T)$

$$T_m(T) = T + \left[\frac{RT^2(1 - k(T))}{\nu L} \right] c_L^{\text{eq}}(T) \quad (3.13)$$

The factor in the rectangular brackets of equation 3.13 (hereafter denoted $m_d(T)$) is precisely the instantaneous liquidus slope of the alloy represented by the free energy in equation 3.6 at temperature T . This can be seen by substituting equation 3.6 into the general expression of the liquidus slope in equation 3.4. In general equation 3.13 defines a linear “phase diagram” that passes through the coordinates at $(T, C_L^{eq}(T))$ of the actual alloy phase diagram, and whose intercept $T_m(T)$ is temperature dependent.

It is convenient to cast the free energy expansion in equation 3.6 in terms of a more tractable analytical form, which will be used to link the phase field free energy functional to other phase field formulations in the next section. This is done by noting that the form of $G_i(c)$ defined by equation 3.6 is precisely a second order Taylor series expansion of the function

$$G_i(c) = f(T) - S_i(T - T_m) + \frac{RT}{\nu} (c \ln c - c) + \epsilon_i c \quad (3.14)$$

about $c = c_i^{eq}$, where all parameters in equation 3.14 have the temperature dependence defined above. It should be emphasized that while equation 3.14 has the same *analytical form* used to model ideal solutions, its parameters are quite different. Indeed, through the effective temperature dependence of the parameters in equation 3.14 many relevant properties of a *general* binary alloy phase near $c = c_i^{eq}$ can be approximated to a reasonable accuracy .

3.3 A Phase Field Model for Solidification of Binary Alloys

At the heart of this phase field formulation is the free energy functional given by

$$G = |W_o \nabla \phi|^2 + f(T) - S(\phi)(T - T_m) + \frac{RT}{\nu} (c \ln c - c) + \epsilon(\phi)c \quad (3.15)$$

where ϕ is the usual order parameter that continuously interpolates between solid ($\phi = 1$) and liquid ($\phi = -1$). The parameters in each phase i are as defined in equation 3.14. The interpolation functions for the entropy $S(\phi)$ and internal energy $\epsilon(\phi)$ interpolate between their respective values in each phase (i.e. $S(\phi = \pm 1) \rightarrow S_{s,L}$ and $\epsilon(\phi = \pm 1) \rightarrow \epsilon_{s,L}$). Their form is chosen precisely as in Refs. [48, 8] in order to guarantee that the concentration and phase field equations of motion introduced below decouple in a steady state, even for large values of the interface width (W).

The free energy functional (Equation 3.15) is substituted into the standard dy-

namical equations of motion for the phase given as

$$\tau(\vec{n}) \frac{\partial \phi}{\partial t} = - \frac{\delta G(\nabla \phi, \phi, C)}{\delta \phi} \quad (3.16)$$

and for the solute field as

$$\frac{\partial C}{\partial t} = - \vec{\nabla} \cdot \vec{J} \quad (3.17)$$

where \vec{J} is the solute flux and τ is related to the kinetic attachment time [48, 8, 62]. Following the procedure in [8] gives the following dimensional phase-field equations of solidification for a binary alloy:

$$\begin{aligned} \tau(T) A(\hat{n})^2 \frac{\partial \phi}{\partial t} &= \hat{\nabla} \cdot [W(T)^2 A(\hat{n})^2 \hat{\nabla} \phi] \\ &\quad + \phi - \phi^3 - \lambda(T) (1 - \phi^2)^2 U \\ &\quad + \hat{\nabla} \cdot \left(|\hat{\nabla} \phi|^2 W(T)^2 A(\hat{n}) \frac{\partial A(\hat{n})}{\partial (\hat{\nabla} \phi)} \right), \\ \left(\frac{1 + k(T)}{2} - \frac{1 - k(T)}{2} \phi \right) \frac{\partial U}{\partial t} &= \hat{\nabla} \cdot \left(D(T) q(\phi) \hat{\nabla} U \right. \\ &\quad \left. + a_t [1 + (1 - k(T)) U] \frac{\partial \phi}{\partial t} \frac{\hat{\nabla} \phi}{|\hat{\nabla} \phi|} \right) \\ &\quad + \frac{1}{2} [1 + (1 - k(T)) U] \frac{\partial \phi}{\partial t}, \end{aligned} \quad (3.18)$$

where $D(T)$ is the liquid state diffusivity, U is the dimensionless supersaturation defined to be $U = (e^u - 1)/(1 - k(T))$, $a_t = \frac{1}{2\sqrt{2}}$ is the anti-trapping prefactor, $q(\phi) = \frac{1-\phi}{2}$ modulates the two sided diffusion (i.e. between solid ($\phi = 1$) and liquid ($\phi = -1$) and

$$u = \ln \left(\frac{2C/C_L^{\text{eq}}}{1 + k(T) - (1 - k(T))\phi} \right) \quad (3.19)$$

The function $A(\hat{n})$ provides four-fold anisotropy as in the pure model, equation 1.17, while $W(T)$, the interface width, and $\tau(T)$, interface kinetic attachment time, may in general be temperature dependent. Finally, the coupling coefficient, λ , becomes

$$\lambda(T) = \frac{15}{8} \frac{L\Delta T}{2HT_m(T)} \quad (3.20)$$

where $\Delta T = |m_d(T)|(1 - k(T))c_L^{\text{eq}}(T)$ represents the freezing range on the effective linear phase diagram defined by equation 3.13, H is the nucleation barrier

height and $T_m(T)$ is the intercept of the linear phase diagram of equation 3.13. Finally, noting that by using the same anti-trapping term defined in Refs. [48, 8] in the U -equation, we can eliminate all thin-interface correction terms appearing in the thin interface limit of equation 3.18.

The model equations, 3.18, are identical in form to that examined in Ref. [8]. This connection allows the use of the same parametric relationships between $\lambda(T)$, $W(T)$ and $\tau(T)$ defined in [8] to map model equations, 3.18, onto the sharp interface model in section 1.1.1. Specifically, the solutal capillary length is related to the phase field model parameters as

$$a_1 \frac{W(T)}{\lambda(T)} = d_o(T) \equiv \frac{\gamma}{\Delta T^*} \quad (3.21)$$

where $a_1 = 0.8839$ [48] and $\Delta T^* = |m(T)|(1 - k(T))c_L^{\text{eq}}(T)$ with $m(T) = m_s = m_L$ given by equation 3.2. It is interesting to note that $\lambda = \lambda(T)$ can be treated as an adjustable convergence parameter in phase field simulations of the model equations, 3.18 [48, 8]. As such, any capillary length via equation 3.21 can be modeled by a suitable choice of $W(T)$.

The interface kinetic coefficient is set to be zero in the phase field simulations (at least to second order accuracy in the ratio W/d_o [48, 8, 62]) by setting

$$\tau(T) = \frac{a_2 \lambda(T)}{D} W^2(T) \quad (3.22)$$

where $a_2 = 0.6267$ [48]. For a constant temperature the coupling constant $\lambda(T)$ may be chosen arbitrarily since its value does not affect the convergence of the dendritic tip velocity and radius, provided it is small enough [49, 48, 8]. However, once a value of λ has been set, W and τ can still depend on temperature according to equations 3.21 and 3.22.

This approach can also incorporate non-isothermal conditions. In the limit when the thermal diffusion coefficient is much larger than the solute diffusion coefficient in the liquid (typically $D_L/\alpha \sim 10^{-4}$), it is reasonable to model temperature as a frozen field that adjusts quasi-instantaneously to changes in the concentration and phase (i.e. $\partial T/\partial t \approx 0$). Replacing $T \rightarrow T(t, x)$ in the model equations, 3.18, makes W , τ and k time and spatially dependent via equations 3.21 and 3.22, while the coupling parameter λ can be set to a constant.

It is found that it is more convenient to maintain the interface width W fixed with changing temperature, thus shifting the temperature dependence in equations 3.21 and 3.22 onto λ . In particular, comparing equation 3.21 at two different temperatures with the requirement that W stay fixed requires that λ change with tem-

perature according to

$$\lambda(T) = \frac{(1 - k(T)) c_l^{\text{eq}}(T) m(T)}{(1 - k(T_0)) c_l^{\text{eq}}(T_0) m(T_0)} \lambda(T_0) \quad (3.23)$$

where the subscript 0 refers to the temperature at $t = 0$ (ie. the first temperature of entry into the coexistence region) and $T \equiv T(t)$, the temperature at time t . After the simulations are completed, the record of $\lambda(T(t))$ is used with equations 3.21 and 3.22 to re-scale time and space axes back to real units.

3.4 Isothermal and Non-Isothermal Solidification of an Isomorphous Alloy

To demonstrate the feasibility of this approach, the dendritic solidification of an $A-B$ binary alloy with an isomorphous phase diagram as shown in Figure 3.1 is considered. This phase diagram is obtained by applying a common tangent construction to the phenomenological solid/liquid alloy free energies defined in [65]. The material properties of the $A - B$ alloy used are $L^A = 31000\text{J/mol}$, $L^B = 24622\text{J/mol}$, $c_p^A = 26.07\text{J/mol}$, $c_p^B = 24.02\text{J/mol}$, $T_m^A = 1728\text{K}$, $T_m^B = 800\text{K}$, identical to the material properties of a Ni-Cu binary alloy with the exception that the latent heats of Ni and Cu are about one half those values and the melting point of Cu is 1358K. The liquidus and solidus concentrations are given by

$$\begin{aligned} c_s^{\text{eq}}(T) &= \frac{1 - e^{-2\Delta T^A/RT}}{e^{-2\Delta T^B/RT} - e^{-2\Delta T^A/RT}} \\ c_L^{\text{eq}}(T) &= \frac{1 - e^{-2\Delta T^A/RT}}{1 - e^{(-2\Delta T^A + 2\Delta T^B)/RT}} \end{aligned} \quad (3.24)$$

where $\Delta T^i = L^i(T_m^i - T)/2T_m^i$ with $i = A, B$. From the liquid-solid coexistence concentrations in equation 3.24, the partition coefficient is given by $k(T) = c_s^{\text{eq}}(T)/c_L^{\text{eq}}(T)$ and $1/m(T) = dc_L^{\text{eq}}(T)/dT$ because this alloy system satisfies $K = 1$ in equation 3.5 for low enough concentrations.

The model equations, 3.18, are used to simulate both isothermal quenches (fixed $T = T_0$) and non isothermal cooling ($T = T_0 \rightarrow T(t)$) through the coexistence region of the phase diagram in figure 3.1. The parameters used in the model equations, 3.18, are determined dynamically using the temperature dependence of λ in equation 3.23, where the equations 3.3 and 3.24 are used to calculate $k(T)$ and $m(T)$. The interface kinetics are made to vanish by setting $\tau(T) = (d_0(T)^2/D)a_2\lambda^3(T)/a_1^2$ and equation 3.21 is used to compute the temperature dependent interface width $W(T)$. The value of $\lambda(T_0)$ is arbitrarily chosen but as the temperature evolves $\lambda(T)$ is chosen according to equation 3.23 in non-isothermal

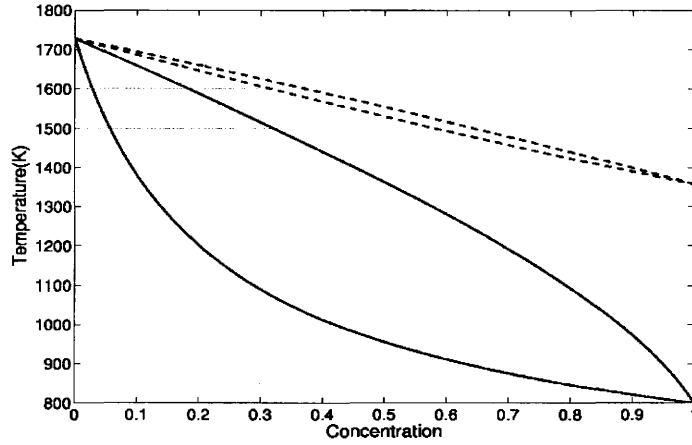


Figure 3.1: *Phase diagrams for Ni-Cu binary alloy (broken lines) and the A – B alloy studied in this work (solid lines).*

situations. As mentioned above, use of Equation 3.23 implies that W actually stays constant during the cooling process. The time scale, however, is changed by a factor $\tau(T)/\tau(T_0) = \Delta T/\Delta T_0$. Finally, without loss of generality, the temperature dependence in the surface energy, γ , is neglected.

First, isothermal two dimensional dendritic growth simulations are performed to investigate the convergence behavior of the tip radius and tip velocity for decreasing values of the coupling constant λ . Four different values of λ are examined, $\lambda = 1.5957, 2.1275, 3.1913, 4.2550$. The simulations have a numerical grid size set to $\Delta x = 0.4W(T_0)$ and the physical domain is chosen to be the same for all λ , $800 \times 800W$, $600 \times 600W$, $400 \times 400W$ and $300 \times 300W$, respectively. Explicit time-marching is used to solve the phase-field equations with a time step of $dt = 0.02, 0.02, 0.018$ and 0.014 , in units of $\tau(T_0)$, for the four λ , respectively.

In these simulations, the far-field concentration is chosen to be $C_L(\infty) = 0.1827$, corresponding to the liquidus concentration at 1600 K. The solidification quench temperature is set to $T_o = 1450$ K, corresponding to an equilibrium liquidus concentration of $C_L^{eq} = 0.3875$ and a partition coefficient $k = 0.1902$. Figure 3.2 displays the predicted variations of the steady state tip velocity and tip radius at the different values of λ . The tip velocity is found to converge faster than the tip radius as λ is decreased, however both are close to convergence for the value of $\lambda \approx 2.1275$. The corresponding centerline solute concentration is found to agree well with the Gibbs-Thomson relation $c_s/c_i^{eq} = k[1 - (1 - k)d_0\kappa]$ for all values of λ .

Next a simple case of non-isothermal solidification of the $A-B$ alloy is considered to investigate the convergence of this technique for transient processes. An $A-B$ alloy with initial concentration corresponding to the liquidus concentration at 1600 K is quenched to $T_0 = 1450$ K and is solidified isothermally until it approaches the steady state. The alloy is then quenched to a temperature of 1400K

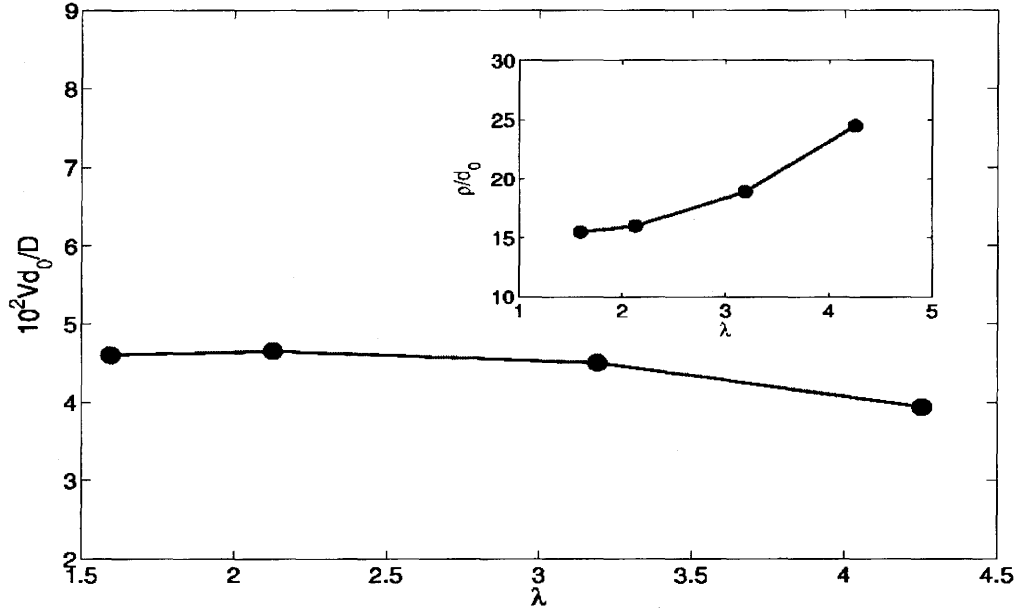


Figure 3.2: Predicted dimensionless steady-state tip velocities as a function of λ for isothermal solidification of the binary alloy in Figure (1), with $T_0 = 1450$ K and initial concentration corresponding to the liquidus concentration at temperature 1600 K. All simulations have the same physical domain and initial seed size, and the tip velocities are evaluated after steady state has been established. The inset shows the steady-state tip radius as a function of λ .

and a new steady state for the dendrite is reached. The temporal evolution of tip velocity and tip radius for the choices of $\lambda(T_0) = 2.1275$ and 3.1913 are shown in Figure 3.3. The relative change in the steady state tip velocity and radius after the new quench shows some dependence on the choice of $\lambda(T_0)$, this is consistent with the isothermal convergence test shown in Figure 3.2. After quenching to 1400 K, the temperature-dependent coupling constant becomes $\lambda(T) = 1.1803\lambda(T_0)$, therefore the convergence comparison occurs between two larger coupling constants and can be prone to an increase in error. These changes in the steady-state values are, however, within 10 % of each other, which is in reasonable agreement.

The solute field along the dendrite centerline is examined to demonstrate that the anti-trapping flux term in the concentration equation still successfully eliminates any excess solute changes due to the solute trapping effect caused by the diffuseness of the interface between solid and liquid phases [48]. Figure 3.4 shows the solute distribution along the dendrite centerline for the simulation of $\lambda(T_0) = 3.1913$ in Figure 3.3. The concentration profile is illustrated both with and without the use of anti-trapping in the phase field equations. It is found that solute partitioning in the solid obeys the Gibbs-Thomson relation quite well with the anti-trapping flux, and in the absence of the corrective term the concentration in the solid phase displays

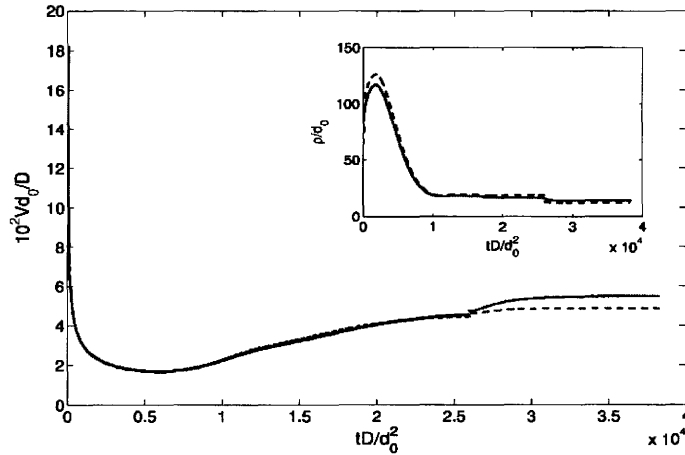


Figure 3.3: Comparison of temporal evolution of dimensionless tip velocity for non-isothermal solidification conditions corresponding to a quench to 1450 K and then to 1400 K for $\lambda(T_0) = 2.1275$ (solid line) and 3.1913 (broken line). The change in temperatures occurs at the jump in the curves. In the inset, the comparison of the temporal evolution of the corresponding (dimensionless) tip radius is displayed.

significant error.

Finally, a continuous cooling between two temperatures during the solidification process is considered. Using the same initial concentration from the previous numerical tests, the *A-B* alloy is cooled to 1450 K and isothermal solidification is allowed to proceed until the dendrite tip velocity approaches the steady state (~ 26000 dimensionless time steps as shown in Figure 3.5). The alloy is then step-wise cooled one degree at equal time intervals down to 1400 K, from time 26000 to 40000, following which isothermal solidification is continued at 1400 K. Figure 3.5 shows that the tip velocity and radius corresponding to $\lambda(T_0) = 2.1360, 2.4061$ and 3.1913 are fairly close to each other, indicating a good convergence of this method in the transient and steady state regimes. Figure 3.5 also shows the tip velocity and tip radius vs time for the case of $\lambda(T_0)=2.1360$ with no anti-trapping current used in the phase field equations (3.18). Without anti-trapping there is a systematic shift in the radius at all times and in the velocity over most of the time domain.

The centreline concentration along the dendrite axes for the three values of $\lambda(T_0)$ simulated in the data of 3.5 are plotted in Figure 3.6. The convergence of concentration for the different $\lambda(T_0)$ are in excellent agreement in both the transient and steady state regimes. Again the centreline concentration for $\lambda(T_0)=2.1360$ without anti-trapping is plotted and shows a very large deviation from the the solution with anti-trapping fluxes, the latter of which is found to obey the Gibbs-Thomson boundary condition.

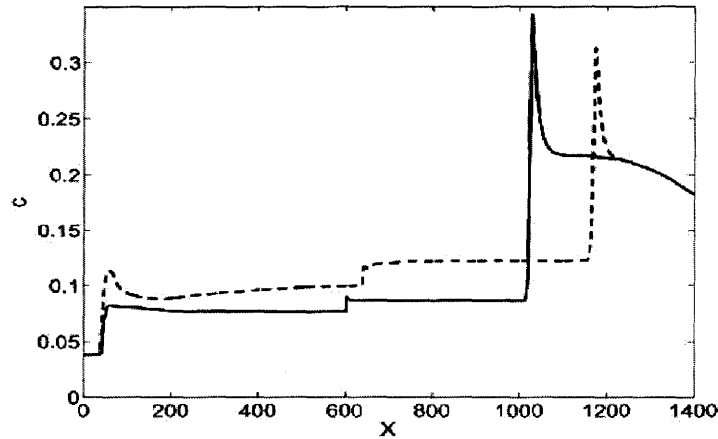


Figure 3.4: Plots of solute concentration (in molar fraction) along the centerline dendrite axis for the non-isothermal case corresponding to $\lambda(T_0) = 3.1913$ in Figure 3.3. The solid line corresponds to the case when anti-trapping is turned on, while the broken line corresponds to the case that anti-trapping is switched off. The x axis is in units of Δx corresponding to $\lambda(T_0) = 3.1913$.

3.5 Diffusion limited growth in Beta-Brass

The solid state transformation of α needles in β brass is investigated using the above quantitative phase field model to simulate the solute partitioning in needle growth in Cu-Zn. The phase diagram is as shown in Figure 3.7. It should be noted that semi-coherent boundary effects and volumetric strains were neglected in this part of the study. As a result, the comparison assumes the needle growth in beta-brass is solely diffusion limited. A series of simulated iso-thermal quenches are performed and the corresponding solid state dendrite tip velocities are measured for the resulting precipitates.

The simulations use a four fold symmetry to describe surface tension anisotropy. Each tip in the 4-fold structure is studied upon reaching an isolated needle at steady state. Strictly speaking, the morphologies of the α needle network morphology does not look like a collection of 4-fold dendrites, as shown in Figure 3.8 (a) and (b). This is to be expected as the simulations are for isolated dendrite arms while the experiments reflect a highly interactive dendrite environment. Interestingly, the tip morphology of the simulated needle agrees quite well with isolated tip morphologies from various experimental needles, as shown in Figure 3.8 (c) and (d).

For the examination of tip velocities, the alloy composition is set to $C_o^{Zn} = 0.441$ as per the experiments [54]. The anisotropy coefficient in the surface energy is set to a value of $\epsilon_4 = 0.01$ ¹ and the numerical convergence constant $\lambda(T_o)$ is set

¹Strictly speaking, without a correct measurement of the experimental anisotropy the velocity comparison presented here can only be semi-quantitative, where (as shown below) the anisotropy,

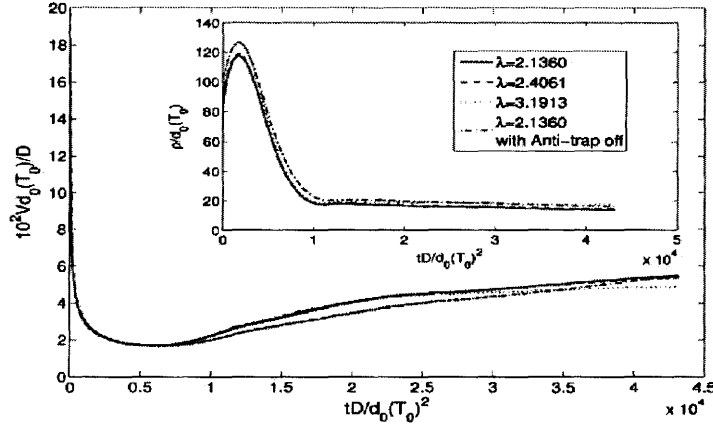


Figure 3.5: Temporal evolution of dimensionless tip velocity for non-isothermal solidification conditions corresponding to slowly cooling from 1450 K to 1400 K. Different values of $\lambda(T_0)$ are compared. In the inset, the comparison of the temporal evolution of the dimensionless tip radius for the same simulation parameters is displayed. Also displayed are the results for a case without anti-trapping in the phase field equations.

to a value of 1.6. A series of iso-thermal quenches were performed in the range of 308K to 524K and the corresponding partition coefficients and values of the equilibrium composition on the β side of the interface, $C_o^{eq\beta}$ were tabulated and are summarized in table 3.1

Temperature(K)	$C_o^{eq\beta}$	Partition coefficient k
454	0.4443	0.8618
427	0.4490	0.8599
400	0.4560	0.8605
373	0.4589	0.8496
346	0.4620	0.8357
319	0.4646	0.8173
291	0.4658	0.8016
264	0.4684	0.7891
237	0.4715	0.7705

Table 3.1: Equilibrium parameters extracted from phase diagram tables.

The temperature dependence of the diffusion coefficient for β brass is readily available in the literature [3]. The Kirkendall effect [21, 4] in β brass causes the diffusion coefficient of Zn in Cu, D_{Zn} , and Cu in Zn, D_{Cu} , to have two distinct values (as a function of temperature). In this work an effective diffusion coefficient

as well as the capillary length are scaled out of the data.

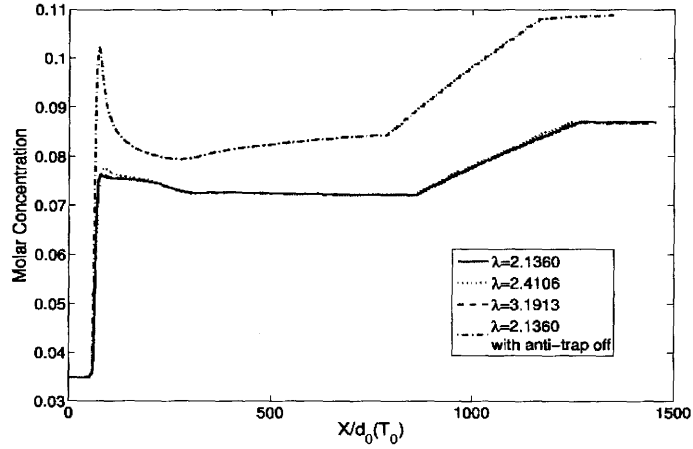


Figure 3.6: Plots of dendrite centreline solute concentration (in molar fraction) corresponding to the $\lambda(T_0)$ values simulated in the data of 3.5. For comparison a case without anti-trapping is also shown.

is used, determined from the alloy composition and the measured values of D_{Cu} and D_{Zn} as derived by,

$$D_{eff} = C_{Zn}D_{Cu} + C_{Cu}D_{Zn} \quad (3.25)$$

where C_{Zn} and C_{Cu} are the alloy compositions of Zn and Cu respectively. The values of the effective diffusion coefficients are summarized in table 3.2.

Temperature(K)	$D_{eff} \left(\frac{m^2}{s} \right)$
454	1.70E-8
427	1.13E-8
400	2.94E-9
373	1.07E-9
346	3.64E-10
319	1.16E-10
291	3.38E-11
264	9.00E-12
237	2.14E-12

Table 3.2: Effective diffusion coefficients calculated from equation 3.25

Performing a conversion of the simulated tip velocities to real units, as shown in Chapter 3, results in a velocity of the form,

$$V_R = \bar{V} \frac{D_{eff}}{d_o} \frac{1}{a_2 \lambda(T_0)^2} \quad (3.26)$$

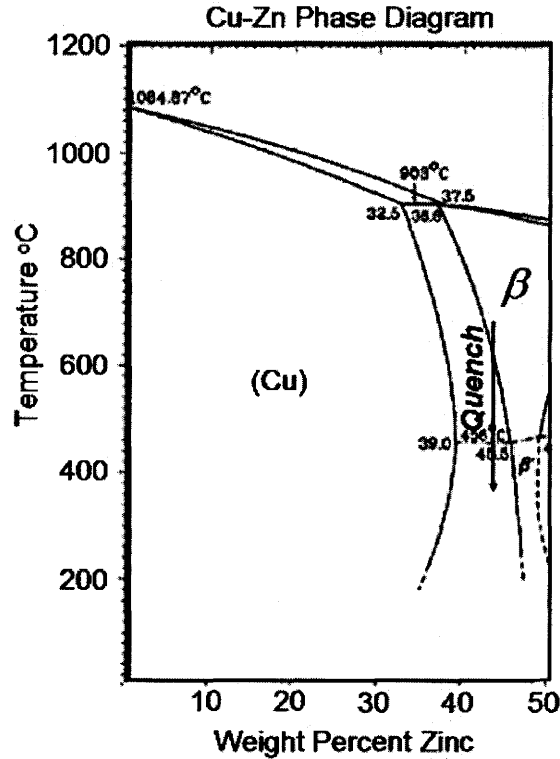


Figure 3.7: Cu-Zn Phase diagram. The iso-thermal quench range is marked into the co-existence region of β and $\alpha(\text{Cu})$.

where V_R is the velocity in units of $\frac{m}{s}$, \bar{V} is the velocity in the dimensionless units of the model, D_{eff} is the effective diffusion coefficient in units of $\frac{m^2}{s}$, d_o is the capillary length in units of m , $a_2 = 0.6267$ and $\lambda(T_o) = 1.6$. Capillarity measurements (d_o) for β brass are not readily available, nor is a corresponding measurement of the anisotropy of the capillarity. The growth rates depend heavily on the choice of the anisotropy and conversion to physical units requires a value of the capillarity, without experimental values for these quantities, only a semi-quantitative comparison of the growth rates is performed, assuming that neither the anisotropy nor the surface energy varies greatly with temperature.

To scale the velocities for comparison with the experimental velocities, both experiments and simulations are dimensionalized relative to a reference velocity, V_{ref} , chosen at $T = 423^\circ\text{C}$. This creates a new scaled velocity equation,

$$V_R^* = \frac{V_R}{V_{ref}} = \frac{\bar{V} D_{eff}}{\bar{V}_{ref} D_{effref}} \quad (3.27)$$

assuming that the surface energy and anisotropy are constant with temperature.

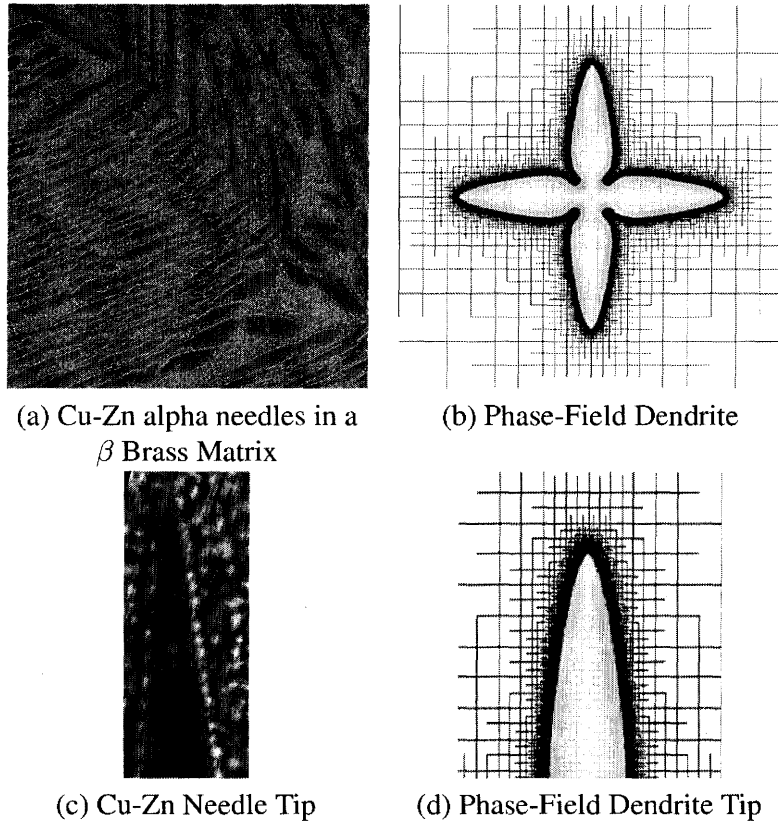


Figure 3.8: Morphological comparison of needle growth in β brass (*left*)[54] and a phase field dendrite (*right*). The simulated dendrite is performed with a four-fold anisotropy, tip velocities are measured and compared to the experimental growth rates of the needles.

This scaling makes it possible to compare simulation with experiment without knowing the capillary length and its anisotropy explicitly. The results of the scaled steady state velocities are plotted with the scaled experimental growth rates in Figure 3.9, indicating a reasonably good agreement.

The turnover of velocity is explained by a competition between the driving force of the transformation and the diffusion limited step. The supersaturation (driving force) of the transformation is found to decrease with increasing temperature, as expected. Conversely the diffusion rate (limiting step) increases with increasing temperature. A comparison of these two controlling factors, shown in Figure 3.10, illustrates the crossover trend of dominance, resulting in a peak in the velocity set in the growth rate of the needles, as shown in Figure 3.9.

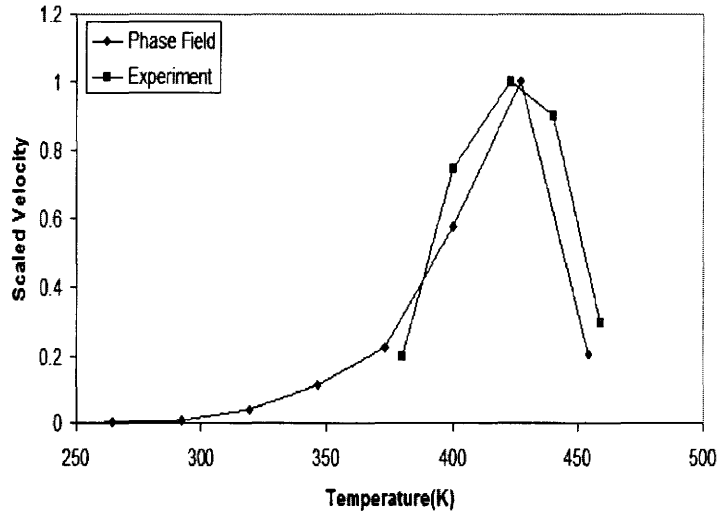


Figure 3.9: Simulated plots of tip growth velocities vs experimental β brass needle growth rates[54]. Both rates are scaled to the peak velocity $\frac{V}{V_{max}}$.

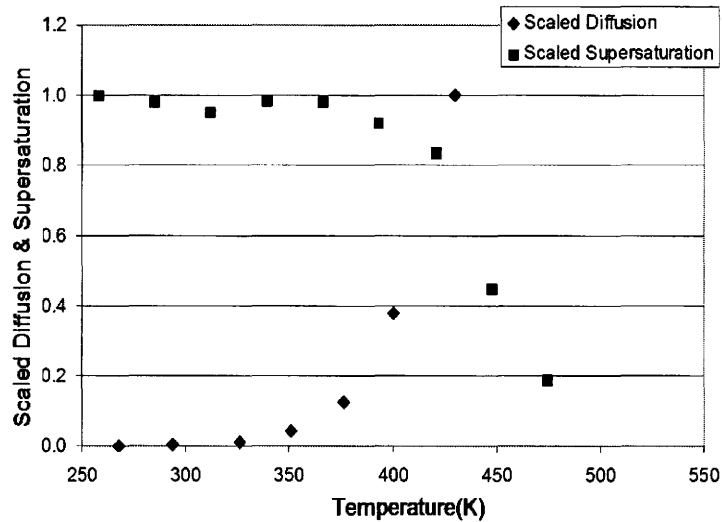


Figure 3.10: Plotted scaled values of the supersaturation and the diffusion coefficients in β brass as functions of the temperature. This illustrates the crossover competition between diffusion and thermodynamic driving forces for β Brass. Diffusion is scaled as $\frac{D}{D_{Max}}$ and Supersaturation as $\frac{\Omega}{\Omega_{Max}}$

Chapter 4

Incorporating Elasticity in the Phase Field Model

Chapter 3 developed a mathematical modification to an existing binary alloy phase field model [8] for the application of *non-linear* phase diagrams. The contribution enables the exploitation of the thin interface asymptotic analysis developed by the previous authors [8, 49]. This chapter further develops the model of Chapter 3 to incorporate elasticity for the use in solid-state transformations. It shows that most of the relationships allowing for a thin interface, which were examined in Chapter 3, may be brought to bear on phase transformations involving elasticity if certain conditions apply.

This chapter begins with the sharp interface kinetic equations from section 1.1.1 with the addition of corrective terms for the elastic free energy. In section 4.2 the phase field free energy is constructed in the form presented in Equation 3.15 with the addition of an elastic free energy. New phase field equations of motions are presented in section 4.3. In section 4.4 the thin interface composition field is projected onto a sharp interface and the results are compared with the theoretical sharp interface elastic correction to the interface composition presented in section 4.1. Finally, anisotropic elasticity is simulated about a growing coherent solid state precipitate and an approximation to the anisotropic strain field is fitted to the simulation results.

4.1 Sharp Interface Kinetics of Phase Transformations with Elasticity

With the addition of elasticity the Gibbs-Thomson condition, equation 1.3, can be expressed as

$$C_B^{int} = C_{L,S} - G_{ele} \quad (4.1)$$

where $C_{L,S}$ is the interfacial composition as defined by equation 3.1, G_{ele} is a corrective term for the elastic free energy change across the interface. The kinetic

attachment coefficient (β_k) is effectively zero in these solid state simulations, since the interfacial velocity is slow enough to neglect that correction. Also, reverting back to an ideal binary alloy for simplicity, the partition coefficient is taken to be independent of temperature as

$$k = \frac{C_A^{\text{eq}}}{C_B^{\text{eq}}} = \text{constant} \quad (4.2)$$

It should be noted that the temperature dependency of the phase-field equations in chapter 3 could hold here, however it is omitted here for simplicity.

In addition to the additional term in the Gibbs-Thomson condition, elastic boundary conditions are imposed on the precipitate interface. The displacement on either side of a coherent interface must be equal and is expressed as

$$U_i^A = U_i^B \quad (4.3)$$

Where A is the parent phase and B is the precipitate phase. The radial forces normal to the interface must be balanced. This is given by the equation

$$\sigma_{nn}^A - \sigma_{nn}^B = 0 \quad (4.4)$$

$$\sigma_{ns}^A - \sigma_{ns}^B = 0 \quad (4.5)$$

where n is the direction normal to the interface, s is the direction along the arc length in curvilinear coordinates and σ^i is the normal stress on the i th side of the interface.

4.2 Phase Field Elastic Free Energy Functional

The Gibb's free energy functional for a binary alloy begins with the form presented in Chapter 3 without elasticity effects. The free energy in equation 3.14 is coupled to the elastic free energy of Equation 1.8, wherein each bulk component is now dependent upon the order parameter (ϕ). This energy is defined by

$$G(\phi, c, \epsilon_{ij}) = |W_o \nabla \phi|^2 + f(T) - S(\phi)(T - T_m) + \frac{RT}{\nu} (c \ln c - c) + \epsilon(\phi)c + f_{el}(\phi) \quad (4.6)$$

The elastic free energy is defined by Hooke's law, given by

$$f_{el}(\phi) = C_{ijkl}(\phi)(\epsilon_{ij} - \epsilon^*(\phi))(\epsilon_{kl} - \epsilon^*(\phi)) \quad (4.7)$$

where ϵ_{ij} is the total strain, $\epsilon^*(\phi)$, equation 1.34, is the total eigenstrain, $\epsilon_{ij}^*(\phi) = \frac{1+g(\phi)}{2}\epsilon_{ij}^{*1L} + \frac{1-g(\phi)}{2}\epsilon_{ij}^{*2L}$ (ϵ_{ij}^{*1L} and ϵ_{ij}^{*2L} are the eignestrains in phase 1 and 2 (parent and precipitate), respectively). The phase dependent compliance tensor is also

interpolated across the interface from their bulk phase values by equation 1.33, $C_{ijkl} = \frac{1+g(\phi)}{2}C1_{ijkl} + \frac{1-g(\phi)}{2}C2_{ijkl}$ and the interpolation function $g(\phi)$ has the form given in equation 1.18

The elastic energy can be re-cast as a function of $g(\phi)$, leaving the elastic free energy in the form of

$$f_{el} = Z_3 (g(\phi))^3 + Z_2 (g(\phi))^2 + Z_1 g(\phi) + Z_0 \quad (4.8)$$

This energy is still a generalized free energy, however each pre-factor of one of the powers of $g(\phi)$, Z_3 , Z_2 , Z_1 and Z_0 , is a non-linear function of the strains and the components of the elastic modulus tensor, best evaluated through the use of mathematical software such as Maple. Explicit expressions for Z_i are given in the appendix (App A.2) for the cubic elastic modulus tensor in two-dimensions.

The parameters of $G(\phi, c, \epsilon_{ij})$ are constructed so that the free energy self-consistently reproduces some relevant thermodynamic properties of a general binary alloy phase. The chemical interpotential defined by $\mu_i(T) = dG_i/dc|_{c_i^{eq}}$ for an elastic energy that is independent of composition gives a partitioning relationship as

$$k \equiv \frac{c_s^{eq}}{c_L^{eq}} = \exp\left(-\frac{(\epsilon_s - \epsilon_L)\nu}{RT}\right) \quad (4.9)$$

by equating $\mu_s = \mu_L$, identical to the form in chapter 3.

A double tangent construction is performed on the elastic Gibbs free energy functional, equation 4.6, for each constituent bulk phase (i.e. $\phi = -1$ or $\phi = 1$). This produces a modification to the equilibrium composition C_b^{eq} by the additional term G_{el} which corrects for the presence of an elastic strain field. For the case of a constant strain in each phase, this new equilibrium composition is given as,

$$C_b = C_b^{eq} - G_{ele} = \frac{(T - T_m)L\nu}{T_m TR(1-k)} - \frac{2\nu(Z_3 + Z_1)}{TR(1-k)} \quad (4.10)$$

where $C_b^{eq} = \frac{(T-T_m)L\nu}{T_m TR(1-k)}$ is the equilibrium coexistence line (i.e. concentration) corresponding to the parent phase in the absence of elasticity, and $G_{ele} = \frac{2\nu(Z_3+Z_1)}{TR(1-k)}$ is the correction to the phase diagram due to a local change in the strain.

4.3 A Phase Field Model For Elastically Influenced Phase Transformations

Incorporating the elastic free energy of the previous section into the phase field model, the following evolution equations for the phase field, the dimensionless supersaturation $U = \frac{e^u - 1}{1-k}$, and the strain (or displacement) fields are derived (see appendix for details):

Phase Mobility:

$$\begin{aligned} \tau_o A(\hat{n})^2 \frac{\partial \phi}{\partial t} &= \hat{\nabla} \cdot [W_o^2 A(\hat{n})^2 \hat{\nabla} \phi] \\ &+ \hat{\nabla} \cdot \left(|\hat{\nabla} \phi|^2 W_o^2 A(\hat{n}) \frac{\partial A(\hat{n})}{\partial (\hat{\nabla} \phi)} \right) \\ &- (\phi^3 - \phi) - \lambda(1 + B)U(1 - \phi^2)^2 \end{aligned} \quad (4.11)$$

Chemical Diffusion:

$$\begin{aligned} \Psi \frac{\partial U}{\partial t} &= \vec{\nabla} \cdot (D\bar{q}(\phi)C_b \vec{\nabla} U) \\ &+ (1 + (1 - k)U)C_b \left(1 + \frac{\alpha Z_2}{C_b(1 - k)} \right) \frac{\partial \phi}{\partial t} \\ &- (1 + (1 - k)U) \left(\frac{k + 1}{1 - k} - \phi \right) \frac{\partial C_b}{\partial t} \end{aligned} \quad (4.12)$$

Strain Relaxation:

$$\frac{\partial \sigma_{ij}}{\partial x_j} \equiv \frac{\partial}{\partial x_j} \left(\frac{\partial G(\phi)}{\partial \epsilon_{ij}^e} \right) = 0 \quad (4.13)$$

The explicit form of B in equation 4.11 is

$$B = \frac{1}{2(1 - k)} \left(\left(\frac{\alpha Z_1}{(1 - k)C_b^{eq}} - 1 \right) \frac{\alpha Z_2}{C_b} g(\phi) - \frac{\alpha Z_1}{C_b^{eq}} \right) \quad (4.14)$$

where here C_b is the equilibrium composition corrected for the local strain. Assuming Z_3 is negligible, this is given by $C_b = C_b^{eq} - \frac{1}{2} \frac{\alpha Z_1}{(1 - k)}$ where C_b^{eq} is the equilibrium composition in the absence of elasticity, while $\alpha = \frac{4\nu}{RT}$ modulates the elastic coefficients to the energy units of the model.

The dimensionless supersaturation ($U = \frac{e^u - 1}{1 - k}$) is modified to incorporate the elastic correction to the equilibrium composition by modification to the dimensionless measure of the deviation from the equilibrium chemical potential (u) through interpolation function matching outlined in appendix B. The resultant equation is,

$$u = \ln \left(\frac{2C}{C_b} \left(k + 1 - (1 - k)g(\phi) - \frac{1}{2} \frac{\alpha Z_2}{C_b} (1 - g(\phi)^2) \right)^{-1} \right) \quad (4.15)$$

where Z_2 is the prefactor to $g(\phi)^2$ in the elastic free energy and C_b is the equilibrium interfacial composition corrected for elasticity by equation 4.10. Ψ modulates the diffusion through the interface correcting for the diffuse nature of ϕ and is given by

equation 4.16.

$$\Psi = C_b(k + 1 - (1 - k)\phi - \frac{Z_2\alpha}{2C_b}(1 - \phi^2)) \quad (4.16)$$

Two-sided diffusion is controlled by the function $\tilde{q}(\phi) = q(\phi)\frac{\Psi}{C_b}$ where $q(\phi)$ modulates the diffusion in the two phases, to simulate equal diffusion coefficients $q(\phi) = 1$. By setting the diffusion coefficients equal in both phases the need for the anti-trapping flux correction term described in section 1.4.2 is eliminated due to the coefficient $a_t = 0$. Surface energy anisotropy is entered into the model by $A(\hat{n})$ using the four-fold anisotropy described in equation 1.17.

This model is studied in the limit where $Z_3 \rightarrow 0$, the condition for a small difference in the elastic coefficients in either phase. This condition holds for all materials in which $\frac{Z_3}{Z_1} \ll 1$ holds. Generally speaking $Z_1 > Z_3$ even in the most extreme disparities of the elastic coefficients, so this assumption is not unreasonable.

Equations 4.11 and 4.12 are presented in the form of the phase field equations (Equations 3.18) introduced in chapter 3. Equation 4.11 has a correction (1+B) to the term containing the dimensionless undercooling (U). This correction is a strain dependent modification of this dimensionless equation. Equation 4.12 has the term Ψ multiplying the time rate of change of the undercooling which is corrected for strain. This term is similar to the multiplying factor in the chemical diffusion equation in the phase field equations of Chapter 3 with the addition of a correction for the strain. In addition to this pre-factor an additional term proportional to $(\frac{\partial C_b}{\partial t})$ is introduced.

Following the procedure for the derivation of the phase field model presented in [8] and extended in chapter 3, the constants W_o , τ_o and λ are inter-related by an asymptotic analysis [49], which maps the phase field model onto the sharp interface limit. Attaining the limit where the interface kinetic coefficient, $\beta_k(\vec{n}) = 0$, in the Gibbs-Thomson condition $C_{int} = C_{eq} - \Delta C d_o(\vec{n})\kappa - \Delta C\beta(\vec{n})V$, requires $\frac{d_o}{W} = 0.8839\lambda$ and $D = 0.6267\lambda$. These relations arise by expansion of the phase (ϕ) and composition (ϕ) inside of the interface and matching to the sharp interface limits [8].

The inter-relationship of W_o , τ_o and λ (discussed in chapter 3) are assumed to be at least approximate in the formulation of the elasticity-corrected phase field model presented in this chapter. This can be checked by comparing the phase field equations in the form presented in Equations 4.11 and 4.12 to the equations in the absence of elasticity (Equations 3.18). The phase field model presented in this chapter is identical to the one of Chapter 3 in the limit when:(a) $\frac{\partial C_b}{\partial t} \ll 1$ in Equation 4.12 which is numerically found to be at least an order of magnitude smaller than the other terms in this equation and (b) when $B \ll 1$, which is also about an order of magnitude smaller than 1. B accounts for the effect of a variable strain field on the development of the precipitate. This is analogous to the temperature dependence of λ presented in chapter 3. With correction terms described above being

small, it is expected that a thin interface analysis of this more complex phase field model will still yield to lowest order the same thin interface parameter relations as the original model of Karma and co-worker. An even more simplistic argument is that even if the elastic terms of our model induce spurious kinetics in the thin interface limit, they will not significantly perturb the interface away from its [elasticity-corrected] equilibrium since only very small growth rates are being considered here.

It should also be noted that both of these terms are zero in the limit of zero strain, but are also valid for small lattice eigenstrains. For larger strains these approximations are valid when the interfacial velocity (V) is small, in effect this small velocity eliminates the excess kinetic effect at the interface. In this thesis only small eigenstrains ($\epsilon^* \approx 0.005$) and small growth rates ($V < 1\mu m/s$) are considered.

4.4 Growth of an Isotropic Second Phase Precipitate with Coherent Interfaces in an Isotropic Parent Phase

To confirm that the model (Equations 4.11-4.13) reproduces the expected elastic correction to the Gibbs-Thomson condition in equation 4.10 an isotropic second phase precipitate is quenched into a coexistence region. The surface energy is made isotropic by setting the surface energy anisotropy coefficient $\epsilon_4 = 0$ in equation 1.17. The elasticity solver is formulated in terms of cubic tensor coefficients, ie C_{11}, C_{12} and C_{44} as described in appendix A.2. For isotropic linear elastic coefficients the cubic elastic terms are related by,

$$C_{44} = \frac{1}{2}(C_{11} - C_{12}) \quad (4.17)$$

where for this simulation $C_{11} = 1011$ and $C_{12} = 729$ (C_{ij} is dimensionalized by α) and a coherent hydrostatic eigenstrain is set to a strength of $\epsilon^* = 0.005$. The constant λ (i.e. the convergence constant in the phase field equation) is set to a value of $\lambda = 3$, the equilibrium composition is $C_b^{eq} = 0.1$ with an initial alloy composition of $C_o = 0.04$ and the partition coefficient is set to a value of $k = 0.1$. The diffusion coefficients are set equal in both phases thus removing the phase dependency in the diffusion coefficient (ie. $q(\phi) = 1$) in equation 4.12.

A precipitate particle is grown under the conditions of the previous paragraph. A cross section of the composition field solved by Equation 4.12 is shown in Figure 4.1. The figure also indicates the corresponding value of the equilibrium interfacial composition as calculated by equation 4.10 where the curvature term is neglected by choosing a precipitate radius such that this correction is negligible. C_b is plotted as a function of the phase by interpolating it through the interface to its corresponding

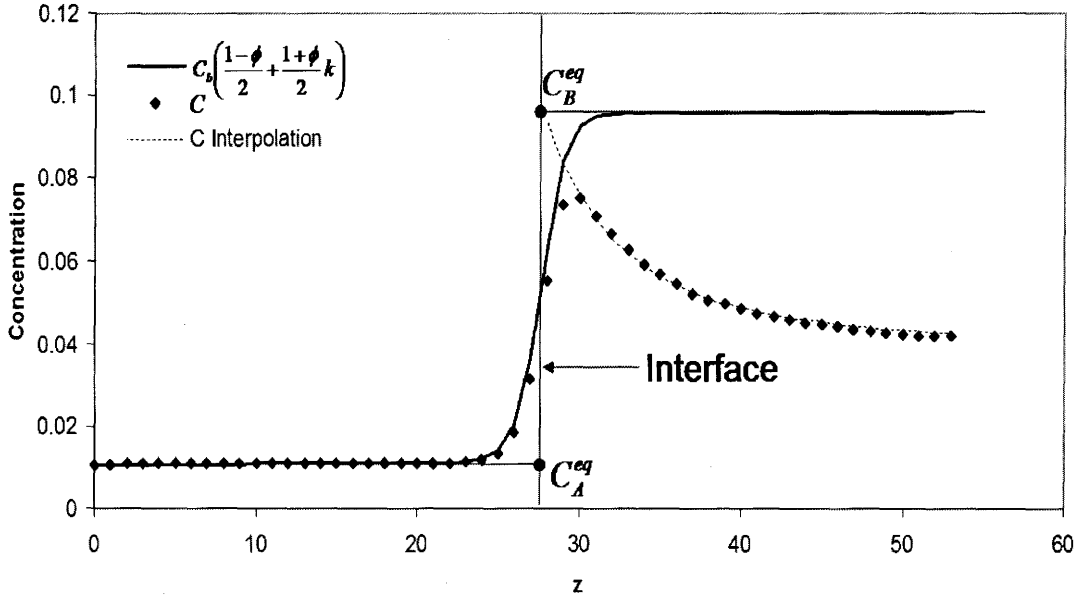


Figure 4.1: A circular isotropic coherent precipitate is grown in an alloy with initial composition of $C_o = 0.04$ with a hydrostatic lattice eigenstrain of $\epsilon^* = 0.005$. A cross section of the composition is shown with the corresponding equilibrium composition corrected for strain, $C_b \left(\frac{1-\phi}{2} + \frac{1+\phi}{2}k \right)$. The compositions are interpolated to the center of the interface and are found to be in good agreement with the sharp interface boundary condition.

precipitate side value by $C_b \left(\frac{1-\phi}{2} + \frac{1+\phi}{2}k \right)$. The composition field is interpolated to the interface described by the point where $\phi = 0$ both from inside the precipitate bulk and from outside the precipitate in the parent phase. The points are denoted C_A^{eq} and C_B^{eq} and are found to have good agreement with the interpolations to the center of the interface.

4.5 Approximation of the Strain Field Around a Precipitate with Cubic Elastic Coefficients

The elastic field is analyzed around a circular precipitate to investigate the behaviour of an anisotropic elastic strain tensor for cubic coefficients that are equal in both phases. The anisotropy is entered into the cubic elastic coefficients by introducing a deviation from the isotropic relation in equation 4.17 as defined here by,

$$C_{44} = \frac{1}{2}(C_{11} - C_{12}) + \beta \quad (4.18)$$

where β is the deviation from the isotropic elastic coefficients. C_{11} and C_{12} remain unchanged. While the analytical solution to the isotropic strain field has been derived for elliptical inclusions under a hydrostatic eigenstrain [17], a solution to an anisotropic precipitate under the same conditions is mathematically cumbersome [70]. Instead, a perturbed form for the strain field is considered.

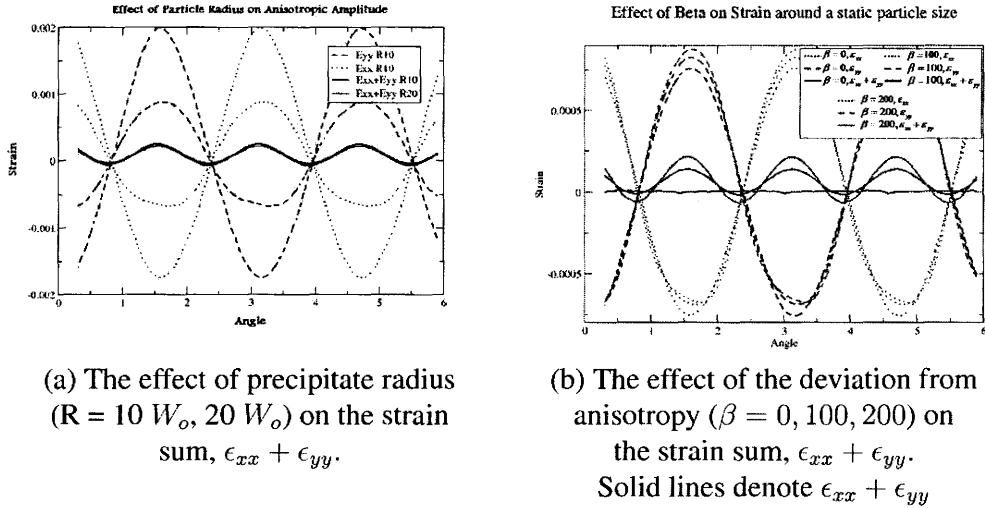


Figure 4.2: Strain fields ϵ_{xx} , ϵ_{yy} and their sum for two particle radii with $\beta = 200$ in units of the model. Strain fields ϵ_{xx} , ϵ_{yy} and their sum for a constant particle radius and varied β .

A circular precipitate in a parent phase with identical elastic coefficients in both phases is considered. The dimensionless elastic coefficients are set to values of $C_{11} = 1011$ and $C_{12} = 729$ (C_{ij} is dimensionalized by α , ie. αC_{ij}), the hydrostatic eigenstrain is set to $\epsilon^* = 0.005$ and the concentration field is made constant.¹ The deviation from elastic isotropy is studied by two controls, the particle radius and the strength of the deviation from isotropic elasticity, β .

The effect of the precipitate radius is studied first by setting the value of β to 200 (in dimensionless units of the model, ie. $\alpha\beta$) and varying the precipitate radius. The resultant strain fields along iso-radius contours just outside of the precipitate interface are plotted in Figure 4.2 (a) for two precipitate radii, $R = 10, 20$ in units of the interface width W_o . With an increase in particle radius it is found that individually each orthogonal component to the strain field, ϵ_{xx} and ϵ_{yy} , is also increased a proportional amount. However, the trace of the strain tensor is found to remain essentially unchanged with increasing particle radius.

¹The elasticity here is not influenced by compositional effects and therefore any concentration field will produce similar results.

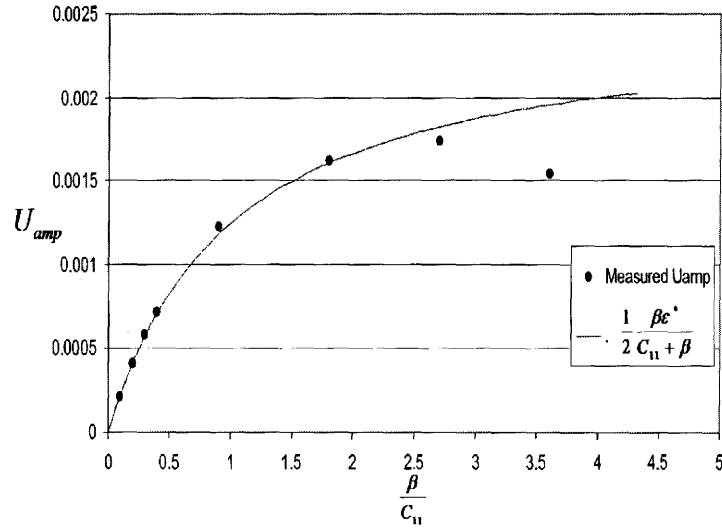


Figure 4.3: Measured values of U_{amp} plotted vs $\frac{\beta}{C_{11}}$ and the fitted prediction of $\frac{1}{2} \frac{\beta \epsilon^*}{C_{11} + \beta}$

Next the effect of increasing the anisotropic parameter β while maintaining a constant particle radius is investigated. Unlike the case where particle radius was increased, each individual component of the diagonal terms of the strain tensor has little relative change in their magnitude. However, the amplitude of the variation in the trace of the elastic tensor has a notable increase, as shown in Figure 4.2 (b) for anisotropic values of the elastic tensor of $\beta = 0, 100, 200$.

The θ dependence of the strain trace can be approximated to lowest order by a single Fourier mode as defined by,

$$\epsilon_{xx} + \epsilon_{yy} = U_{amp} \cos(4\theta) \quad (4.19)$$

To elucidate the form for the fourier mode amplitude, U_{amp} , the anisotropic strength β is varied and the values of U_{amp} are measured for the corresponding waveform at the interface of the precipitate. These measured values are fitted to a functional form, given by the equation,

$$U_{amp} = \frac{1}{2} \frac{\beta \epsilon^*}{C_{11} + \beta} \quad (4.20)$$

The functional form of equation 4.20 shows good agreement for all values of β in the regime where $\frac{\beta}{C_{11}} < 2$ as shown in figure 4.3. This range of anisotropies is well within the limits of the relative anisotropic strengths that will be further studied in this thesis.

Chapter 5

Morphological Transitions Due to Elastic and Surface Energy Competitions

Competing growth materials properties, such as surface energy anisotropy and temperature gradients, can cause transitions in the dominant growth morphology of precipitate structures.[63, 85] In the presence of an anisotropic influence dendritic structures can form. If however there are multiple anisotropic influences these anisotropic fields interact leading to the emergence of various off-dendritic structures. If the anisotropic influences are of similar form, but are simply out of phase, two extreme phenomena can occur. In one extreme, the anisotropic fields destructively interfere causing the precipitates to grow as if under isotropic conditions. Conversely the anisotropic fields can amplify and strengthen the preferential growth direction of the dendrite. The understanding of how these fields interact is of importance in the formation of a precipitate structure.

In this chapter the phase field model presented in chapter 4 is used to investigate how the competition between the anisotropic nature of both the surface energy and the cubic elastic energy affects the growth morphology of precipitates. The analysis of the morphology considers the Gibbs-Thomson condition, modified for anisotropic elasticity and including surface energy anisotropy, coupled with the Mullins-Sekerka linear stability analysis of growing precipitates [60]. A scaling mechanism is derived for determining the transition between dominant growth directions.

Section 5.1 reports on simulations that illustrate how the material properties affect dendritic morphologies in solid state precipitates. In section 5.2 phase field simulations are used to elucidate the transition point between the dominant growth planes by consideration of both the Gibbs-Thomson modification to the interface composition due to elasticity and the linear stability analysis of growing interfaces.

5.1 Conditions Influencing the Structure of Precipitates

Three distinct controlling influences on the selection of a dominant morphology of precipitated dendrites are characterized. These controlling properties are the supersaturation and the anisotropies in the surface energy and elastic tensor. The effect of each of these parameters are systematically tested by increasing the strength of the test parameter while holding the other parameters constant.

In the following phase field simulations, the free parameter λ is set to a value of $\lambda = 3$ and as required by the sharp interface phase field sharp-interface analysis, while the dimensionless diffusion coefficient is set to $D = 0.6267\lambda$, which makes $\beta = 0$ via Equation 1.22. The equilibrium composition is set to $C_b^{eq} = 0.1$ and the partition coefficient used is $k = 0.1$. The elastic coefficients were converted to units of the model by the elastic modulating factor $\alpha = 6.005 \cdot 10^{-9} \frac{m^3}{J}$ and in these units the elastic coefficients are set to a value of $C_{11} = 1011$ and $C_{12} = 729$, where $C_{ij} = \alpha C_{ij}$.

Precipitate structures are grown in a system with periodic boundaries, where the system size is set to $6400W \times 6400W$, W being the interface width. The precipitates grew to sizes of at most $2000W$ and the solution to the displacement field drops off as $1/R$. This justifies the claim that purely isolated precipitates are studied while using the periodic boundaries. The diffusion coefficients and elastic coefficients have no phase dependence. The grid spacing is set to $dx = 0.4W$.

5.1.1 Elastic Anisotropy (β)

The elastic anisotropy emerges from the elastic tensor, where C_{11} , C_{12} and $C_{44} = \frac{1}{2}(C_{11} - C_{12}) + \beta$. The anisotropy of the tensor is varied by holding C_{11} , C_{12} constant and varying C_{44} through changes in β . Figure 5.1 (a-c) shows the effect of increasing the strength of the elastic anisotropy by increasing C_{44} while holding all other parameters constant (surface energy anisotropy ϵ_4 and average concentration C_o). From left to right the values of β used are $\beta = 25, 100, 400$ respectively. As can be seen in this figure, small elastic anisotropy causes the surface energy to dominate and the dendrite grows in the $[10]$ direction (Figure 5.1 (a)). When the elastic anisotropy is increased to sufficient strength (Figure 5.1 (c)) the dendrite grows in the $[11]$ direction. When the anisotropies effectively destructively interact the resultant structure leads to an almost isotropic growth morphology (Figure 5.1 (b)).

5.1.2 Surface Energy Anisotropy (ϵ_4)

The surface energy anisotropy is entered into the model using the simple form for 4-fold surface energy $\gamma = \gamma_o(1 - \epsilon_4 \cos(4\theta))$ (ie. $A(\vec{n})$ function in the phase field

model Equation 1.17). The effect of surface energy anisotropy is controlled by varying ϵ_4 and holding both the super saturation ($\Omega = 0.555$ through C_o) and the elastic anisotropy ($\beta = 400$) constant. Figure 5.1 (e-f) shows the effect of increasing the strength of the surface anisotropy with these constant parameters. From left to right in Figure 5.1 the values of the ϵ_4 used are $\epsilon_4 = 0.01, 0.03, 0.05$ respectively. As with the effect shown in section 5.1.1 for an increasing β , increasing the strength of ϵ_4 causes the morphology to transform from a preferential growth along the [11] direction (Figure 5.1 (d)) to that of the [10] direction (Figure 5.1 (f)) with a transition region where the precipitate structure is isotropic (Figure 5.1 (e)).

5.1.3 Supersaturation(Ω)

The supersaturation is varied by changing the initial alloy composition C_o . Figure 5.1 (g-i) shows the effect of decreasing the supersaturation while holding the strength of the surface anisotropy and elastic anisotropy constant. From left to right the values of the initial alloy composition used are $C_o = 0.04, 0.06, 0.08$ respectively. For large super saturations (Figure 5.1 (g)) the growth direction is dominated along directions preferred by the surface energy, i.e. the [10] directions. As the supersaturation is decreased a transition from the [10] growth direction to the [11] direction is observed (Figure 5.1 (h) and (i)).

5.2 Characterization of the Morphological Transition

This section provides a method to predict the transition point of the dominant precipitate growth direction. In section 5.1 three effects were shown to combine to create a transition between dominant growth directions: the anisotropy in the capillarity, the anisotropy in the elastic fields and the supersaturation of the material, the latter of which is linked to the selected tip radii of the precipitates. The point at which this transition occurs is defined and measured by examining the envelope of the precipitate tips in $R - \theta$ space. It is found that the amplitude of the envelope allows the critical surface energy anisotropy parameter (ϵ_4^C) for a specified elastic anisotropy (β) to be determined. With a measured relationship for ϵ_4^C and β the radius needed to scale the transition curves is found by balancing the Gibbs-Thomson corrections for surface energy Vs. elastic anisotropy. This radius is found to be proportional to the Mullins-Sekerka critical radius of instability (R^C). Finally, with the Gibbs-Thomson condition and the Mullins-Sekerka critical radius, a condition relating ϵ_4^C as a function of β and R^C at the transition is proposed.

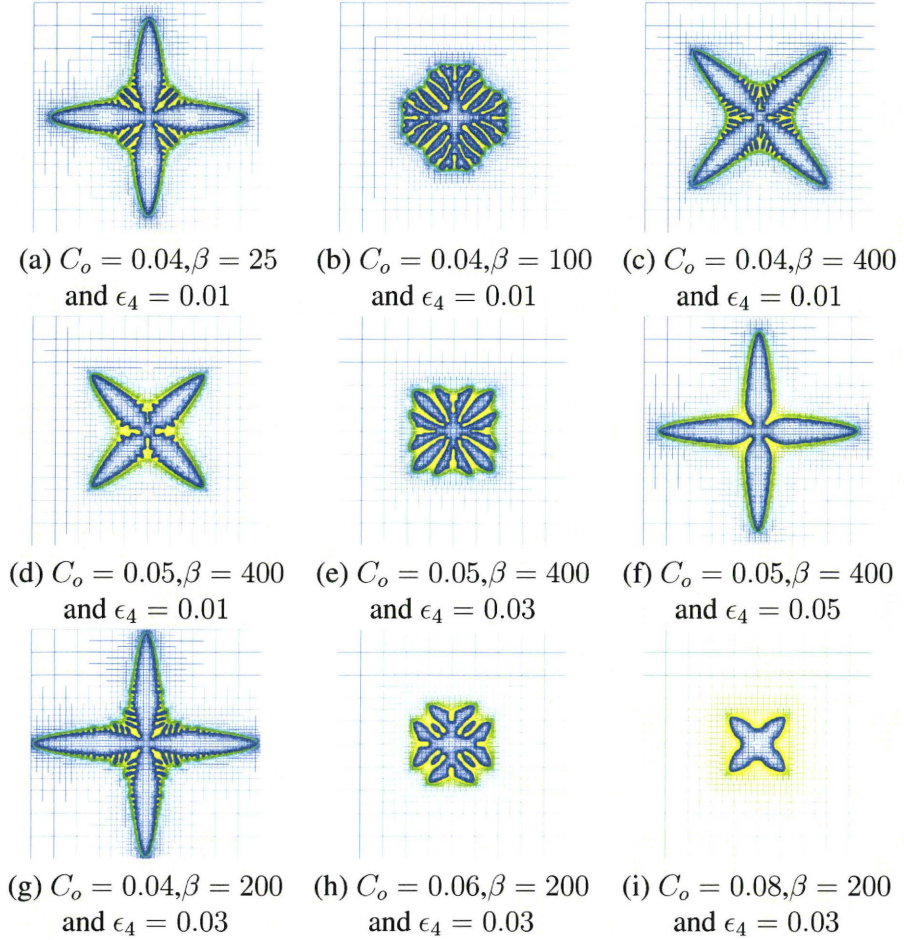


Figure 5.1: *Morphologies of growth precipitates for variations in the elastic anisotropy (a-c), surface energy anisotropy (d-f) and in the supersaturation (g-i). The composition field is plotted on the adaptive mesh, blue being low concentration and yellow is a higher concentration. The total system size is $6400W$, plotted is an area of $2000W$ on one side. C_o is the average concentration and ϵ_4 controls the surface energy anisotropy.*

5.2.1 Defining the Transition Point Between Dominant Growth Directions

The transition point that characterizes the controlling mechanism of growth morphology is the point at which all competing anisotropies exactly cancel. Under this condition an isolated precipitate will grow (ideally) as a circle (a sphere in three dimensions) until the interface becomes unstable by the Mullins-Sekerka criteria. While in this case the interface will become unstable, the envelope around the par-

ticle will continue to grow as a spheroid. It is this envelope that allows the point of transition to be characterized.

Envelope of Precipitates

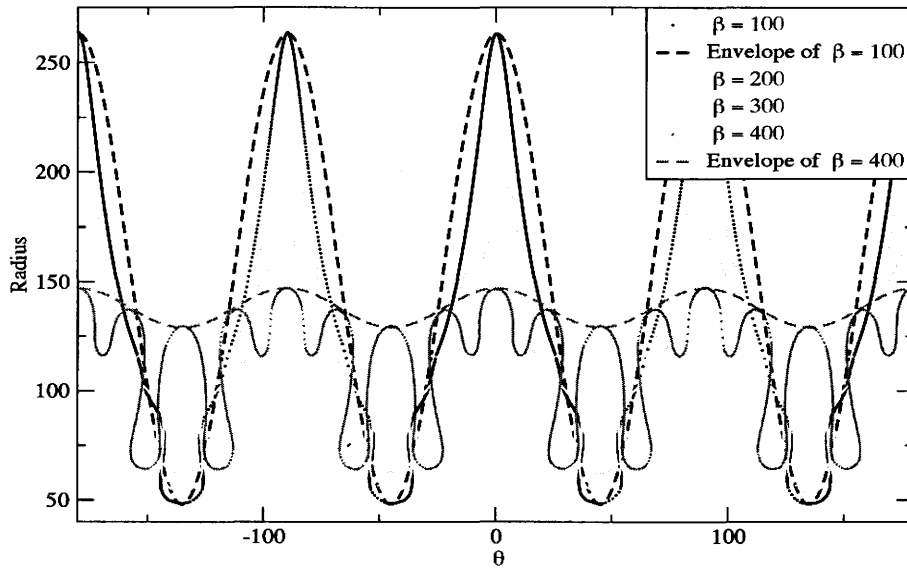


Figure 5.2: $R - \theta$ space of 4 precipitates with varied β values, $\epsilon_4 = 0.03$ and super saturation = 0.666. The dashed lines illustrate the envelope of the precipitate, as the control values approach a transition point, the envelope amplitude goes to 0.

The concept of the precipitate envelope is illustrated in Figure 5.2 where the interface for 4 precipitates with values of $\beta = 100, 200, 300, 400$, $\epsilon_4 = 0.03$ and $\Omega = 0.666$ in $R - \theta$ space are plotted, where $\Omega = \frac{C_b^{eq} - C_o}{(1-k)C_b^{eq}}$. The dashed line shows the envelope surrounding the interface. As the magnitude of β approaches the transition point the amplitude of the envelope decreases, approaching zero.

5.2.2 Measurement of the Critical Surface Anisotropy (ϵ_4^C)

The critical surface energy anisotropic coefficient, denoted ϵ_4^C , is the value of ϵ_4 at a given supersaturation and β which results in an envelope amplitude of zero. ϵ_4^C is interpolated from the amplitudes of the precipitate envelopes by varying ϵ_4 for given values of the supersaturation Ω and elastic anisotropy β .

The envelope amplitude is approximated by measuring the difference of the total growth distance from the center of the precipitate along the [10] direction to the growth distance along the [11] direction. The transition point is the interpolated value for ϵ_4 such that these amplitudes approach zero. Seven different supersaturations are run where ϵ_4 is varied between 0.005 and 0.05 and β is varied from 100 to

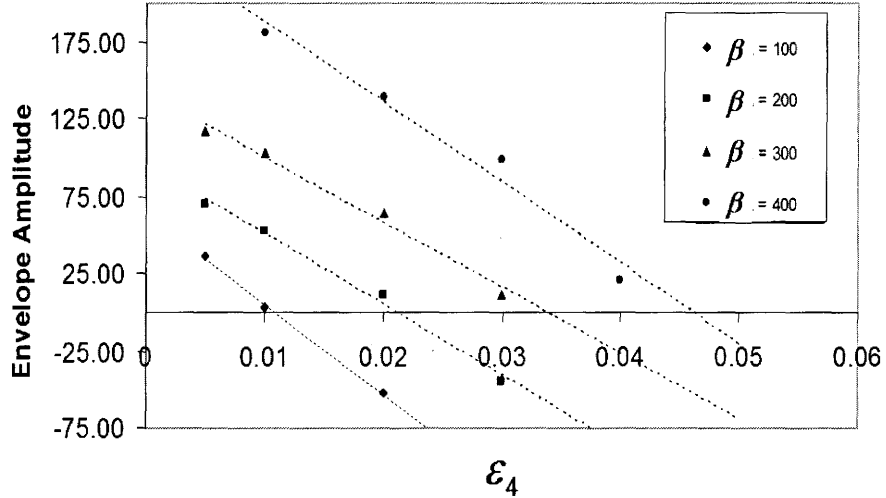


Figure 5.3: Interpolation of ϵ_4^C by examination of the envelope amplitude (in units of W) for different values of β . The alloy composition is $C_o = 0.06$. Fits are used to interpolate to the transition point where the amplitude of the envelope goes to zero. The negative amplitudes denote a phase shift as the direction of orientation switches from one growth direction to another.

400. The ratios are measured at arbitrary times, chosen in each case such that the precipitate is grown to a sufficient size as to have outgrown any initial transients.

For each value of β at each alloy composition C_o , the envelope amplitude is plotted vs ϵ_4 . Figure 5.3 illustrates this for an alloy with an average composition of $C_o = 0.06$, and the deviation from elastic isotropy is characterized for values of $\beta = 100, 200, 300, 400$. For each value of β , the data is fitted linearly and is interpolated to the transition line to extract the critical surface anisotropic value $\epsilon_4^C(\beta, \Omega)$. A linear relationship between ϵ_4^C and β is found for each of the selected supersaturations. These linear relationships are plotted in Figure 5.4 for the alloy compositions of $C_o = 0.04, 0.05, 0.06, 0.07$. Figure 5.4 thus predicts that

$$\epsilon_4^C = A_{C_o}\beta \quad (5.1)$$

where the fitting parameter A_{C_o} has values of $A_{0.04} = 6.84 \cdot 10^{-5}$, $A_{0.05} = 8.33 \cdot 10^{-5}$, $A_{0.06} = 10.68 \cdot 10^{-5}$ and $A_{0.07} = 16.98 \cdot 10^{-5}$ for the given supersaturations.

5.2.3 Critical Tip Radii at the Transition Point

The competing anisotropic effects cancel when all correction terms that are dependent on the interface normal angle (θ) in the interfacial equilibrium composition ($C_b^{int} = C_b^{eq} - \Delta C_{capillarity}(1 + 15\epsilon_4 f(\theta)) - \Delta C_{elastic}(1 - \epsilon_e h(\theta))$) exactly cancel.

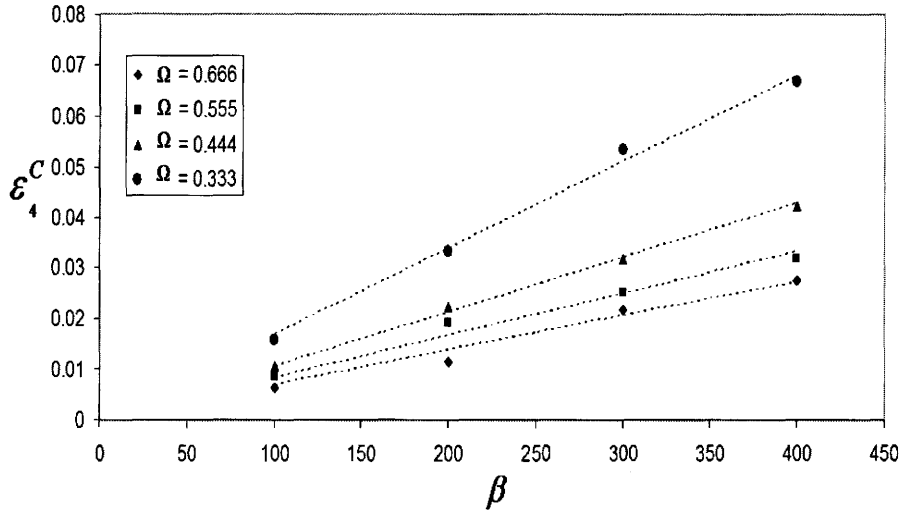


Figure 5.4: The relationship between ϵ_4^C and β is extracted by fitting their plots. Shown here are the ϵ_4^C vs β for 4 supersaturations, $\Omega = 0.666$, $\Omega = 0.555$, $\Omega = 0.444$, $\Omega = 0.333$.

$\Delta C_{capillarity}$ and $\Delta C_{elastic}$ are the isotropic corrections to interfacial equilibrium composition and ϵ_4 and ϵ_e represent the strength of the surface energy and elastic energy anisotropies. Assuming a linear fourier expansion with a 4-fold symmetry in both $f(\theta)$ and $h(\theta)$ (ie. $\cos(4\theta)$) the terms of the solute correction can be grouped by order of the fourier expansion.

$$C_b^{int} = C_b^{eq} - (\Delta C_{capillarity} + \Delta C_{elastic}) - (\epsilon_{surf} - \epsilon_{ele}) \cos(4\theta) \quad (5.2)$$

where $\epsilon_{surf} = 15\epsilon_4\Delta C_{capillarity}\kappa$ and $\epsilon_{ele} = \epsilon_e\Delta C_{elastic}$ are the relative anisotropic strengths of the surface energy correction and the elastic energy correction respectively. The factor of 15 in the capillarity term comes from the stiffness of the capillarity, $d_o(\vec{n}) = d_o(1 + 15\epsilon_4\cos(4\theta))$. The elastic anisotropy strength ϵ_e is yet to be determined but is linked to the strength of the elastic anisotropy through β . For an isotropic morphology to emerge the coefficient $\cos(\theta)$ term in Equation 5.2 is required to vanish, ie.

$$\epsilon_{surf} - \epsilon_{ele} = 0 \quad (5.3)$$

In Equation 5.2 the capillarity term ($\Delta C_{capillarity}$) contains a curvature correction, while the elastic term ($\Delta C_{elastic}$) does not. When these terms cancel a curvature κ is selected, which will be associated with a critical radius R_{trans}^C , ie. $\kappa_c = 1/R_{trans}^C$. From Equation 1.3 the capillarity correction is $\Delta C_{capillarity} = (1 - k)d_oC_b^{eq}$ and

substituting to calculate ϵ_{surf} results in a surface anisotropy strength of

$$\epsilon_{surf} = \Delta C_{capillarity} 15\epsilon_4 \kappa = 15C_b^o(1-k)d_o\epsilon_4 \kappa \quad (5.4)$$

The total elastic correction for cubic coefficients is defined by Equation 4.10 as $\Delta C_{elastic} = \frac{1}{2} \frac{Z_1}{1-k} = \frac{1}{4} \frac{C_{11}+C_{12}}{1-k} \epsilon^{*2} (1 - \frac{\epsilon_{xx}+\epsilon_{yy}}{\epsilon^*})$. In the absence of elastic anisotropy the strain trace ($\epsilon_{xx} + \epsilon_{yy}$) is zero as shown in Section 4.5. Therefore

$$\Delta C_{elastic} = \frac{1}{4} \frac{C_{11} + C_{12}}{1-k} \epsilon^{*2} \quad (5.5)$$

ϵ_{ele} is calculated by consideration of the anisotropy in the strain field as calculated in Section 4.5. Substituting Equation 4.19 for $\epsilon_{xx} + \epsilon_{yy}$ gives

$$1 - \frac{\epsilon_{xx} + \epsilon_{yy}}{\epsilon^*} = 1 - \frac{U_{amp}}{\epsilon^*} \cos(4\theta) = 1 - \epsilon_e \cos(4\theta) \quad (5.6)$$

where U_{amp} is defined by Equation 4.20 and $\epsilon_e = \frac{U_{amp}}{\epsilon^*}$. This results in ϵ_{ele} becoming

$$\epsilon_{ele} = \frac{1}{8(1-k)} \frac{C_{11} + C_{12}}{C_{11} + \beta} \beta \epsilon^{*2} \quad (5.7)$$

Substituting Equations 5.4 and 5.7 into Equation 5.3 and solving, the critical radius of curvature required to maintain isotropic conditions is given by,

$$R^C = 120(1-k)^2 C_o^l d_o \frac{(C_{11} + \beta)}{\epsilon^{*2}(C_{11} + C_{12})} \frac{\epsilon_4^C}{\beta} \quad (5.8)$$

A fit to a selected critical radii is attained by substituting the fitted equation for the critical surface anisotropy coefficient, ϵ_4^C given by equation 5.1 and by choosing a reference point of $\beta = 0$. This results in a relationship for the magnitude of the $\beta = 0$ transition radius that depends on concentration through A_{C_o} in Equation 5.1 given as,

$$R_{trans} = \frac{120(1-k)^2 (C_{11}) C_o^l d_o}{(C_{11} + C_{12}) \epsilon^{*2}} A_{C_o} \quad (5.9)$$

The next section will produce a method by which to predict this radius without the need for measured values of A_{C_o} .

5.2.4 Linear Stability Calculation of the Transition Tip Radius (R_C)

In the previous section a selected precipitate radius is derived based on the interpolated values for the critical surface energy anisotropy. However, this method re-

quires a physical measurement of the relationship between ϵ_4^C and β by measuring the value of A_{C_o} . A method by which to approximate the selected radius by theoretical consideration of the Mullins-Sekerka linear stability analysis on an isotropic particle is now shown.

Mullins and Sekerka in 1963 [60, 53] predict a critical particle size $R_{k=2}^* = 11R^*$, where $R^* = \frac{2d_o}{\Omega}$, after which the particle interface becomes unstable. A particle at the transition point can be considered to be an isotropic particle in a supercooled matrix. The difference from the Mullins and Sekerka treatment is in the nature of the supersaturation. The supersaturation of the precipitate under elastic strain is modified by the elasticity such that the elastic supersaturation is redefined to be $\Omega_{el} = \frac{C_b - C_o}{(1-k)C_b}$, where C_b is the equilibrium interface composition with corrections due to elasticity, equation 4.10. This supersaturation is used in the linear stability analysis to arrive at a minimum critical radius of,

$$R_{MS} = 22 \frac{d_o}{\Omega_{el}} \quad (5.10)$$

A comparison of this instability radius with the fitted radius of equation 5.9 shows excellent linear agreement as shown in figure 5.5. Equation 5.9 is calculated

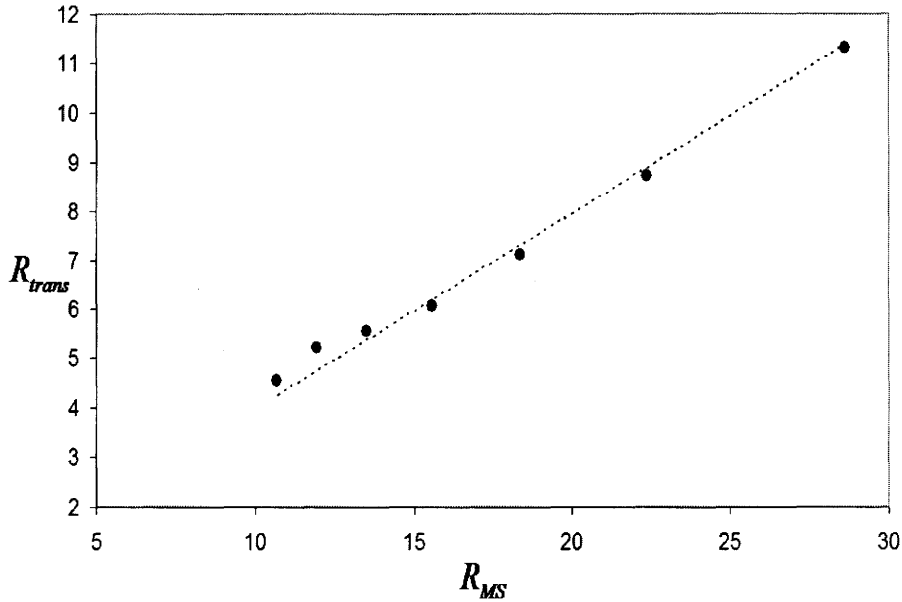


Figure 5.5: The fitted critical tip radius for isotropic growth, from equation 5.9, vs the onset Mullins-Sekerka wavelength for seven different supersaturations.

such that $C_{11} + \beta \rightarrow C_{11}$ in Equation 5.8. The R_{trans} dependence on β is reintroduced through its relationship to ϵ_e by the term $\frac{1}{C_{11} + \beta}$. The final result for the

critical selected radius as a function of β and Ω_{el} is

$$R_C = \frac{44}{5} \frac{d_o}{\Omega_{el}} \left(1 + \frac{\beta}{C_{11}}\right) \quad (5.11)$$

5.2.5 Calculation of the Critical Transition Point

With a predicted value for the critical tip radius, determined by the supersaturation, the required measurement of the relationship between ϵ_4^C and β can be eliminated. The linear stability prediction of the critical radius, given by equation 5.11 is substituted back into the equation for the isotropic criteria for the selected radius, equation 5.8. The resultant equation is solved for the critical surface energy anisotropy pre-factor (ϵ_4^C) versus beta, given by the equation,

$$\epsilon_4^C = \frac{11}{150} \frac{C_{11} + C_{12}}{(1 - k)^2 (C_{11} + \beta) C_o^i \Omega_{el}} \epsilon^{*2} \beta \left(1 + \frac{\beta}{C_{11}}\right) \quad (5.12)$$

This equation describes the transition points as a function of supersaturation (Ω), elastic anisotropy (β) and the anisotropy of the capillarity (ϵ_4). The transition lines for $\Omega_{el} = 0.606, 0.479, 0.353, 0.226$ are plotted in figure 5.6. Precipitates grown above the transition line will grow in the 10 directions while growth for conditions below the line will grow along 11 directions. Some morphologies are overplotted above and below the transition line for $\Omega = 0.606$ in figure 5.7 to further illustrate the transition points.

Equation 5.9 is the main result of Chapters 4 and 5. It makes an explicit prediction regarding the morphological selection of solid state precipitates growing in a host matrix with anisotropic surface energy and elastic coefficients. The parameters in this equation can be measured experimentally in order to validate these phase field predictions.

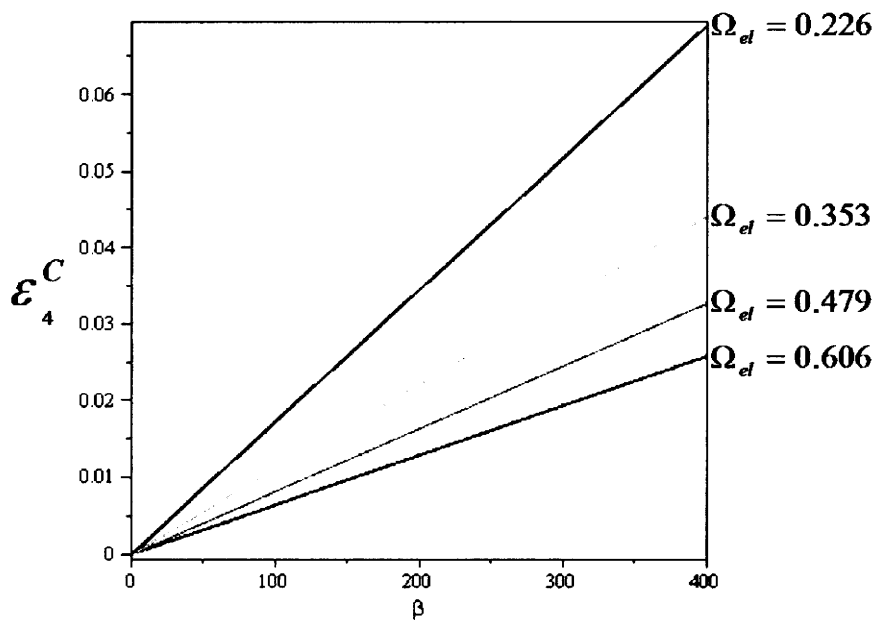


Figure 5.6: The critical transition points from equation 5.12. Above the line the precipitates prefer to grow in directions that minimize the surface energy [10], and below the directions which minimize the elastic energy [11]. Transition lines for different Ω_{el} are plotted.

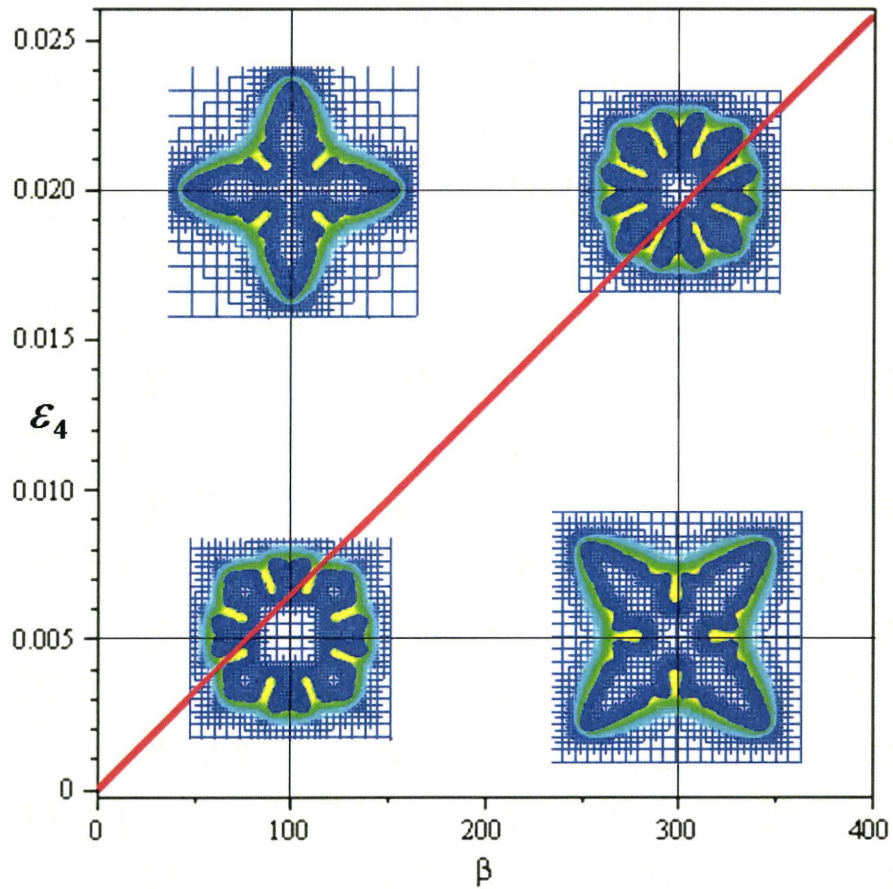


Figure 5.7: The critical transition line from equation 5.12. Above the line the precipitates prefer to grow in directions that minimize the surface energy [10], and below the directions which minimize the elastic energy [11]. The curve is plotted vs beta for $C_o = 0.04(\Omega_{el} = 0.606)$. Overplotted are 4 simulations corresponding to different values of ϵ_4 and β . The plotted line represents the value of ϵ_4^C , the transition point where anisotropies cancel out.

Chapter 6

Summary

The goal of this thesis was to develop a phase field model for the transformation of solid state precipitates and to use this model to help elucidate the pattern formations that occur during solid state transformations. The phase field model developed in Chapter 3 illustrates a technique that allows for the simulation of alloys that have non-linear phase diagrams using a model the mathematics of which was originally developed strictly for dilute alloys by Karma and coworkers [49, 8]. Chapter 4 further develops this model to incorporate an elastic free energy in order to study strain energy effects. These two advances allow for the simulation of solid state precipitates with elastic effects using the sharp interface analysis developed in the solidification model which enables artificial widening of the interface width without losing any of the pertinent physics. Therefore, much larger microstructures can be computed and studied without an increase in computational power.

Also in this thesis a new numerical adaptive mesh algorithm is developed that was tailored specifically for a finite difference numerical scheme. This algorithm places densely packed grid points about regions of importance and sparsely packed grid points in regions of unimportance. This has two added benefits. First larger domain sizes can be simulated with the same amount computer memory and secondly the simulation time is greatly decreased. The choice of a finite difference adaptive mesh stemmed specifically due to finite differencing algorithms being computationally faster than finite elements. In addition to this it is found that the elastic fields of growing precipitates could be relaxed using Gauss-Seidel iteration in strictly $O(N)$ time.

The adapted phase field model and newly developed numerics were used to study and predict a transition between dominant growth directions in the presence of competing anisotropies (In this case the surface energy [10] and elastic energy [11]). This competition is quantified in Chapter 5 by analysis of the Gibb-Thomson condition using a numerical solution to the anisotropic elastic field and a consideration of the Mullins-Sekerka instability.

Appendix A

Appendix - Numerical Techniques

A.1 Finite Differencing

Many different techniques are used to discretize and solve partial differential equations. Discussed here is a simple technique of discretizing differential equations through which the continuum equations can be solved approximately on a discrete grid. Consider a mesh, as shown in Figure A.1 (left). Each node in this mesh can be denoted by a unique node number N_i .¹ This is known as global referencing. However, every node can also be mapped onto a local grid, Figure A.1 (right), where each local node can exist at the center of its own minimesh and its nodal neighbours are assigned a local node number n_i ² based on its orientation to the central node.

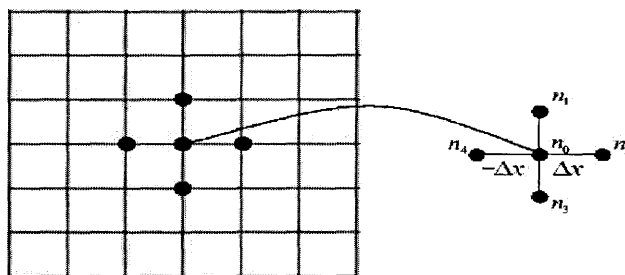


Figure A.1: *Global and Local coordinates in a 2D mesh used in a finite difference solver.*

Partial Differential equations can be discretized by approximating the derivatives with a Taylor expansion of a function f at a node about one of its neighbours from the local minimesh. For example the node n_0 can be expanded about its neigh-

¹ $i = 0, 2, \dots, m - 1$, where m is the total number of nodes in the global mesh

² $i = 0, 2, \dots, q - 1$, where q is the total number of nodes on the local mesh

bour n_2 as

$$n_2 = n_0 + \Delta x \left. \frac{df}{dx} \right|_{x_{local}=0} + \frac{\Delta x^2}{2!} \left. \frac{d^2f}{dx^2} \right|_{x_{local}=0} + \frac{\Delta x^3}{3!} \left. \frac{d^3f}{dx^3} \right|_{x_{local}=0} + \dots \quad (\text{A.1})$$

given that the grid spacing $\Delta x = |n_o - n_2|$.

Approximation of the derivatives in this manner introduces some error in the calculation. For explicit differentiation some of this error can be minimized by increasing the order over which the derivatives are calculated. The error is reduced in this manner by expanding over multiple grid points and combining their expansions, for example taking the expansion about n_4 as well as n_2 and subtraction of the two equations gives a difference equation of

$$n_2 - n_4 = 2\Delta x \left. \frac{df}{dx} \right|_{x_{local}=0} + 2 \frac{\Delta x^3}{3!} \left. \frac{d^3f}{dx^3} \right|_{x_{local}=0} + \dots \quad (\text{A.2})$$

This particular difference form is known as central differencing. Equation A.2 can be solved for the first order derivative, given as

$$\left. \frac{df}{dx} \right|_{x_{local}=0} = \frac{n_2 - n_4}{2\Delta x} - \frac{1}{2\Delta x} \left(\frac{\Delta x^3}{3!} \left. \frac{d^3f}{dx^3} \right|_{x_{local}=0} \right) + \dots \quad (\text{A.3})$$

and results in a discrete approximation of the first order derivative with an error of the order $O(\Delta x^3)$.

A.1.1 Finite Difference Templates of Gradient Operators

The technique above is used to develop the finite difference templates for the explicit solutions to the phase and chemical diffusion equations presented in chapters 3 and 4, as well as the templates used to solve implicit solution to the static displacement fields for elasticity by Gauss-Seidel iteration. In the equations below i and j are orthogonal cartesian coordinates, dx is the grid spacing and X is the field parameter being discretized.

Templates for Explicit Solutions

Derivatives to the phase and composition functions are expanded to include diagonal node neighbours in addition to the closest node neighbours to minimize anisotropy introduced by grid asymmetry. One such finite difference template was developed by examining the fourier transform of this discretization [30]. The Lapla-

lian operator is given as

$$\nabla^2 X = \frac{1}{2}(X_{i,j+1} + X_{i,j-1} + X_{i+1,j} + X_{i-1,j}) + \frac{1}{4}(X_{i+1,j+1} + X_{i+1,j-1} + X_{i-1,j+1} + X_{i-1,j-1}) - 3X_{i,j}(dx^2)^{-1} \quad (\text{A.4})$$

and a single derivative is given by

$$\frac{\partial X}{\partial x_i} = \frac{(X_{i+1,j+1} + X_{i+1,j-1}) - (X_{i-1,j+1} + X_{i-1,j-1})}{4dx} \quad (\text{A.5})$$

Templates for Gauss-Seidel iteration of Elastic Fields

The Gauss-Seidel iteration discussed in section A.3 uses a lower order template. Any grid errors that arise are minimized by additional relaxation steps. The Laplacian operator is given as

$$\nabla^2 X = \frac{(X_{i,j+1} + X_{i,j-1} + X_{i+1,j} + X_{i-1,j}) - 4X_{i,j}}{dx^2} \quad (\text{A.6})$$

and a single derivative is given by

$$\frac{\partial X}{\partial x_i} = \frac{X_{i+1} - X_{i-1}}{2dx} \quad (\text{A.7})$$

A.2 Cubic Elastic Free Energy Coefficients

In the generalized elastic portion of the phase field free energy, as described by equation 4.8 $f_{el} = Z_3 (g_3(\phi))^3 + Z_2 (g_3(\phi))^2 + Z_1 g_3(\phi) + Z_0$, several terms Z_3 , Z_2 , Z_1 and Z_0 are introduced. These coefficients are dependent on the particular values of the elastic modulus tensor in either of the precipitate or matrix phases. Presented here are the explicit forms for these functions for two sided cubic modula and a hydrostatic elastic eigenstrain of the form,

$$\epsilon_{ij}^* = \begin{vmatrix} \epsilon^* & 0 \\ 0 & \epsilon^* \end{vmatrix}.$$

and the elastic modulus tensor is described as introduced in section 1.2 and its phase dependence in section 1.5. The zeroth order component(Z_0) has no dependence on

the phase at all and is calculated to be

$$\begin{aligned}
 Z_0 = & \frac{1}{4}(C1_{11} + C2_{11})(\epsilon_{xx} - \frac{\epsilon^*}{2})^2 \\
 & + \frac{1}{4}(C1_{11} + C2_{11})(\epsilon_{yy} - \frac{\epsilon^*}{2})^2 \\
 & + \frac{1}{2}(C1_{12} + C2_{12})(\epsilon_{xx} - \frac{\epsilon^*}{2})(\epsilon_{yy} - \frac{\epsilon^*}{2}) \\
 & + (C1_{44} + C2_{44})\epsilon_{xy}^2
 \end{aligned} \tag{A.8}$$

This pre-factor has no dependence of phase (nor concentration) and therefore it does not appear in either the phase mobility equation (equation 4.11) or the chemical diffusion equation (Equation 4.12) since the growth kinetics are dependent on differences of energy. It does however appear in the static elasticity equation (Equation 4.13).

The first order component is the most prominent term in the model equations and is calculated to be

$$\begin{aligned}
 Z_1 = & \frac{1}{8}(3(C1_{11} + C1_{12}) + C2_{11} + C2_{12})\epsilon^{*2} \\
 & - \frac{1}{2}(C1_{11} + C1_{12})(\epsilon_{xx} + \epsilon_{yy})\epsilon^* \\
 & + \frac{1}{4}(C1_{11} - C2_{11})(\epsilon_{xx}^2 + \epsilon_{yy}^2) \\
 & + \frac{1}{2}(C1_{12} - C2_{12})\epsilon_{xx}\epsilon_{yy} \\
 & + (C1_{44} - C2_{44})\epsilon_{xy}^2
 \end{aligned} \tag{A.9}$$

The second order coefficient to the elastic energy in terms of the phase is calculated to be

$$\begin{aligned}
 Z_2 = & \frac{1}{8}(3(C1_{11} + C1_{12}) - (C2_{11} + C2_{12}))\epsilon^{*2} \\
 & + \frac{1}{4}(C2_{11} + C2_{12} - C1_{11} - C1_{12})(\epsilon_{xx} + \epsilon_{yy})\epsilon^*
 \end{aligned} \tag{A.10}$$

and in the presence of equal elastic coefficients this term becomes a constant, independent of strain.

The third order component is calculated to be

$$Z_3 = \frac{1}{8}(C1_{11} - C2_{11} + C1_{12} - C2_{12})\epsilon^{*2} \tag{A.11}$$

and has no dependence on the dynamic strain field. In the presence of equal elastic coefficients this term vanishes completely.

A.3 Static Elastic Solution for the Displacement Fields by Gauss-Seidel Iteration

Equation 1.9 is solved by Gauss-Seidel iteration [28]. This iterative technique discretizes the equations and solves for each local component of these equations. These iteration "templates" are coupled and are iterated until the solution converges to within a defined threshold. The templates for the 2-D displacement fields that satisfy the elastic static equilibrium equation (Equation 1.9) are derived for two sided cubic elastic coefficients using the finite different templates of Equations A.6 and A.7 and are derived to be,

$$U_{x_{i,j}} = \frac{\phi_x(P_0U_{xx} + P_2U_{yy} + 2P_3dx) + \phi_yP_1(U_{xy} + U_{yx})}{8(P_4 + P_5)}g(\phi)' + \frac{4P_5U_{x+y} + 4P_4U_{x+x} + P_6U_{yxy}}{8(P_4 + P_5)} \quad (\text{A.12})$$

and

$$U_{y_{i,j}} = \frac{\phi_y(P_0U_{yy} + P_2U_{xx} + 2P_3dx) + \phi_xP_1(U_{xy} + U_{yx})}{8(P_4 + P_5)}g(\phi)' + \frac{4P_5U_{y+x} + 4P_4U_{y+y} + P_6U_{xyx}}{8(P_4 + P_5)} \quad (\text{A.13})$$

where P_i are functions of the phase and the elastic modulus tensor C_{ijkl} and are defined in section A.3.1, $g(\phi)' = \frac{\partial g(\phi)}{\partial \phi}$ and the subscripted terms of U and ϕ are grid discretizations with respect to coordinates i and j as described in section A.3.2.

A.3.1 Elastic Coefficient Pre-factors to the Discretized Displacement Templates

For cubic elastic coefficients with a hydrostatic lattice eigenstrain the pre-factors P_i are calculated to be:

$$\begin{aligned} P_0 &= \frac{1}{2}(C1_{11} - C2_{11}) \\ P_1 &= \frac{1}{2}(C1_{44} - C2_{44}) \\ P_2 &= \frac{1}{2}(C1_{12} - C2_{12}) \\ P_3 &= \frac{1}{2}\epsilon_1^*L[(C2_{11} + C2_{12} - C1_{11} - C1_{12})g(\phi) - C1_{11} - C1_{12}] \\ P_4 &= \frac{1}{2}(g(\phi)(C1_{11} - C2_{11}) + C1_{11} + C2_{11}) \\ P_5 &= \frac{1}{2}(g(\phi)(C1_{44} - C2_{44}) + C1_{44} + C2_{44}) \\ P_6 &= \frac{1}{2}(g(\phi)(C1_{44} + C1_{12} - C2_{44} - C2_{12}) + C2_{44} + C1_{44} + C2_{12} + C1_{12}) \end{aligned}$$

where P_0, P_1 and P_2 become 0 when the elastic coefficients are equal on either side of the interface.

A.3.2 Discretized Terms of U_i and ϕ_i

Equations A.12 and A.13 are dependent on the discretized fields of ϕ and U_i . The fields $\phi(x, y)$ and $U_i(x, y)$ are discretized using equations A.6 and A.7. The resultant discretized forms of the subscripted U and ϕ terms in equations A.12 and A.13 are defined to be:

$$\begin{aligned}
 \phi_x &= \phi_{i+1,j} - \phi_{i-1,j} \\
 \phi_y &= \phi_{i,j+1} - \phi_{i,j-1} \\
 Uy_y &= Uy_{i,j+1} - Uy_{i,j-1} \\
 Uy_x &= Uy_{i+1,j} - Uy_{i-1,j} \\
 Ux_x &= Ux_{i+1,j} - Ux_{i-1,j} \\
 Ux_y &= Ux_{i,j+1} - Ux_{i,j-1} \\
 Ux_{+y} &= Ux_{i,j+1} + Ux_{i,j-1} \\
 Ux_{+x} &= Ux_{i+1,j} + Ux_{i-1,j} \\
 Uy_{+y} &= Uy_{i,j+1} + Uy_{i,j-1} \\
 Uy_{+x} &= Uy_{i+1,j} + Uy_{i-1,j} \\
 Uxy_y &= Uy_{i+1,j+1} + Uy_{i-1,j-1} - Uy_{i-1,j+1} - Uy_{i+1,j-1} \\
 Uxy_x &= Ux_{i+1,j+1} + Ux_{i-1,j-1} - Ux_{i-1,j+1} - Ux_{i+1,j-1}
 \end{aligned}$$

A.3.3 Threshold in the Convergence of the Displacement Field

The Gauss-Seidel templates in equations A.12 and A.13 are iterated until a threshold criteria is reached. The threshold to the displacement field is defined by the threshold criteria,

$$e = |U_i^{j-1} - U_i^j| \quad (\text{A.14})$$

where j is the time iteration. The iteration over the entire field is repeated until $e < e'$ is satisfied everywhere, where e' is the threshold to which the displacement field is within a satisfied convergence.

To approximate the error in the displacement field for this threshold criteria, the radial displacement is considered for a circular inclusion. The total displacement inside a circular precipitate can be approximated as $\approx \frac{1}{2}\epsilon^*r$ and outside as $\approx \frac{1}{2}\frac{a^2}{r}\epsilon^*$ where a is the particle radius. The displacement change e is calculated everywhere in the domain and if it fails to meet the threshold *anywhere* then the entirety of the domain undergoes further convergence of the displacement field. If the displacement field is considered at the center of a circular precipitate and infinitely far away from the precipitate, assuming no translational displacement, the total displacement at these positions is zero. This results in no error in the solution at these positions. The position of greatest error is therefore surmised to be the position where the largest change in displacement occurs as the precipitate grows. This position corresponds to the precipitate interface. At the interface the displacement is $\approx \frac{1}{2}\epsilon^*a$ resulting in an error correction of $(\frac{e}{U_i})$ which is $\approx \frac{0.1}{a}\%$ and $\approx \frac{0.01}{a}\%$ for values of

$e' = 0.0001$ and 0.00001 and are considered to be worst case values for the error in the displacement field.

A.3.4 Displacement Field Dependency on the Interface Width W_o

An isotropic circular precipitate with a lattice eigenstrain of $\epsilon^* = 0.005$ is placed in a parent phase with identical elastic coefficients of $\bar{C}_{11} = 1011$ and $\bar{C}_{12} = 729$. The

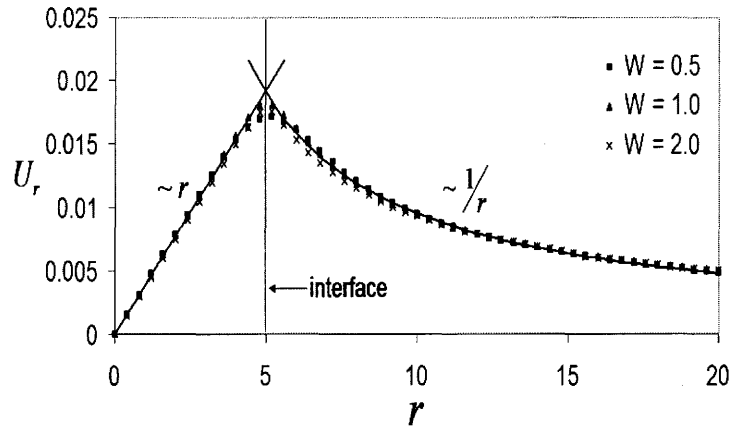


Figure A.2: Radial displacement field U_r for a precipitate with interface widths $W_o = 0.5, 1.0, 2.0$.

strain field is solved by Gauss-Seidel iteration with a threshold value of $e' = 0.0001$. Interface widths are chosen by setting $W_o = 0.5, 1.0, 2.0$ (in units of the capillary length) and the strain field is solved for each. Figure A.2 displays the resultant radial displacement field $U_r = \sqrt{U_x^2 + U_y^2}$ for these three interface widths. There are two points of note. Firstly, outside of the interface width each of the resultant displacement fields have excellent agreement. And secondly is the linear behaviour of the displacement field inside the precipitate and a $\frac{1}{r}$ behaviour outside of the precipitate, as expected.

Appendix B

Appendix - Phase Field Model Derivation with Elasticity

Derived here are the chemical and phase field mobility equations presented in chapter 4. These two equations are derived from the following free energy:

$$G(\nabla\phi, \phi, C, \epsilon_{ij}) = |W_o\nabla\phi|^2 + f(T) + H\left(\frac{\phi^2}{2} - \frac{\phi^4}{4}\right) - S(\phi)(T - T_m) + \frac{RT}{\nu}(C \ln C - C) + \epsilon(\phi)C + f_{el}(\phi) \quad (\text{B.1})$$

All of the terms in this equation are as defined previously in chapter 4 and H represents the nucleation barrier of the transformation. The phase dependent entropy is $S(\phi) = \frac{1}{2}(S_a + S_b - \frac{L}{T_m}g_2(\phi))$ and the phase dependent enthalpy of mixing is $\epsilon(\phi) = \frac{1}{2}(\epsilon_a + \epsilon_b + (\epsilon_a - \epsilon_b)g_1(\phi))$. g_1 and g_2 are interpolation functions through the diffuse interface with the limits of $g_i(\phi = \pm 1) = \pm 1$ and the derivative limit of $g_i(\phi = \pm 1) = 0$.

The standard dynamical form for the phase mobility equation is

$$\frac{1}{K_\phi} \frac{\partial\phi}{\partial t} = -\frac{\delta G(\nabla\phi, \phi, C, \epsilon_{ij})}{\delta\phi} \quad (\text{B.2})$$

where K_ϕ is related to the interface kinetics time. The chemical diffusion equation is given by

$$\frac{\partial C}{\partial t} = \vec{\nabla} \cdot \left(Dq(\phi)C\vec{\nabla} \frac{\delta G(\phi, C, \epsilon_{ij})}{\delta C} \right) \quad (\text{B.3})$$

To manipulate these equations to the forms presented in chapter 4 it is instructive to examine the equilibrium properties of G and develop a relationship for the chemical potential from this free energy. Namely,

$$\mu_{eq} = \frac{RT}{\nu} \ln(C_o) + \bar{\epsilon} + \frac{\Delta\epsilon}{2}g_1 \quad (\text{B.4})$$

This gives an equilibrium composition inside the interface as

$$C_o = e^{\left(\frac{\nu}{RT}(\mu_{eq} - \bar{\epsilon} - \frac{\Delta\epsilon}{2}g_1)\right)} \quad (\text{B.5})$$

Consider a static strain at some steady state, the composition at the interface is defined by the interfacial correction to the composition in equation 4.10 as

$$C_o(\infty) = C_b = e^{\left(\frac{\nu}{RT}(\mu_{eq} - \bar{\epsilon} - \frac{\Delta\epsilon}{2})\right)} \quad (\text{B.6})$$

Dividing these two relations gives a relationship between the sharp interface composition and the equilibrium composition in a diffuse interface as

$$\frac{C_o}{C_b} = e^{\left(\frac{\ln k}{2}(1+g_1)\right)} \quad (\text{B.7})$$

Under certain choices of the interpolation functions g_1 and g_2 , the phase field equation is in equilibrium and in 1-D the mobility equation collapses to

$$\frac{\partial\phi}{\partial t} = W_o^2 \frac{d^2\phi}{dx^2} - H(\phi^3 - \phi) = 0 \quad (\text{B.8})$$

The solution to this equation is a hyperbolic tangent of the form $-\tanh\left(\frac{x}{\sqrt{2W}}\right)$, where $W = \frac{W_o}{\sqrt{H}}$. The relationship between g_1 and g_2 is derived by substitution of the energy (Equation B.1) into the standard dynamical equation for the phase (Equation B.2). The double well ($H(\phi^3 - \phi)$) and the gradient energy ($W_o^2 \frac{d^2\phi}{dx^2}$) terms define the hyperbolic tangent form for the phase field. All other terms must exactly cancel to produce this steady state profile. These terms are set to zero and produce the following relationship of the two interpolation functions,

$$(1 - k)g_2' + \ln k \frac{C_o}{C_b} g_1' - \frac{\alpha Z_2}{C_b} g_2 g_2' = 0 \quad (\text{B.9})$$

By integrating the relationship in equation B.9 with respect to ϕ and using Equation B.7. A relationship between g_1 and g_2 can be derived to later eliminate g_1 in favour of g_2 . This relationship results in the equation

$$g_1 = \frac{2}{\ln(k)} \ln \left(\frac{1}{2}(k + 1 - (1 - k)g_2 - \frac{1}{2} \frac{\alpha Z_2}{C_b} (1 - g_2^2)) \right) - 1 \quad (\text{B.10})$$

The function Z_2 , which depends on the strain fields, is slowly varying across the interface and adjusts instantaneously compared to ϕ and the concentration. As such it can be treated as decoupled from the phase field and concentration field in the manipulations below. Of course, in the actual dynamics its form is adjusted instantaneously from the strain relation equations 4.13.

These relationships are now used to form the phase-field equations in Chapter

4.

B.1 Phase Field Equation

The phase field equation described in chapter 4 is derived by following precisely analogous techniques in the derivation of the phase field model in reference [8]. By substitution of the free energy in equation B.1, eliminating g_1 with equation B.10 and the use of equation B.7 the functional derivative of the free energy with respect to ϕ is rewritten as

$$\frac{\delta G}{\delta \phi} = -W_o^2 \nabla^2 \phi + H(\phi^3 - \phi) + 2Z_2 g_2 g_2' + \frac{C_b \Delta \epsilon (1-k)}{2 \ln(k) C_o} \left(\frac{\ln(k) \Delta T L e}{C_b (1-k) \Delta \epsilon T} C_o - C (1 - 2\beta_1 g_2) \right) g_2' \quad (\text{B.11})$$

where $Le = L + \frac{2T}{\Delta T} (Z_1 + Z_3 g_2^2)$ and $\beta_1 = \frac{\alpha Z_2}{2C_b(1-k)}$. The underlined portion of this equation is found to be $\frac{\ln(k) \Delta T L e}{C_b (1-k) \Delta \epsilon T} = 1$ by matching to the phase diagram and using the partition coefficient $k = \frac{C_s^{eq}}{C_l^{eq}} = \exp\left(-\frac{\Delta \epsilon \nu}{RT}\right)$. The functional derivative is rewritten as

$$\frac{\delta G}{\delta \phi} = -W_o^2 \nabla^2 \phi + H(\phi^3 - \phi) - \frac{1}{2} C_b (1-k) \frac{RT}{\nu} (1 - 2\beta_1 g_2) (1 - e^u) g_2' \quad (\text{B.12})$$

where $e^u = \frac{C}{C_o} = \frac{2C}{C_b} \left(k + 1 - (1-k)g_2 + \frac{\alpha Z_2}{2C_b} (1 - g_2^2) \right)^{-1}$. Substituting C_b from equation 4.10 and defining $\tilde{\lambda} = \frac{1}{2} \frac{RT(1-k)^2 C_b^{eq}}{\nu H}$, the functional derivative becomes

$$\frac{\delta G}{\delta \phi} = -W_o^2 \nabla^2 \phi + H(\phi^3 - \phi) - \left(\frac{H \tilde{\lambda}}{1-k} - Z_1 \right) (1 - 2\beta_1 g_2) (1 - e^U) g_2' \quad (\text{B.13})$$

Dividing this equation through by H and substituting into the standard dynamical form for the phase field equation (equation B.2) the phase field mobility equation becomes,

$$\tau \frac{\partial \phi}{\partial t} = W^2 \nabla^2 \phi - (\phi^3 - \phi) - \left(\frac{\lambda}{1-k} - \frac{15}{8} \frac{Z_1}{H} \right) (1 - 2\beta_1 g_2) (e^u - 1) (1 - \phi^2) \quad (\text{B.14})$$

where $\tau = \frac{1}{HK_\phi}$ is related to the kinetic attachment time, the interface width is $W = W_o / \sqrt{H}$, the constant $\lambda = \frac{15}{8} \tilde{\lambda}$, g_2 is the interpolation function and a convenient form is identical to the form in equation 1.18.

Defining a dimensionless undercooling as $U = \frac{e^u - 1}{1-k}$ and some rearrangement,

the phase field equation can be reformulated to a form similar to the pure model equation (Equation 1.9). This equation is

$$\tau \frac{\partial \phi}{\partial t} = W^2 \nabla^2 \phi - (\phi^3 - \phi) - \lambda U(1+B)(1-\phi^2)^2 \quad (\text{B.15})$$

where $B = \frac{1}{2(1-k)} \left(\left(\frac{\alpha Z_1}{(1-k)C_b^0} - 1 \right) \frac{\alpha Z_2}{C_b} g(\phi) - \frac{\alpha Z_1}{C_b^0} \right)$.

B.2 Chemical Diffusion

The chemical diffusion equation described in chapter 4 is derived by calculating the chemical potential with respect to the free energy in equation B.1. This equation is,

$$\frac{\partial C}{\partial t} = \vec{\nabla} \cdot (DqC\vec{\nabla}\mu) \quad (\text{B.16})$$

where D is the rate of diffusion in the parent phase and $q(\phi)$ is a function that interpolates the diffusion into the precipitate phase ($q(\phi) = 1$ for equal diffusion rates). The diffusion is reformulated into the dimensionless undercooling field $U = \frac{e^\mu - 1}{1-k}$. This is done by reformulating the composition field by the equation

$$C = \frac{A}{2} e^\mu = \frac{A}{2} \left[\frac{e^\mu - 1}{1-k} (1-k) + 1 \right] = [U(1-k) + 1] \frac{A}{2} \quad (\text{B.17})$$

where $A = C_b(k+1 - (1-k)g_2 - \frac{Z_2\alpha}{2C_b}(1-g_2^2))$. First the left hand side of equation B.16 is reformed in terms of U and then the right hand side will be reformed.

The left hand side of equation B.16 is modified by substituting equation B.17 and rearranging, this forms the left hand side into

$$\frac{\partial C}{\partial t} = \frac{1}{2} A(1-k) \frac{\partial U}{\partial t} + \frac{1}{2} [U(1-k) + 1] \cdot \left((k+1 - (1-k)g_2) \frac{\partial C_b}{\partial t} - C_b(1-k + \frac{\alpha Z_2}{C_b} g_2) \frac{\partial g_2}{\partial t} \right) \quad (\text{B.18})$$

The right hand side of equation B.16 is modified by substituting $\mu = \ln(U(1-k) + 1)$ and this results in the equation

$$\vec{\nabla} \cdot (Dq(\phi)C\vec{\nabla}\mu) = \vec{\nabla} \cdot (Dq(\phi) \frac{A}{2} (1-k) \vec{\nabla} U) \quad (\text{B.19})$$

By combining the left (Equation B.18) and right (Equation B.19), the chemical diffusion equation is reformulated in terms of the dimensionless undercooling U .

The equation is

$$\begin{aligned} \Psi \frac{\partial U}{\partial t} &= \vec{\nabla} \cdot (D\tilde{q}(\phi)C_b\vec{\nabla}U) \\ &+ (1 + (1 - k)U)C_b \left(1 + \frac{\alpha Z_2}{C_b(1 - k)} \right) \frac{\partial \phi}{\partial t} \\ &- (1 + (1 - k)U) \left(\frac{k + 1}{1 - k} - \phi \right) \frac{\partial C_b}{\partial t} \end{aligned} \quad (\text{B.20})$$

where $\Psi = C_b(k + 1 - (1 - k)\phi - \frac{Z_2\alpha}{2C_b}(1 - \phi^2))$.

Terminology

<i>Array</i>	A computer data structure in which information is stored in line in a contiguous block of computer memory.	26
<i>Element, Child</i>	An element that is a subdomain of another element.	28
<i>Element, Parent</i>	An element that has split to form 4 children.	28
<i>Element</i>	A branching point in a tree structure with references to the assigned nodes.	28
<i>Mode</i>	A mode is an integer that sets the frequency, with higher modes representing larger frequencies.	11
<i>Neighbour</i>	A structure of the same refinement level that shares a second common data structure, such as an element sharing a node.	28
<i>Nodal Count</i>	Total number of grid nodes used to describe a domain.	26
<i>Node, Boundary</i>	A grid node which lies on a user defined boundary.	30
<i>Node, Field</i>	A grid node existing in the bulk of the domain on which the model equations are applied.	30
<i>Node, Ghost</i>	A grid node that is required to provide a uniform mini-mesh for a field node, the field values at these nodes are interpolated from nearby field nodes.	30
<i>Pointer</i>	A structure containing a computer memory address.	26
<i>Pop</i>	The act of removing an object from a data structure, such as a stack.	33
<i>Push</i>	The act of placing an object into a data structure.	33
<i>Root</i>	The highest level of refinement in a tree, or an element representing the entire domain area that a tree structure describes.	31

<i>Stack</i>	A data structure that has a first in last out organization.	33
<i>Tree Data Structure</i>	A tree structure is a way of representing a hierarchical breakdown of a domain. A tree is composed of a root domain and from the root the domain is broken into sub domains, each of which can be viewed as a sub tree.	26

Bibliography

- [1] *New England Meteoritical Services*, 2003.
- [2] Karma A, Kessler D, and Levine H. *Phys Rev Lett*, **87**:045501, 2001.
- [3] A.B.Kuper, D.Lazarus, J.R.Manning, and C.T.Tomizuka. *Phys Rev*, **104**:1536, 1956.
- [4] Smigelskas A.D. and Kirkendall E.O. *Trans. AIME*, **171**:130, 1947.
- [5] Asaro R and Tiller W. *Metall Trans*, **3**:1789, 1972.
- [6] R. Almgren. *SIAM J. Appl. Math.*, 59:2086, 1999.
- [7] Athreya B, Goldenfeld N, Dantzig J, Greenwood M, and Provatas N. *Physical Review E*, **76**:056706, 2007.
- [8] Echebarria B, Folch R, Karma A, and Plapp M. *Physical Review E*, **70**:061604, 2004.
- [9] Morin B, Elder K R, Sutton M, and Grant M. *Phys Rev Lett*, **75**:2156, 1995.
- [10] W.J. Boettinger, J.A. Warren, C. Beckermann, and A. Karma. *Annu Rev. Mater. Res.*, **32**:163, 2002.
- [11] W.P Bosze and R.Trivedi. *Acta Met*, **23**:713, 1975.
- [12] Lund A C and Voorhees P W. *Acta Mater*, **50**:2585, 2002.
- [13] Tong C, Greenwood M, and Provatas N. *Physical Review B*, **77**:064112, 2008.
- [14] G. Caginalp. *Arch. Rat. Mech. Anal.*, 92:205, 1986.
- [15] G. Caginalp and W. Xie. *Phys. Rev. E*, 48:1897, 1993.
- [16] J. B. Collins and H. Levine. *Phys. Rev. B*, 31:6119, 1985.
- [17] Eshelby J D. *Proc Roy Soc London A*, **241**:376, 1957.

- [18] Rodney D, Bouar Y. Le, and Final A. *Acta Mater*, **51**:17, 2003.
- [19] Yeon D, Cha P, Kim J, Grant M, and Yoon J. *Modelling Simul. Mater. Sci. Eng.*, **13**:031609, 2005.
- [20] Kessler DA and Levine H. *Phys Rev E*, **61**:2348, 1999.
- [21] Kirkendall E, Thomassen L, and Upthegrove C. *Trans. AIME*, **133**:186, 1939.
- [22] K. R. Elder, Martin Grant, Nikolas Provatas, and Mike Kosterlitz. *Phys. Rev. E*, **64**:1604, 2001.
- [23] Lifshitz E.M. and Landau L.D. *Theory of Elasticity*, 1959.
- [24] Mecozzi M G, Sietsma J, Vand Der Zwagg S, Apel M, Schaffnit P, and Steinbach I. *Metall. Mater. Trans. A*, **36A**:2327, 2005.
- [25] G.Horvay and J.W.Cahn. *Acta Met.*, **9**:695, 1961.
- [26] Garcke H, Nestler B, and Stoth B. *SIAM J. Appl. Math*, **60**:295, 1999.
- [27] Henry H and Levine H. *Phys Rev Lett*, **93**:105504, 2004.
- [28] Jeffreys H and Jeffreys B S. *Methods of Mathematical Physics, 3rd ed.* Cambridge University Press, 1988.
- [29] Reiss H. *Methods of Thermodynamics*, 1996.
- [30] Tomita H. *Prog Theor Phys*, **85**:47, 1991.
- [31] M. Hillert. *Jernkontorets Ann*, **141**:757, 1957.
- [32] P. C. Hohenberg and B. I. Halperin. *Rev. Mod. Phys.*, **49**:435, 1977.
- [33] Steinbach I and Pezzolla F. *Physica D*, **134**:385, 1999.
- [34] Steinbach I and Apel M. *Physica D - Nonlinear Phenomena*, **217**:153, 2006.
- [35] G.P. Ivanstov. *Growth Crystals*, **3**:53, 1961.
- [36] Fan J, Greenwood M, Haataja M, and Provatas N. *Physical Review B*, **74**:031602, 2006.
- [37] Jou H J, Leo P H, and Lowengrub J S. *J Comp Phys*, **131**:109, 1997.
- [38] Laraia V J, Johnson W C, and Voorhees P W. *J Mater Res*, **3**:257, 1988.
- [39] Slutsker J, Thornton K, Roytburd A.L., Warren J.A., and McFadden G.B. *Phys Rev B*, **74**:014103, 2006.

- [40] Srolovitz D J. *Acta Metall*, **37**:621, 1989.
- [41] Malcolm JA and Purdy GR. *Trans Metall Soc AIME*, **239**:1391, 1967.
- [42] Ramirez J.C., Beckermann C, Karma A, and Diepers H.J. *Phys. Rev. E*, **69**:051607, 2004.
- [43] J.Jeong, N.Goldenfeld, and J.A.Dantzig. *Phys Rev E*, **64**:1063, 2001.
- [44] Zhu J.Z., Wang T, Ardell AJ, Zhou SH, Liu ZK, and Chen LQ. *Acta Mater*, **52**:2837, 2004.
- [45] Aguenau K, Muller J, and Grant M. *Philos Mag B*, **78**:103, 1998.
- [46] Kassner K, Misbah C, Muller J, Kappey J, and Kohlert P. *Phys Rev E*, **63**:036117, 2001.
- [47] Kassner K, Misbah C, Muller J, Kappey J, and Kohlert P. *J. Cryst. Growth*, **225**:289, 2001.
- [48] A. Karma. *Phys. Rev. Lett*, **87**:115701, 2001.
- [49] A. Karma and W.-J. Rappel. *Phys. Rev. E*, **53**:3017, 1996.
- [50] Elder KR and Grand M. *Phys Rev E*, **70**:051605, 2004.
- [51] Elder KR, Katakowski M, Haataja M, and Gran M. *Phys Rev Lett*, **88**:245701, 2002.
- [52] Zhang L, Chen L.Q., and Du Q. *Physical Review Letters*, **98**:265703, 2007.
- [53] J.S. Langer. *Rev. Mod. Phys.*, **52**:1, 1980.
- [54] Bletry M and Purdy G. *In house experiments at McMaster University*, 2006.
- [55] Grinfeld M. *Sov. Phys. Dokl*, **31**:831, 1986.
- [56] Haataja M and Leonard F. *Phys Rev B*, **69**:081201, 2004.
- [57] Koslowski M, Cuitino A.M., and Ortiz M. *J. Mech. Phys. Solids*, **50**:2597, 2002.
- [58] R.F. Mehl and C.S. Barrett. *Trans AIME*, **93**:78.
- [59] M.Hillert. *Met Trans A*, **6A**:5, 1975.
- [60] W. W. Mullins and R. F. Sekerka. *J. Appl. Phys.*, **34**:323, 1963.

- [61] Provatas N and Dantzig J. *The Encyclopedia of Materials Science and Technology*, 2001.
- [62] Provatas N, Greenwood M, Athreya B, Goldenfeld N, and Dantzig J. *International Journal of Modern Physics*, **19**:4525, 2005.
- [63] Provatas N, Wang Q, Haataja, and Grant M. *Physical Review Letters*, **91**:155502, 2003.
- [64] Ahmad NA, Wheeler AA, Boettinger WJ, and McFadden GB. *Phys Rev E*, **58**:3436, 1998.
- [65] Ahmad N.A., Wheeler A.A., Boettinger W.J., and McFadden G.B. *Physical Review E*, **58**:3436, 1998.
- [66] Stefanovic P, Haataja M, and Provatas N. *Phys Rev Lett*, **96**:225504, 2006.
- [67] P.Kopczynski, W.Rappel, and A.Karma. *Phys Rev E*, **55**:1282, 1997.
- [68] N. Provatas, J. Dantzig, and N. Goldenfeld. *J. Comp. Phys.*, 148:265, 1999.
- [69] Voorhees P.W. and Johnson W.C. *J.Chem.Phys*, **84**:5106, 1986.
- [70] Ru C Q. *Acta Mechanica*, **160**:219, 2003.
- [71] Folch R and Plapp M. *Phys. Rev. E*, **72**:011602, 2005.
- [72] Phillips R. *Crystals, Defects and Microstructures*. Cambridge University Press, 2001.
- [73] R.D.Townsend and J.S.Kirkaldy. *Trans ASM*, **61**:605, 1968.
- [74] Sekerka RF. *J Crystal Growth*, **264**:530, 2004.
- [75] R.F.Mehl, C.S.Barrett, and D.W.Smith. *Trans AIME*, **94**:215, 1933.
- [76] R.F.Mehl and O.T.Marzke. *Trans AIME*, **93**:123, 1931.
- [77] R.Trivedi and G.M.Pound. *J.App.Phys*, **40**:4293, 1969.
- [78] Majaniemi S and Provatas N. *In Review at Phys Rev E*, 2008.
- [79] Kim S.G., Suzuki T, and Ode M. *J. Cryst. Growth*, **261**:135, 2004.
- [80] P.H. Shipway and H.K.D.H. Bhadeshia. *Mat Sci and Eng*, **A223**:179, 1997.
- [81] Wang SL, Sekerka RF, Wheeler AA, Murray BT, Coriel SR, Braun RJ, and McFadden GB. *Physica D*, **69**:189, 1993.

- [82] Hu S.Y. and Chen L.Q. *Acta Mat*, **49**:463, 2001.
- [83] Hu S.Y. and Chen L.Q. *Comp Mat Sci*, **23**:270, 2002.
- [84] Hu S.Y. and Chen L.Q. *Acta Mat*, **52**:3069, 2004.
- [85] Hazhimali T, Karma A Gonzales F, and Rappaz M. *Nature Materials*, **5**:660, 2006.
- [86] R. Trivedi, Shan Liu, B. Echebarria, and A. Karma. *TMS*, 2004.
- [87] Wang Y. U., Jin Y. M., and Khachaturyan A. G. *J Appl Phys*, **91**:6435, 2002.
- [88] Wang Y U, Jin Y M, and Khachaturyan A G. *Appl Phys Lett*, **80**:4513, 2002.
- [89] Wang Y U, Jin Y M, and Khachaturyan A G. *J Appl Phys*, **92**:1351, 2002.
- [90] Wang Y U, Jin Y M, and Khachaturyan A G. *Acta Mater*, **52**:1039, 2004.
- [91] Vaithyanathan V, Wolverton C, and Chen L.Q. *Acta Mat*, **52**:2973, 2004.
- [92] Husain S W, Ahmed M S, and Qamar I. *Metall. Mater. Trans. A*, **30A**:1529, 1999.
- [93] Voorhees P W, McFadden G B, and Johnson W C. *Acta Metall Mater*, **40**:1979, 1992.
- [94] J. A. Warren and W. J. Boettinger. *Acta Metall. Mater. A*, 43:689, 1995.
- [95] W.D.Calister. Materials science and engineering an introduction. *John Wiley and Sons inc*, 2003.
- [96] W.P.Bosze and T.Trivedi. *Acta Met*, **23**:713, 1975.
- [97] Bouar Y, Loiseau, and Khachaturyan A G. *Acta Mater*, **46**:2777, 1998.
- [98] Lu Y, Chen Z, Li Y, Wang Y, and Chu Z. *Prog Nat Sci*, **15**:1104, 2005.
- [99] Ni Y and He L.H. *Acta Mater*, **51**:4161, 2003.
- [100] Ni Y, He L.H., and Song J. *Surf Sci*, **553**:189, 2004.
- [101] Dong-Hee Yeon, Pil-Ryung Cha, Ji-Hee Kim, Martin Grant, and Jong-Kyu Yoon. *Model and Simul in Mat Sci and Eng*, **13**:299, 2005.
- [102] Y.Kim, N.Provatas, N.Goldenfeld, and J.Dantzig. *Phys Rev E*, **59**:2546, 1999.
- [103] Yoo Y.S. *Scr Mater*, **53**:81, 2005.
- [104] C. Zener. *Met Soc AIME*, **167**:550, 1946.